TECHNISCHE UNIVERSITÄT MÜNCHEN

Max-Planck-Institut für Physik
(Werner-Heisenberg-Institut)

Muon Colliders, Frictional Cooling and Universal Extra Dimensions

Daniel E. Greenwald

Abstract

A muon collider combines the advantages of pp and e^+e^- colliders, sidestepping many of their disadvantages, and has the potential to make discoveries and precision measurements at high energies. However, muons bring their own technical challenges, largely relating to their instability. We present a summary of the motivations and research and development efforts for a muon collider.

We detail a frictional cooling scheme for preparing high-luminosity muon beams on timescales shorter than the muon lifetime. This involves bringing a hot beam of muons to an equilibrium energy by balancing energy losses to a retarding medium and energy gains from an electric field. We investigate the impact of low-energy charge exchange processes on the cooling of positively charged particles, and find that they necessitate significant changes to schemes previously developed for negatively charged particles: the cooling medium is limited to helium gas; the maximum equilibrium energy is limited to approximately 4 keV for μ^+; and the electric field strengths needed to bring particles to an equilibrium energy are up to several times larger than those needed to bring negatively charged ones to the same energy.

We present the commissioning of the Frictional Cooling Demonstration experiment at the Max Planck Institute for Physics, which will verify the simulation of the physics processes involved in frictional cooling. In the experiment, protons will be accelerated from rest to keV energies over several centimeters and the dependence of their energies on the strength of the accelerating electric field and density of the retarding helium gas will be determined. The current status and the future of the experiment are discussed.

Finally, we present the universal extra dimensions model, which posits the existence of compact spatial dimensions beyond the three of the standard model, resulting in towers of heavy copies of the standard model at regular mass intervals. We show that a characteristic signal at a muon collider of one extra dimension is the increase of the production of soft muon pairs accompanied by large missing energies. Using this signal, we show that percent-level-or-better uncertainty on the measurement of the size of the extra dimension is possible, and that the uncertainty increases with a decrease of the angular acceptance of the collider detector. This motivates our discussion of frictional cooling for a muon collider, since it can potentially reduce background radiation in the detector, allowing for smaller radiation shielding and a larger angular acceptance.

Zusammenfassung

Ein Myon-Collider vereint die Vorteile eines Proton-Proton- und Elektron-Positron-Colliders und umgeht deren wesentliche Nachteile. Er hat das Potenzial, neue Erkenntnisse auf dem Gebiet der Teilchenphysik zu ermöglichen und erlaubt Präzisionsmessungen bei hohen Energien. Allerdings birgt die Arbeit mit Myonen ihre eigenen technischen Herausforderungen, vor allem aufgrund der Instabilität der Myonen. Im Folgenden werden die Konzepte eines Myon-Colliders sowie die dafür notwendige Forschungs- und Entwicklungsarbeit zusammengefasst.

Wir beschreiben detailliert das Frictional Cooling, das auf kleineren Zeitskalen als der Myonlebensdauer zur Gewinnung von Myonenstrahlen mit hoher Luminosität verwendet wird. Zu diesem Zweck wird ein heißer Myonenstrahl auf eine Gleichgewichtsenergie gebracht, indem man den Energieverlust an das umgebende Medium mit Energiegewinn von einem elektrischen Feld ausgleicht. Wir untersuchen den Einfluss von niederenergetischen Ladungsaustauschprozessen auf die Kuehlung von positiv geladenen Teilchen und stellen fest, dass sie beträchtliche Änderungen an den Systemen, die für negativ geladene Teilchen entwickelt wurden, nötig machen: Das Kühlmedium ist auf gasförmiges Helium beschränkt. Die maximale Gleichgewichtsenergie ist auf ungefähr 4 keV für μ^+ beschränkt. Außerdem müssen die elektrischen Felder, die nötig sind, um die Teilchen auf eine Gleichgewichtsenergie zu bringen, teilweise um ein Vielfaches stärker sein als die Felder, die nötig sind, um negativ geladene Teilchen auf dieselbe Energie zu bringen.

Wir präsentieren die Inbetriebnahme eines Frictional-Cooling-Demonstrationsexperiments am Max-Planck-Institut für Physik, das die Simulation der physikalischen Prozesse, die beim Frictional Cooling auftreten, bestätigen wird. Zu diesem Zweck werden Protonen über mehrere Zentimeter hinweg aus der Ruhe auf Energien von einigen keV beschleunigt und die Abhängigkeit ihrer Energien von der Stärke des beschleunigenden elektrischen Feldes und der Dichte des abbremsenden Heliumgases wird bestimmt. Der gegenwärtige Status und die Zukunft des Experiments werden diskutiert.

Schließlich stellen wir das Universal-Extra-Dimensions-Modell vor, das die Existenz von kompakten Raumdimensionen zusätzlich zu den drei Raumdimensionen des Standardmodells voraussetzt, was zu Türmen von schweren Kopien des Standardmodells in regelmäßigen Massenabständen führt. Wir zeigen, dass ein charakteristisches Signal einer zusätzlichen Dimension an einem Myon-Collider der Anstieg der Produktion von weichen Myonenpaaren mit großen fehlenden Energien ist. Wir zeigen, dass mit diesem Signal eine Messung der Groeße der zusätzlichen Dimension mit einer Unsicherheit von höchstens Prozentniveau

möglich ist und dass die Unsicherheit mit der Abnahme der Winkelakzeptanz des Collider-Detektors zunimmt. Diese Erkenntnis motiviert unsere Diskussion des Frictional Coolings für einen Myon-Collider, da diese Technik möglicherweise die Untergrundstrahlung im Detektor reduzieren kann, was eine schwächere Strahlungsabschirmung und eine größere Winkelakzeptanz ermöglicht.

In conclusion, we have investigated the possibility of the use of colliding muon beams ..., and have found it to be difficult but perhaps not impossible.

David Neuffer, 1979

Contents

CHAPTER 1

Introduction

The greatest tool available to particle physicists in the last half century has been the collider. By accelerating particles to higher and higher energies, we have probed ever deeper inside composite particles to discover their constituents. Exploiting Einstein's energy–mass equivalence, we have also created heavier and heavier particles by converting the kinetic energy of accelerated particles into the masses of new particles.

In the first half of the last century, cosmic rays and radioactive sources outpaced the first accelerators in terms of aiding in the discovery of particles; they brought us the proton, the positron, the muon, and light mesons and baryons. But by the late 1940s, most of the particles light enough to be discovered through these means had been seen. It was then that accelerators facilitated the discovery of the neutral pion, the antiproton, the antineutron, and heavier mesons and hadrons. When the earliest colliders exhausted the discovery of the zoo of GeV/c^2 mesons and hadrons, physicists developed ways to increase the collider energies to probe higher mass ranges. Figure 1.1 shows a so-called Livingston plot of the center-of-mass energies ($\sqrt{s}$) of some representative particle colliders and their first years of operation.* It is interesting to view this plot alongside that of figure 1.2, which shows the masses of several high-mass particles and their years of discovery. All the particles in the figure were discovered at particle accelerators.

The multitude of particles discovered in the middle of the last century gave theorists much to think about. For a time, experimental findings were largely ahead of theoretical explanations. When these explanations came, they predicted new particles, such as the heavy weak gauge bosons $W^{\pm}$ and Z^0 [1–3], which were subsequently discovered in the early 1980s at CERN's Super Proton Synchrotron (SppS in figure 1.1). Ten years later, the heaviest standard-model (SM) particle, the top quark t was discovered at Fermilab's Tevatron.

There is only one yet-undiscovered fundamental particle in the standard model of particles and interactions, the Higgs boson. But physicists have posited new theories beyond the standard model (BSM) that predict even heavier particles. To discover these particles, colliders have been designed to reach to center-of-mass energies well above the masses of the weak bosons. The Large Hadron Collider at CERN (LHC in figure 1.1) has recently started operation and

---

*Named after M. Stanley Livingston who prophesied the continuous increase of collider energies.

looks for the Higgs boson and the heavy particles of various new theories. As well, a large research and development effort has been focused on increasing the center-of-mass energy of a lepton collider. Figure 1.1 shows the proposed energies of three such colliders: two electron-positron colliders—the International Linear Collider (ILC) at 500 GeV, and the Compact Linear Collider (CLIC) at several TeV; and a muon collider (μC) at 100s of GeV to several TeV.

This thesis is concerned with three topics related to muon colliders. **Chapter two** presents the physics motivation for building a muon collider, the general design of one, and the past and current research and development efforts towards building one. **Chapter three** tackles the first topic, frictional cooling— a method of beam preparation for a muon collider—and updates certain findings by including the effects of charge exchange processes in the stopping of positively charged particles in matter. **Chapter four** details software we developed for the simulation of frictional cooling and charge exchange.

Chapters five, six, and seven are concerned with the second topic: the Frictional Cooling Demonstration experiment. They present the construction of the experiment at the Max Planck Institute for Physics, the simulation of the experiment, and our first measurements.

Finally, **chapter eight** presents a model of physics beyond the standard model called universal extra dimensions, which predicts towers of heavier and heavier versions of the standard-model particles existing as the 4D phenomenology of excitations in an extra spatial dimension. And **chapter nine** discusses the search for such physics at a 3-TeV muon collider, and how frictional cooling may be utilized to create optimal conditions for the precise measurement of the size of an extra dimension.

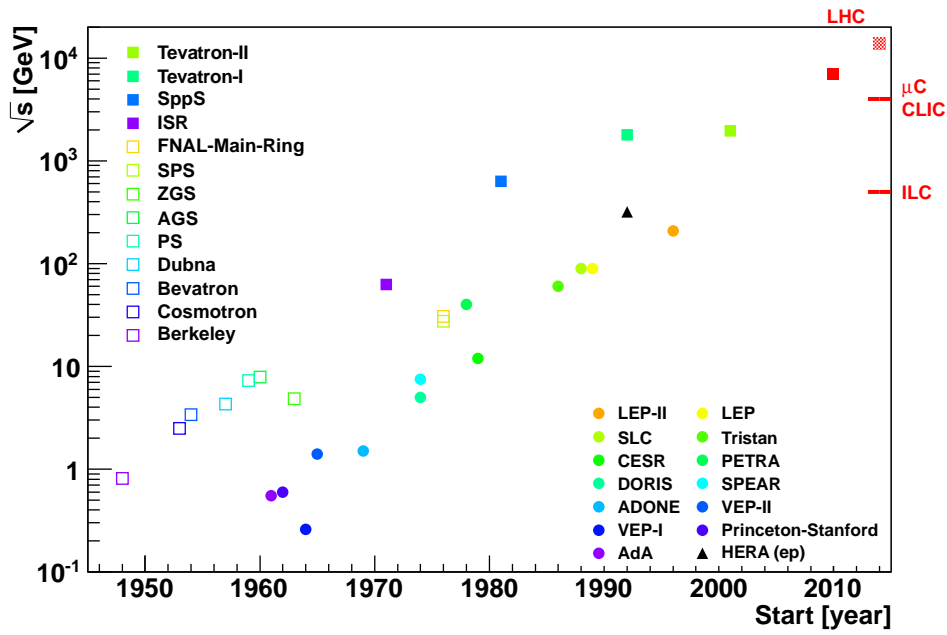Figure 1.1: Center-of-mass energies of several high-energy colliders versus the starting years of their operation. Hadron colliders are represented by ■ (□ for fixed-target experiments), lepton colliders by •, and lepton-hadron colliders by ▲. The current LHC energy and proposed ILC, CLIC, and muon collider energies are shown.
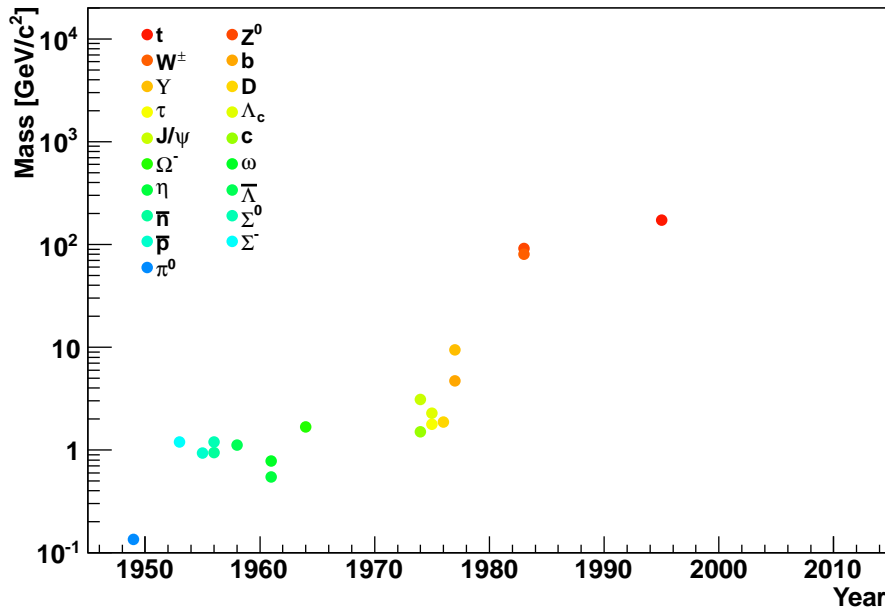
Figure 1.2: Masses of several high-mass particles versus the years of their discovery.

3

Muon Collider

The concept of a muon collider dates back at the latest to 1979, when Neuffer [4] proposed colliding muons at center-of-mass energy $\sqrt{s} = 90$ GeV. In his scheme (figure 2.1), a 400-kW beam of 300-GeV protons interacts with a solid target to produce pions; the momentum acceptance of the collider ring is tuned to select 45-GeV muons from the decay products of the pions. Neuffer estimated a possible beam luminosity of only 10^{24} cm$^{-2} \cdot$s^{-1}. He also estimated the cross section for $\mu^+ + \mu^- \to Z$ to be 10^{-31} cm^2, allowing for only $\mathcal{O}(10)$ events to be measured per year.

In the last thirty years a large research and development effort has been devoted to raising this luminosity by ten orders of magnitude and making a muon collider a viable and interesting experiment. In this chapter, we describe this effort and the changes it has affected in the muon collider scheme, particularly with respect to pion production and muon-beam preparation.

2.1 MOTIVATION

Traditionally, high-energy colliders have been built to accelerate electrons and protons. Both projectile particles offer advantages and disadvantages: The proton is heavy, but composite. The electron is elementary, but light.

The disadvantage of circularly accelerating light particles manifests itself through synchrotron radiation, which causes an accelerated particle to lose energy according to

$$\Delta E = \frac{4\pi\alpha\hbar c}{3R} \left(\frac{E}{mc^2} \right)^4,$$
(2.1)

where ΔE is the energy lost per turn around the collider ring, R is the bending radius of the ring, and E and m are the energy and mass of the particle [5]. This places a practical limit on the energy reach of an accelerator. For example, a 250 GeV electron would lose 33% of its energy each turn around the Large Electron-Positron (LEP) collider ($R = 4.2$ km).

There are two ways to overcome this limit: increase R or increase m. Increasing R has its own practical limits. For example, to bring the energy losses of a TeV-center-of-mass e$^+$e$^-$ collider down to the percent levels of LEP (90 GeV center-of-mass energy), one would need to build it along the earth's equatorial circumference. One can increase R to infinity, decreasing the energy loss to zero, by building a linear collider, the length of which is then determined by the limits
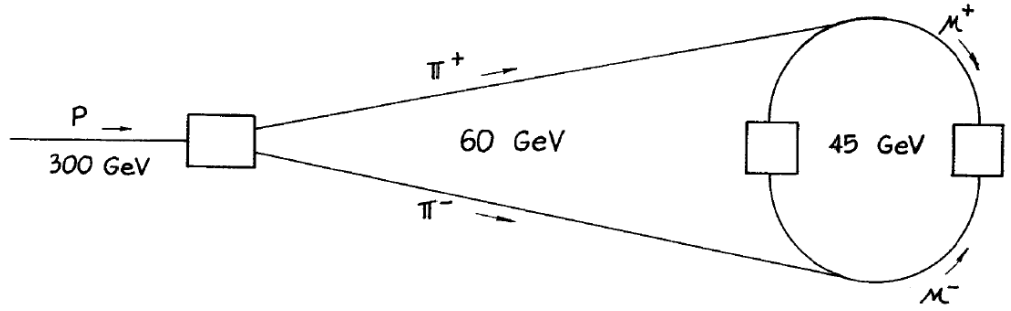
Figure 2.1: Schematic of a 90-GeV $\mu^+\mu^-$ collider from [4].

of acceleration techniques.[*] However, building a linear collider is not a simple solution [6, 7].

Increasing m is achieved by accelerating heavier particles. The energy loss at a proton collider is $(m_\mathrm{p}/m_\mathrm{e})^4 \approx 10^{13}$ times smaller than that of an identical electron collider. For comparison, protons at the 14-TeV Large Hadron Collider, which is in the same tunnel as LEP, will lose less than $10^{-7}\%$ of their energy each turn. However, protons are not elementary particles.

The disadvantages of colliding composite particles become apparent in the analysis of collisions. Since protons are not elementary, the collision of two 7-TeV beams does not result in a collision energy of 14 TeV, but instead an energy only a fraction of the total of the two beam energies. Furthermore, this fraction is not known precisely. Protons consist of partons (valence quarks, sea quarks, gluons, photons) that each carry a fraction x of the proton's total momentum P. The likelihoods $F(x)$ for the different types of partons to carry xP momentum are described by parton distribution functions (PDFs; figure 2.2). Since these functions must be folded into the calculation of the pp (or p$\bar{\text{p}}$) cross section for an interaction, uncertainties on the PDFs limit the precision to which cross sections can be measured.

A parton of one proton is orders-of-magnitude more likely to interact with a parton of another proton (or antiproton) at small x than at a large x. Therefore, most collisions happen at an energy much smaller than the combined beam energies. Not only is the likelihood small for the occurrence of high-energy ("hard") interactions in which new physics can be seen, but also many low-energy ("soft") interactions occur during each crossing of the beams. Figure 2.3 shows the total cross section at a hadron collider along with several cross sections of interesting processes hoped to be studied [9]; the irreducible QCD background cross sections are orders of magnitude larger than those for the new processes one hopes to investigate. The products of these soft interactions must be disentangled from the products of the hard interaction of interest to physicists, complicating event analysis.

---

[*]The length is also limited by what a PhD student prefers not to think about: money & politics. As the length increases, the costs grow higher, and finding somewhere to locate such a collider becomes more troublesome.

6
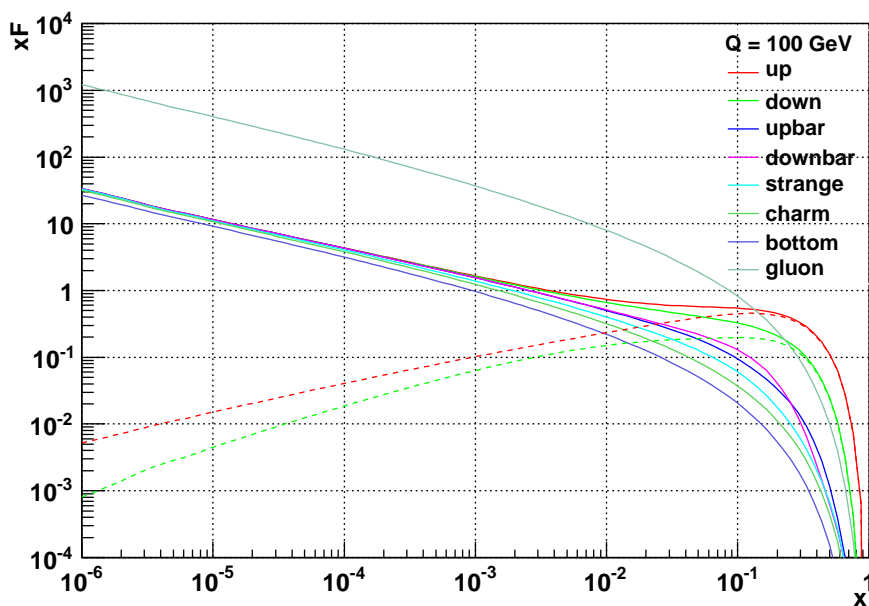
Figure 2.2: Parton distribution functions (F) multiplied by x for the proton at squared momentum transfer $Q^2 = (100 \text{ GeV})^2$ from the MSTW2008 leading order description [8]. The dashed lines show the valence quark components.

Since the interaction energy is unknown in an event, missing energy cannot be used as an indicator of new physics that contains a stable (or quasistable) particle carrying energy out of the experiment undetected. For an example of this, see section 9.1. Instead missing transverse energy must be used, placing limitations on an analysis.

Muons, like protons, are much heavier than electrons ($m_\mu \approx 207 m_e$), so the energy losses to synchrotron radiation for circularly accelerated muons are more than 10^9 times smaller than for electrons. Muons at a 3-TeV-center-of-mass collider 4 km in diameter would lose less than $2 \times 10^{-5}\%$ of their energy each turn. This is a negligible amount, allowing for muons to be circularly accelerated at colliders with small bending radii.

The synchrotron-radiation problem can be avoided for electrons by using a linear collider scheme. But at the interaction point, beam–beam interactions cause a widening of the $\sqrt{s}$ spread, which like synchrotron radiation, has an m^{-4} proportionality. Figure 2.4 shows the distribution of beam luminosity as a function of $\sqrt{s}$ at a proposed muon collider and the proposed CLIC e^+e^- linear collider [10]. At the muon collider, the full luminosity is expected to be contained within a 0.1%-wide window around the central energy. At CLIC, only 35% of the luminosity is expected to be contained within a 1%-wide window around the central energy.

Muons, like electrons, are elementary particles. A 1-TeV muon is a 1-TeV muon and nothing else; no PDFs must be folded into an analysis. Likewise, col-
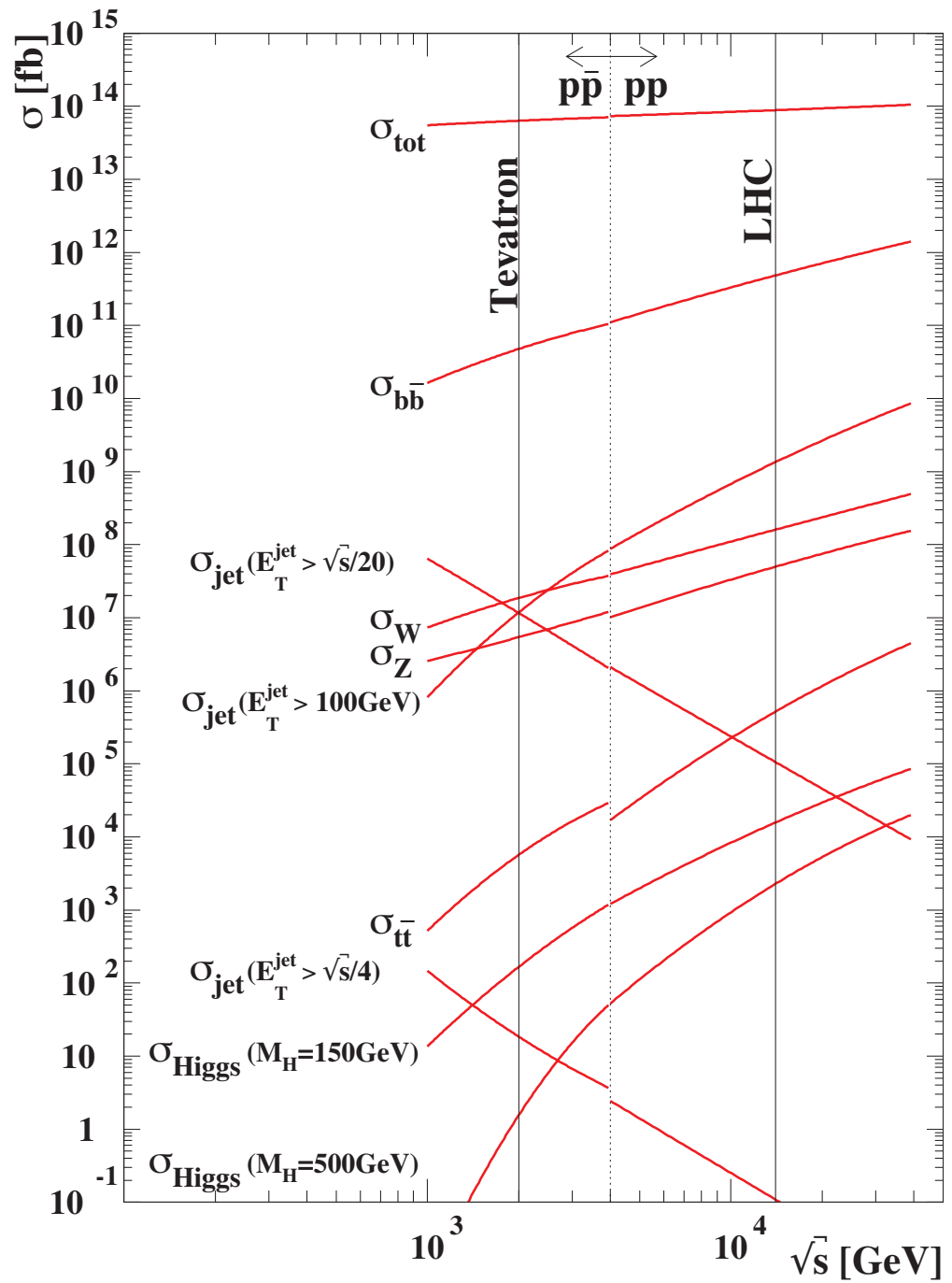
Figure 2.3: Total cross section as well as cross sections for several representative processes as a function of center-of-mass energy at a $p\bar{p}$ collider ($\sqrt{s} < 2$ TeV) and a pp collider ($\sqrt{s} > 2$ TeV), from [9]. The Tevatron and 14-TeV LHC are highlighted by the vertical lines.
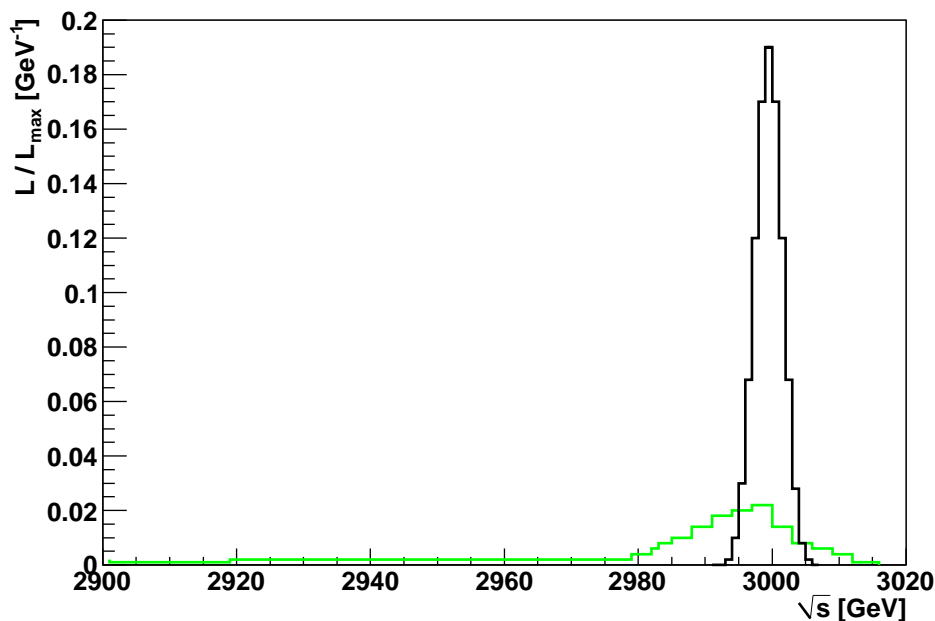
Figure 2.4: Luminosity density ($L/L_{\max}$) as a function of center-of-mass energy at a muon collider (black) and CLIC (green), from [10].

lision events are comparatively clean, lacking the tens of underlying soft events that contaminate the collision environments at pp and p$\bar{\text{p}}$ colliders.

Of course, the muon is an unstable particle. Its decay presents serious challenges to the production and collision of beams. These issues are addressed in sections 2.3 and 2.4.

2.2 PHYSICS AT A MUON COLLIDER FACILITY

The physics program at a muon collider has been much discussed ([11–15] offer some general overviews). A muon collider facility would allow for more than just collider experiments: The intense muon source at the front end of the collider could be used for physics studies on its own. The neutrino beam resulting from decay of the initial pions and muons (before acceleration) could be used for neutrino experiments. As well, the neutrino beams arising from decay of the accelerated muon beams along straight sections of the collider ring would be unique in intensity and energy definition and could be used for high-flux neutrino experiments.

With a muon collider, one would have the potential to detect the signals of physics beyond the standard model at the high-energy frontier and at the same time precisely measure the parameters of such new physics. One could also increase the precision on remaining standard-modelparameters that the LHC expects to measure.

2.2.1 Sub-TeV Collider

A sub-TeV muon collider can be a so-called Higgs factory, focusing on the $\sqrt{s}$ region around where the Higgs boson may be discovered at the LHC. The Higgs boson couplings to particles are proportional to their masses, so the coupling to the the muon is much stronger than to the electron, increasing the cross section for Higgs events. Also, the energy spread of the beams at a muon collider is expected to be much narrower than that of the beams at an electron collider, allowing for a more precise measurement of the Higgs mass. By searching for the threshold for s-channel Higgs-boson production with a muon collider, one could potentially measure the Higgs mass to a precision of $\Delta m_{\rm h}/m_{\rm h} = \mathcal{O}\!\left(10^{-6}\right)$ [11,16]. This is orders of magnitude better than the precisions expected at the LHC, $\mathcal{O}\!\left(10^{-3}\right)$, and a linear e^+e^- collider, $\mathcal{O}\!\left(10^{-4}\right)$ [17]. A high-precision measurement of the Higgs mass and decay width would allow for constraint of BSM parameters. For example, in the minimal supersymetric standard model (MSSM) one could constrain the masses of the heavy neutral-Higgs doublets and $\tan\beta$ (the ratio of the vacuum expectation values of the two Higgs doublets) through measurement of the Higgs boson branching ratios [14].

Since a muon collider would have a narrow center-of-mass energy spread and a high Higgs production rate, the CP-nature of the light Higgs and CP violation in a nearly mass-degenerate heavy neutral Higgs pair (as can exist in the MSSM [18]) could also be probed, if polarization of the muon beams is possible, by looking at Higgs production asymmetries involving the polarization directions of the beam [16, 19, 20].

The threshold for pair production of the new particles of a supersymmetry (SUSY) theory may be measured if the new particles are sufficiently light enough [21–23]. The masses of the W boson and the top quark could also be measured to higher precision through threshold cross section measurements. The mass of the W could be measured to within 6 MeV; the mass of the top quark to within 70 MeV [24]. The current precisions on these masses are 23 MeV and approximately 1 GeV [25].

2.2.2 Multi-TeV Collider

A multi-TeV muon collider offers myriad options of physics to study. Certainly, and unfortunately, theorists outpace accelerator physicists, and before a muon collider will be built, new theories yet-formulated will arise. The following is a list of just a few of the main areas of BSM physics that can be studied at a muon collider. The physics program at a muon collider would be nearly the same as that of an electron collider of comparable energy; and many of the studies of the potentials of a muon collider adapt calculations made for an e^+e^- collider.

SUPERSYMMETRY

A natural scale for SUSY models is the TeV scale, resulting in new heavy particles at this scale. Another feature of many SUSY models is the conservation of so-called R parity, which mandates the production of supersymmetric particles in

pairs only. This means that these new heavy particles can only be produced at a multi-TeV collider. R parity conservation also requires that the decay chain of a supersymmetric particle end at a stable lightest supersymmetric particle (LSP). The undetectability of this particle will mean that missing energy is a key feature of the SUSY collider signal. The high energy reach, known collision energy, narrow beam-energy spread, and relatively clean collision environment of a muon collider makes it the ideal probe of SUSY [23, 26].

A muon collider also offers a good laboratory for testing the conservation of R parity or for measuring the size of R parity violation; and would be complementary to an e^+e^- collider in terms of the R-parity-violating channels each can study [27].

EXOTIC ELECTROWEAK SECTORS

The TeV scale may also be where the electroweak sector becomes strongly interacting. This can be studied at a high-energy collider through V–V scattering (V standing for a vector boson), by carefully measuring the angular distribution and invariant masses of the outgoing decay products of the scattered vector bosons [28]. This can best be achieved in the clean interactions of a $\mu^+\mu^-$ collider, and can be enhanced by the running of the machine as a $\mu^-\mu^-$ or $\mu^+\mu^+$ collider.

This energy scale may also be that of additional new weak bosons, such as the right-handed W_R or Z' [29]. Studies have been made of the discovery potentials for these theories at a multi-TeV muon collider [26, 30].

EXTRA DIMENSIONS

An interesting class of BSM theories posits the existence of spatial dimensions beyond the three of the standard model [31–33]. Such extra dimensions are generally required of string theories, are often necessary for SUSY-breaking mechanisms [34], and depending on the particular model, address the hierarchy problem inherent in the standard model. The number of extra dimensions and their shapes vary greatly amongst the models. But all models require the dimensions to be compact, which necessitates the existence of excited states of the standard-model particles, seen as towers of heavier-mass particles.

Like SUSY these theories often have heavy states that must be pair-produced, and a lightest stable particle. The requirements on a collider for discovery are similar. Therefore a muon collider is an ideal laboratory for the investigation of these theories. Studies have been made of the discovery potential of these theories as well as the ability to discern between them and supersymmetry for pp and e^+e^- colliders and comparisons have been made showing that a lepton collider provides better discovery potential (for example [35, 36]); but no studies exist for a $\mu^+\mu^-$ collider. The potential at a muon collider will be addressed in this thesis in chapter nine for a particular model of extra dimensions.

REALLY EXOTIC PHYSICS

The list of possible new physics is as endless as the imaginations of theorists, and includes for example 4th-generation fermions, quark singlets, leptoquarks,

Baseline	Flux	CC Rate
[km]	$[\mathrm{m}^{-2} \cdot \mathrm{year}^{-1}]$	$[\mathrm{kt}^{-1} \cdot \mathrm{year}^{-1}]$
10^4	$10^{10} - 10^{11}$	$10^2 - 10^3$
10^3	$10^{12} - 10^{13}$	$10^4 - 10^5$
1	10^{16}	10^6

Table 2.1: Neutrino fluxes and charged-current (CC) event rates for a νF beam from a 20-GeV to 50-GeV muon beam at a very-long-baseline, long-baseline, and near experiment.

and mirror fermions; all of which have been discussed in the overview literature cited above.

2.2.3 *Neutrino Factory*

While the instability of muons creates a challenge to producing a collideable beam, it brings with itself one great benefit: the decay of muons along a straight section of a storage ring would produce a high-intensity beam of neutrinos. This is referred to as a neutrino factory (νF). Since the front end for a neutrino factory would greatly resemble that of a muon collider, its construction is often seen as a first step towards one, which may also contain a storage ring for the production of a neutrino beam.

Neutrinos are emitted from muons isotropically in the muon rest frame with a continuum of energies. However, in the boosted frame of the accelerated muons, these neutrinos form a high-energy beam with a narrow divergence,

$$\theta_\nu \approx \tan \theta_\nu \approx \gamma_\mu^{-1}, \tag{2.2}$$

where γ_μ is the Lorentz factor of the muon beam.

Furthermore, unlike current neutrino beams and proposed superbeams [37–39], the contents of the beam would be well defined: 50% each of ν_μ and $\bar{\nu}_e$ from a μ^- beam—and the charge-conjugate beam from a μ^+ beam—with no contamination from other neutrino species. This would allow for "wrong sign" searches for neutrino oscillation: the production of μ^+ (μ^-) in a detector illuminated by a beam initially containing no $\bar{\nu}_\mu$ (ν_μ) is clearly recorded as an oscillation event. Another unique feature of a neutrino factory (in comparison to superbeams and beta beams [40]) is that the ν's have sufficiently high energies to produce τ's, allowing one to search for ν_τ appearance [41].

Studies for both a dedicated neutrino factory and a νF as part of a muon collider [40, 42] predict $\mathcal{O}(10^{20})$ ν and $\bar{\nu}$ per year. This translates to the fluxes and event rates for oscillation experiments listed in table 2.1 using neutrino beams from stored muon beams with energies between 20 GeV and 50 GeV.

Nuetrino beams from higher-energy muons (250 GeV or greater) can be used for deep-inelastic scattering off a target placed near (1 km or less) the storage or collider ring. Studies of the experimental potential of such a scheme predict event rates of 10^5 per year per kilogram of target [42–44].

2.2.4 *Muon–Proton Collider*

One can also collide a high-energy muon beam with a high-energy proton beam to study the proton structure functions with deep-inelastic scattering. Studies of this potential have projected a high-precision Q^2 reach of 10^5 GeV^2, with a luminosity two orders of magnitude higher than that of the HERA ep collider at the Deutsches Elektronen Synchrotron [11, 45, 46].

2.2.5 *Front End Physics*

The intense flux of muons at the front of a muon collider complex would allow for high-precision measurements of standard-model parameters. Deviations from SM predictions can indicate the presence of BSM physics.

MUON MAGNETIC MOMENT

Measurement of the muon's magnetic-moment anomaly, $a_\mu \equiv \frac{1}{2}(g_\mu - 2)$, where g_μ is its gyromagnetic ratio, can be greatly improved at a muon collider facility. The current world-average experimental values for $a_{\mu+}$ and a_{e+} are [25]

$$
\begin{aligned}
a_{\mu+} &= (11659209 \pm 6) \times 10^{-10}, \\
a_{e+} &= (115965218073 \pm 28) \times 10^{-14}.
\end{aligned}
\tag{2.3}
$$

Contributions to a from new physics are (for BSM theories in general) dependant on m_l $(l = e, \mu, \tau)$,

$$
a_l^{\text{BSM}} \propto \left(\frac{m_l}{\Lambda}\right)^2,
\tag{2.4}
$$

where Λ is the energy scale of the new theory [47]. Therefore, though the measurement of the anomaly is more precise for electrons than muons by three orders of magnitude, measuring a_μ is still a more-precise test of new physics than measuring a_e and allows for the setting of stricter limits on Λ. This can be seen even within the standard model: The electroweak contributions to a_l are [48]

$$
\begin{aligned}
a_\mu^{\text{EW}} &= 154 \times 10^{-11} &\approx 2.6\,\sigma_a^\mu, \\
a_e^{\text{EW}} &= 3 \times 10^{-14} &\approx 0.1\,\sigma_a^e,
\end{aligned}
\tag{2.5}
$$

where σ_a^l is the experimental uncertainty on a_l. Clearly, measuring a_μ tests the electroweak theory, whereas measuring a_e does not. Studies of the a_μ measurement potential at a muon collider or neutrino factory facility [49] have predicted an achievable precision of less than 0.1 ppm, an order of magnitude better than the current highest precision, 0.44 ppm, achieved at Brookhaven National Laboratory [50].

LEPTON FLAVOR VIOLATION

Lepton-flavor-violating (LFV) decays of muons,

$$
\mu^\pm \to e^\pm \gamma, \qquad \mu^\pm \to e^\pm\, e^\pm\, e^\mp, \qquad \mu^- N \to e^- N,
\tag{2.6}
$$

are greatly suppressed in the standard model. Since they can only occur through mixing of the neutrino flavor eigenstates, their branching ratios are proportional
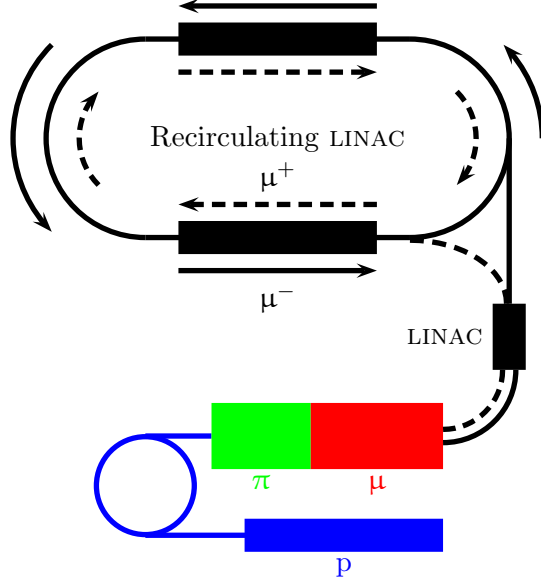
Figure 2.5: Illustration of the front end of a μC or νF with proton driver in blue, π-production target in green, μ cooling channel in red, and first stages of μ reacceleration in black. (Not drawn to scale.)

to $(m_\nu/m_W)^4$ and are of the order of 10^{-54} [51]. Branching ratios this small are unobservable; therefore observation of any LFV decays is a sign of new physics.

Many BSM physics models, such as SUSY, predict LFV branching ratios just below the current experimental upper limits [51–53]. Experiments using muons from the front end of a muon collider or neutrino factory could improve the upper limits on the branching ratios by 1 to 2 orders of magnitude at least [49].

2.3 COLLIDER SCHEMES

Muon beams are tertiary beams: A multi-MW multi-GeV proton driver bombards a target (figure 2.5), producing a large flux of secondary particles—mostly charged pions. A strong (≈ 20 T) solenoidal magnetic field collects the pions exiting the target and guides them down a channel at energies spread broadly between 50 MeV and 500 MeV. The magnetic field strength is tapered down to a few tesla over the length of the channel (order 10 m). The pions decay in the channel, producing muons with momenta also on the order of 10^2 MeV/c.

The resulting muon beam is intense, but occupies too-large a volume in momentum and coordinate space to be efficiently accelerated, let alone yield an interesting collision luminosity. The phase-space volume of the beam, called its emittance, must be reduced. This process is called cooling because it involves reducing the temperature of the beam in its comoving frame.

After the beam is cooled, it is accelerated up to GeV energies, at which it can be stored in a ring for use in a neutrino factory (figure 2.5), or further accelerated up to collision energies (figure 2.6). Beam cooling should take place
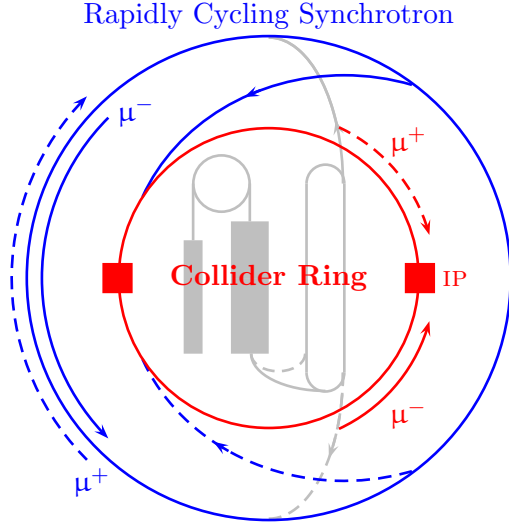
Figure 2.6: Illustration of a muon collider complex with the front end of figure 2.5 shown in gray, rapidly cycling synchrotron in blue, and the collider ring and interaction points in red. (Not drawn to scale.)

Center-Of-Mass Energy	[TeV]	0.4	3
μ/bunch	$[10^{12}]$	2	2
Collider Ring Diameter	[km]	0.16	1
$\Delta p/p$	[%]	0.16	0.14
ϵ_6	$[10^{-10}\pi\text{m}^3]$	1.7	1.7
β^*	[cm]	2.6	0.3
σ_z	[cm]	2.6	0.3
σ_r	[μm]	26	3.2
σ_θ (at IP)	[mrad]	1.0	1.1
Turns		700	785
Luminosity	$[\text{cm}^{-2}\cdot\text{s}^{-1}]$	10^{33}	7×10^{34}

Table 2.2: Low-energy and high-energy muon collider parameters, from [54].

on a timescale short enough to allow for a high efficiency, so that a high enough luminosity is achieved so that the beam can circulate around a collider ring $\mathcal{O}(1000)$ times before muon decays decrease the luminosity to an uninteresting level.

Many schemes have been proposed for the front end of a muon collider (for examples, see [14, 54, 55]). All these schemes have the same building blocks as the general scheme described above. They differ in the parameters of the proton driver, the mechanics of the pion production target, and the method of cooling the resultant muon beam. Some typical parameter sets are listed in table 2.2.

Beam Power	4 MW
Kinetic Energy	2–15 GeV
Repeitition Rate	50 Hz
Bunches/Train	3
Bunch Length	1–3 ns
Minimum Bunch Spacing	17 μs
Maximum Bunch Train Length	40 μs

Table 2.3: Proton driver parameters, from [58].

2.4 R&D CHALLENGES

The scheme described above is technically complicated. A twenty-year research and development effort has been devoted to overcoming the difficulties involved in constructing a muon collider. The following sections describe the major technical concerns and the research projects addressing them.

2.4.1 *Proton Driver*

There are many constraints placed on the proton driver for the efficient production of muon beams: Simulation of pion production with the MARS software [56] found that for proton energies between 2 GeV and 15 GeV, the pion yield is fairly flat with a broad peak at 7 GeV [57]. The timing of the bunch train must be optimized to fit the pion production target (see section 2.4.2). The length of the proton bunches must be short, allowing for efficient collection and cooling of the downstream muons. Muon-reacceleration requirements (see section 2.4.4) place a lower limit on proton bunch spacing. These requirements are summarized in table 2.3.

Over the last 30 years, the highest power achievable at a proton accelerator has increased from 10^{-1} MW to greater than 1 MW. Figure 2.7 shows the energies and powers of some of the highest-power proton accelerators built or planned [59]. Overlaid on this plot in green are the energies and powers of the proton drivers used in the schemes of references [14, 54, 55]; they range in power from 1 MW to 4 MW, and in energy from 2 GeV to 24 GeV.

These driver parameters are not very far beyond current capabilities. The Paul Scherrer Institute (PSI) in Switzerland has neutron and muon sources incorporating a 1.3-MW 590-MeV proton beam [60]. The Japan Proton Accelerator Research Complex (J-PARC) is home to a 1-MW 3-GeV beam (J-PARC RCS in figure 2.7), and a 0.75-MW beam of energies up to 50 GeV [61] (J-PARC MR). The 3-GeV beam is part of a high-intensity muon source [62] that has produced muons with 120 kW of proton beam power and will soon run with the full 1 MW [63].

The Fermi National Accelerator Laboratory (FNAL) is currently designing a 2-MW proton driver for a possible energy range from 2 GeV to 120 GeV (shown in yellow in figure 2.7). The proton driver program, named Project X, is being
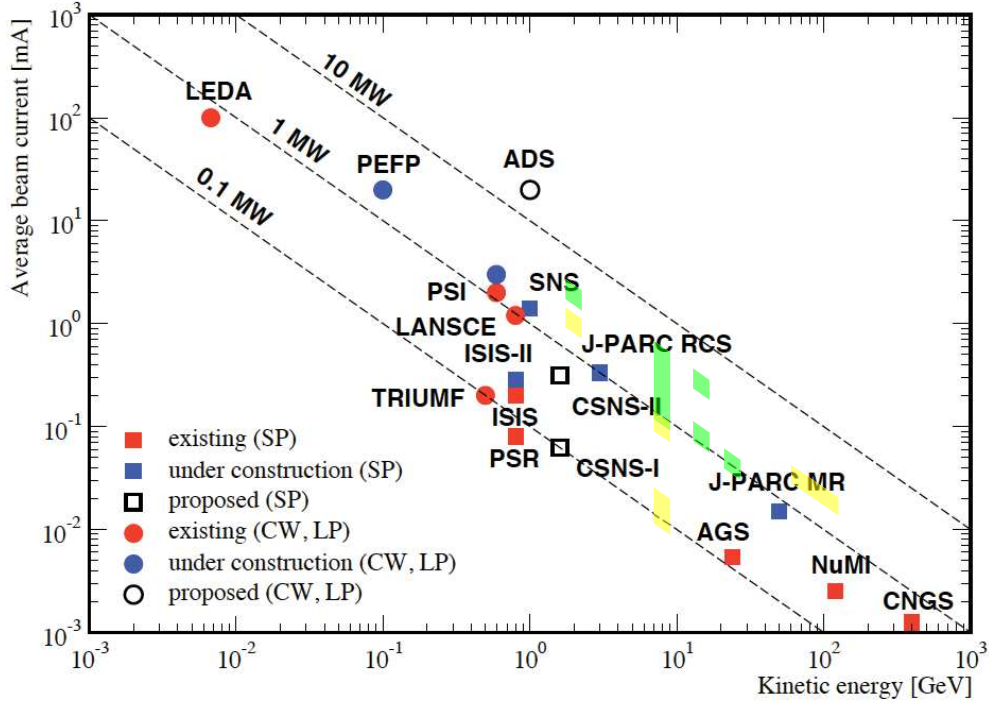
Figure 2.7: Beam currents and energies for high-power proton accelerators of three types: short pulse (SP), long pulse (LP), and continuous wave (CW). Taken from [59] with proposal and construction statuses as of 2006. The green markers show the proton drivers proposed in many muon collider schemes. The yellow markers shows the beams of the proposed first stage of FNAL's Project X.

developed for a staged upgrade plan [64] that would provide beams for neutrino experiments, muon and kaon experiments, and finally a neutrino factory and muon collider [65].

Two initial design reports (ICDs) have been published [66,67], each containing a GeV-energy linear accelerator (8 GeV for ICD-I; 2 GeV for ICD-II) as a first stage. The beam would then be split off to numerous experiments requiring unique beam setups. For long-baseline neutrino-oscillation experiments, 2 MW of the beam would be accelerated to 60 GeV–120 GeV to produce a pion-decay neutrino beam. Simultaneous to this, low-energy muon and kaon physics experiments would use a further 100 kW of beam power per experiment from the linear accelerator. The beam would then be upgraded to provide 4 MW for muon beam production for a μC or νF.

2.4.2 Pion Target

The production of pions, and subsequently muons, from an initial proton beam is not a new idea. The facilities mentioned above are accomplishing this with the current level of proton beam power (less than or approximately 1 MW). These

facilities bombard solid targets with their proton beams. This works well at the lower-power, but higher-power beams require new target technology that can withstand the higher-intensity bombardment.

The most-promising solution to this challenge is the use of a liquid-metal target. The Mercury Intense Target (MERIT) experiment successfully tested a liquid-Hg target in the proton beam of the CERN Proton Synchrotron (PS) in 2007 [68]. The experiment utilized a free liquid target—a 1-cm-diameter liquid jet with no housing—traveling at 20 m/s in the cavity of a superconducting solenoid magnet capable of providing field strengths up to 15 T. The PS provided proton beams of energies up to 24 GeV with single pulse intensities equivalent to those of a 4-MW beam.

Using this setup, the MERIT experiment demonstrated that a free liquid-Hg target could withstand the energy deposition of a high-power proton beam. Though being hit by the beam caused the jet to explode, the strong pion-collection magnetic field helped keep the jet consolidated long enough to function for a full proton bunch train after which it was replaced by the flow of mercury in the jet.

Such a target scheme places a limit on the length of the proton bunch train that it cannot be longer than tens of microseconds (table 2.3).

2.4.3 *Muon Cooling*

Perhaps the toughest challenge to be overcome in producing a muon beam is that of cooling. The short lifetime of the muon necessitates that beam preparation be accomplished on time scales less than a μs. To achieve the luminosities of 10^{34} cm$^{-2} \cdot$ s^{-1} the schemes in [14,54,55] prescribe, the accelerated muon beams must have normalized (6D) emittances $\epsilon \sim 10^{-10}$ $(\pi\text{m})^3$. In all of the schemes, the precooled muon beams (upon exiting the pion decay channel) have transverse position and momenta spreads of $\mathcal{O}(\text{cm})$ and $\mathcal{O}(10\,\text{MeV/c})$; and longitudinal spreads of $\mathcal{O}(10\,\text{m})$ and $\mathcal{O}(10^2\,\text{MeV/c})$. This means an initial emittance $\epsilon_0 \sim 10^{-4}$ $(\pi\text{m})^3$. Thus, to achieve the desired luminosity, the beam must be cooled by six orders of magnitude.

Two concepts are proposed for achieving this level of cooling without losing too-large a percentage of the beam to decay: ionization cooling (discussed below) and frictional cooling (discussed in chapter three).

IONIZATION COOLING

When a charged particle passes through matter, it decelerates in the direction of its velocity by interacting with the surrounding medium, mainly through ionization. Restoring the energy lost to the medium in only one direction (the longitudinal direction) through reacceleration reduces the dispersion of the beam with respect to this direction. This can counteract the dispersion created by focusing the beam in the transverse plane. Applying the three actions together, focusing, isotropic energy loss, and directional energy replacement, reduces the transverse emittance of a beam of particles. This is known as transverse (4D) ionization cooling [69, 70].
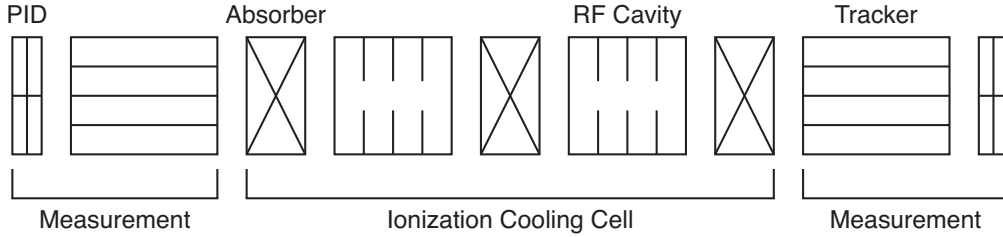
18

Figure 2.8: Diagram of the MICE experiment (magnets not shown).

Using a dipole to introduce a position–momentum correlation and then passing higher-energy particles through more of the medium, 6D cooling is achieved. If the beam is in the energy region above the ionization minimum (figure 3.1), longitudinal cooling is aided by the increase of the energy loss to the medium with increasing kinetic energy: faster particles lose more energy than slower particles, but all have the same amount of energy restored during reacceleration.

The effects of ionization energy losses on a beam of particles were first discussed in 1965 in [71], and it was quickly realized that the scheme described above could be used to cool the beam [72]. The principles were applied to electron cooling [73], wherein the retarding medium was replaced by a beam of electrons comoving with the beam to be cooled, but not developed for a solid medium, since it was deemed either ineffective or less effective than other schemes for cooling proton or electron beams [74].

However, ionization cooling was later investigated as a scheme for cooling beams of muons [69, 74]. Since then several ionization cooling schemes for a neutrino factory or muon collider have been proposed [54, 75, 76] and a proof-of-principle experiment is currently being constructed.

MUON IONIZATION COOLING EXPERIMENT

The Muon Ionization Cooling Experiment (MICE) is an international collaboration building up an experiment in stages to test ionization cooling [77, 78]. In its final stage it will contain an ionization cooling cell of the type described in [79] that will demonstrate a 10% emittance reduction of an input muon beam of momenta 140–240 MeV/c produced by the ISIS proton beam at the Rutherford Appleton Laboratory (RAL).

The MICE cooling cell consists of three absorber stages and two radio frequency (RF) acceleration cavities (figure 2.8). The absorber stages each contain a cavity for a liquid hydrogen (or lithium hydride) volume flanked on both sides by strongly focusing solenoid magnets. The RF cavities provide electric fields up to 16 MV/m in strength, and sit inside large-diameter solenoid magnets capable of providing fields up to 3 T in strength [80].

The emittance of the muon beam is measured directly before and after the cooling cell by measuring each muon's transverse position (x, y), transverse divergence $(dx/dz, dy/dz)$, total momentum, and time [81]. The position, divergence, and momentum are measured by scintillating-fiber trackers placed in a 4-T solenoid magnet. The tracker consists of five stations spaced out over

		LINAC	RLA	RLA	RLA	RCS	RCS	RCS
Initial Energy	[GeV]	0.10	0.70	2	7	50	200	1000
Final Energy	[GeV]	0.70	2	7	50	200	1000	1500
Length/Circ.	[km]	0.07	0.12	0.26	1.74	4.65	11.30	11.36
Turns			2	8	10	11	15	27	17
ΔE/turn	[GeV]	0.4	0.17	0.5	4	10	30	30
Acc. Gradient	[MV/m]	8	8	10	10	15	25	25
Muon Losses	[%]	6.1	12.3	10.8	14.0	10.7	10.1	2.7

Table 2.4: Acceleration stages of a 3-TeV muon collider, from [15].

1.1 m. Each station contains three double planes of tracking fibers rotated 120° from each other about the longitudinal direction. The time is measured by time-of-flight (TOF) and Čerenkov detectors placed before the first tracker and after the second.

To make these measurements, the beam must be let into the experiment one muon at a time. As well, to obtain the desired 1% uncertainty on the 10% cooling effect, background from pions and electrons must be supressed. This is achieved through particle identification (PID) by the TOF detectors and an electromagnetic calorimeter placed after the second tracker.

The staged construction and testing of the MICE experiment consists of first installing the PID and tracker detectors; then introducing an absorber between them; then two absorbers with one RF cavity between them; and finally the full cooling cell. As of 2010, the muon beam line has been completed; the two trackers have been constructed and tested with cosmic-ray muons; the first absorber has been constructed; the RF cavities have been designed; and the building up the first stages in the beam line should commence soon [80]. The full cooling cell test is expected in 2012.

2.4.4 *Reacceleration*

After exiting the cooling channel, the muons must be rapidly accelerated up to GeV energies, at which their lifetime is extended in the lab frame. This is achieved by a combination of linear accelerators (LINACs) and storage ring arcs, known as recirculating linear accelerators (RLAs).

Figure 2.5 shows the initial reacceleration components following the muon cooling channel, based on the scheme of [15], which are common to a low-energy and a high-energy muon collider: the muons are linearly accelerated to 700 MeV. They then pass through multiple RLAs, each consisting of race-track-shaped rings (such as shown in figure 2.6), of increasing size that accelerate the beam up to 70 GeV. Rapidly cycling synchrotrons (RCS) then accelerate the beam up to the collider energy, after which they are transferred to the collider storage ring. This acceleration could be truncated at the desired energy for a neutrino factory, and the muons transferred to a race-track-shaped storage ring for the generation of neutrino beams. These components are summarized in table 2.4. Research and
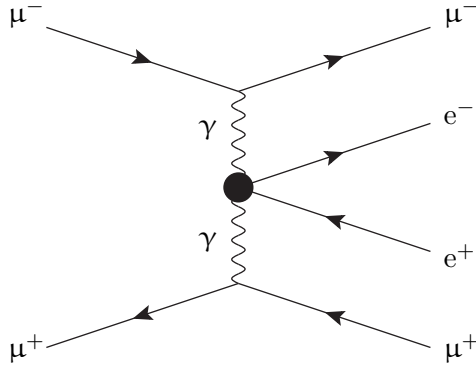
Figure 2.9: Incoherent e^+e^- pair production.

development for the acceleration phases of a muon collider are focused on the RCSs.

2.4.5 *Detector Backgrounds*

Another major challenge to be overcome in building a muon collider experiment is the suppression of background signals in an interaction point (IP) detector. There are three main sources of background: electrons from incoherent pair production at the IP, muons from the beam halos, and the showers of particles produced when electrons from beam decay hit the material surrounding the beam pipe. These background sources have been studied extensively; detailed calculations can be found in [15, 82, 83]. The following discussion is based on their results.

LOW-ENERGY PAIR PRODUCTION

The total cross section for the incoherent pair production of electrons and positrons (figure 2.9) is $\mathcal{O}(\mathrm{mb})$ (for example, 10 mb at $\sqrt{s} = 4$ TeV [84]). Though most of the electrons have small transverse momenta, they can be deflected by the large magnetic fields created by the beams. The electrons are confined within a particular radius of the beam axis by the magnetic field of the detector: at a field strength of 2 T, only 10% of the electrons travel more than 10 cm from the beam axis; at 4 T none of the electrons travel beyond this radius [82].

This background source is of great importance in the design of the vertex detector. The high fluence at centimeter radii can limit the smallness of the inner radius of the vertex detector. The uncertainty on measuring the location of an interaction vertex grows linearly with the inner radius of the detector. Whereas many detectors—for example, the Tevatron's D0 and CDF, and the proposed International Linear Collider detectors have inner radii between 1 cm and 2 cm, the muon collider detector may have to have an inner radius of 5 cm or larger. This is due to the production of higher-energy electrons at a muon collider in the interaction region, which will spiral around the beam axis at larger radii.

The beam halo is comprised of muons that deviate from the design orbit of the collider ring. They may enter the ring already off orbit (at beam injection) or be deflected at the IP or through interactions with residual gas in the beam pipe. During final focusing before the IP they can then be deflected into the detector.

The halo particles arising at beam injection will leave the beam pipe within the first several cycles around the ring. The halo regenerated by the ring itself can be "scraped": beam particles at a specified transverse distance to the beam center (typically $3\sigma_{\text{trans}}$) are removed by magnetic collimators (toroidal magnets) that deflect them away from the beam path and detectors. Since muons can travel very long distances through matter before stopping, scraping must take place away from the IP. Precise modeling of the beam-halo background in the detector is possible but can only be done after the collider-ring lattice has been specified.

DECAY BACKGROUND

The largest source of background in the interaction region will come from the electrons emitted by muons decaying upstream of the interaction point in the final focus region of the collider ring (130 m on either side of the IP). These electrons follow the muon beam trajectories until they encounter a focusing magnetic, which deflects them out of the beam pipe. The high-energy electrons (~ 500 GeV) radiate synchrotron photons in the magnetic fields and when they hit the material surrounding the beam they produce electromagnetic showers of electrons, photons, hadrons, and muons.

It is important to shield the detector from the decay electrons' showers, so that no active components of the detector see a surface that is irradiated by them. As well, the neutrons and muons produced in any shielding must themselves be shielded against. The long lifetime of the neutron allows it to migrate slowly into the detector and produce a detector signal asynchronous to the bunch crossing that produced it. High-energy muons (~ 10 GeV)—called Bethe Heitler (BH) muons for their coherent production process—are created when the high-energy electrons first hit the beam pipe or magnets, upstream of the IP. Since muons are very penetrating, these BH muons can easily reach the detector, unless they are shielded against.

SHIELDING

To prevent the decay electrons and the neutrons and muons they produce from reaching the detector, shielding is placed inside and around the beam pipe in the detector region. The following shielding scheme is common to all the studies referenced above. The outside of the beam pipe is surrounded by a cone of tungsten that begins approximately 3 cm from the IP and widens out further down the beam line (figure 2.10). Three angles at which the shielding could extend from the IP were studied: $9°$, $20°$, and $30°$.

The shielding inside the beam pipe consists of tungsten beginning 6.5 m from the interaction point and narrowing down to approximately $4 \cdot \sigma_{\text{trans}}$ at 1.1 m
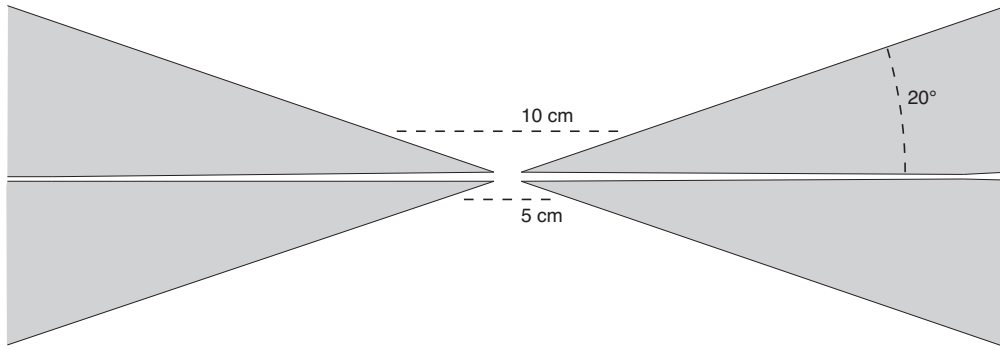
Figure 2.10: Tungsten shielding around the IP (1.1 m shown on either side) with a 20° angle.

from the IP. It then widens at an angle approximately $4 \cdot \sigma_\theta$ (the divergence of the beam) from 1.1 m to the IP, so as to prevent any surviving decay electrons from producing showers on a surface inside the detector. The outer section of shielding also contains neutron traps consisting of copper surrounded by poly-boron. Some of the background studies consider placing such traps inside the detector structure as well.

With such shielding, only approximately 2% of the decay electrons interact with the shielding near the IP; 30% are stopped by the shielding beyond 1.1 m; 58% are stopped further upstream; and 10% pass through the interaction region without leaving the beam pipe [83].

While such shielding is necessary to run the detector, it may greatly impact the ability to make precise physics measurements. The background in the detector can also be reduced by decreasing the population of the muon bunches, allowing for shallower angles of the conical shielding outside the beam pipe. Chapter three presents an alternative to ionization cooling that can deliver the same luminosity with an order of magnitude fewer muons per bunch. As well, the impact of limited angular acceptance in the detector on the study of a particular model of BSM physics is presented in chapter nine.

CHAPTER 3

Frictional Cooling

Like ionization cooling, frictional cooling involves balancing energy losses to a retarding medium with energy gains from an electric field to bring a beam of particles to an equilibrium energy and reduce beam dispersion. Both methods require the establishment of an attractive equilibrium energy. Whereas ionization cooling takes place at high energies (hundreds of MeV and greater) and may require acceleration of the pion or muon beams by RF cavities before they enter a cooling cell; frictional cooling takes place at low energies (tens of keV and lower) and requires muons be slowed down before they can be cooled.

3.1 WORKING PRINCIPLE

Figure 3.1 shows the stopping power for helium on μ^+ and the acceleration power of an electric field of fixed strength E on a particle of constant unit charge. The stopping power is velocity scaled for μ^+ (see section 3.2.1) from the proton data given in [85]. The stopping power for μ^- has a similar shape, though it is smaller in magnitude at energies below approximately 100 keV [86, 87]. When the accelerating power is larger than the stopping power, the particle is accelerated. When the reverse is true, the particle is decelerated. At the kinetic energies where the two curves intersect, particles are neither accelerated nor decelerated, establishing an energy equilibrium. If the stopping power is greater than the accelerating power at energies above the equilibrium energy and the reverse is true at energies below it, then the equilibrium point is stable and attractive.

For a particle of constant charge, two equilibrium points are created: a stable one (T_{eq} in figure 3.1) at an energy below that at which the stopping power peaks, and an unstable one at an energy above (T'_{eq}). Particles with $T_{eq} < T < T'_{eq}$ will decelerate to T_{eq} and particles with $T < T_{eq}$ will accelerate to T_{eq}, defining the frictional cooling energy region.

Straggling of the energy losses to the medium prevent a beam of muons from becoming truly mono-energetic in a frictional cooling scheme, inducing a spread of the beam energy around T_{eq}. A study of frictional cooling with μ^- in [88] found that the spread of the energy distribution of a cooled beam is independent of the beam's initial spread and decreases with increasing gradient of the stopping power (figure 3.2).

The muons also scatter off the nuclei of the stopping medium. Without scattering, just as with ionization cooling (where scattering is negligible), the
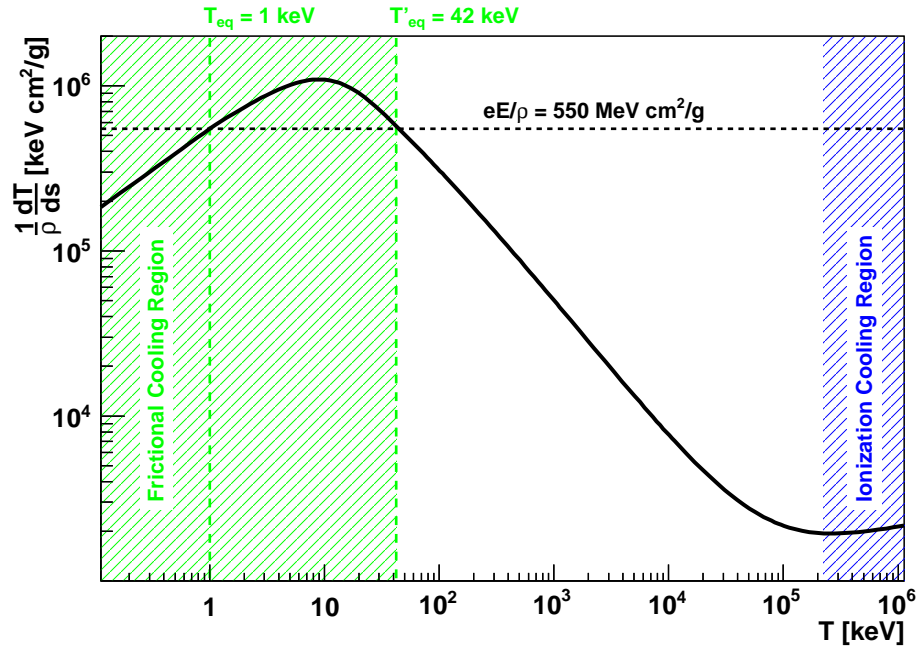
Figure 3.1: Stopping power of helium on μ^+ (velocity scaled from [85]) and the acceleration power of an electric field of fixed strength E for a particle of constant unit charge as functions of particle energy T.

beam divergence is reduced, since muons lose energy along the direction of motion but gain energy only in the direction of the electric field. Scattering counteracts this divergence reduction, and—independent of the initial beam conditions—creates a mean divergence of $\sim 20°$ with an rms of $\sim 10°$ for keV equilibrium energies [88].

Nuclear scattering contributes to the spread in kinetic energies of the cooled beam to a larger extent than straggling of the energy losses. This is due to muons scattering away from the electric field direction, possibly even at a large angle, sending it in a direction opposed to that of the field; they are then slowed down and reaccelerated to the equilibrium energy in the direction of the field (figure 3.13b, explained in more detail in section 3.5.1).

3.2 LOW-ENERGY STOPPING PROCESSES

At high kinetic energies, a projectile slows down in a medium through excitation and ionization of the electrons of the medium atoms. One can assume that the interactions with the nuclei of the medium are negligble and that a positively charged projectile is stripped of all its electrons [89, 90]. Thus the stopping power of the medium for positively charged particles is the same as for negatively charged ones. This is the energy region of ionization cooling, and the energy loss here is comparatively simpler to model than energy loss at low energies, the region of frictional cooling.
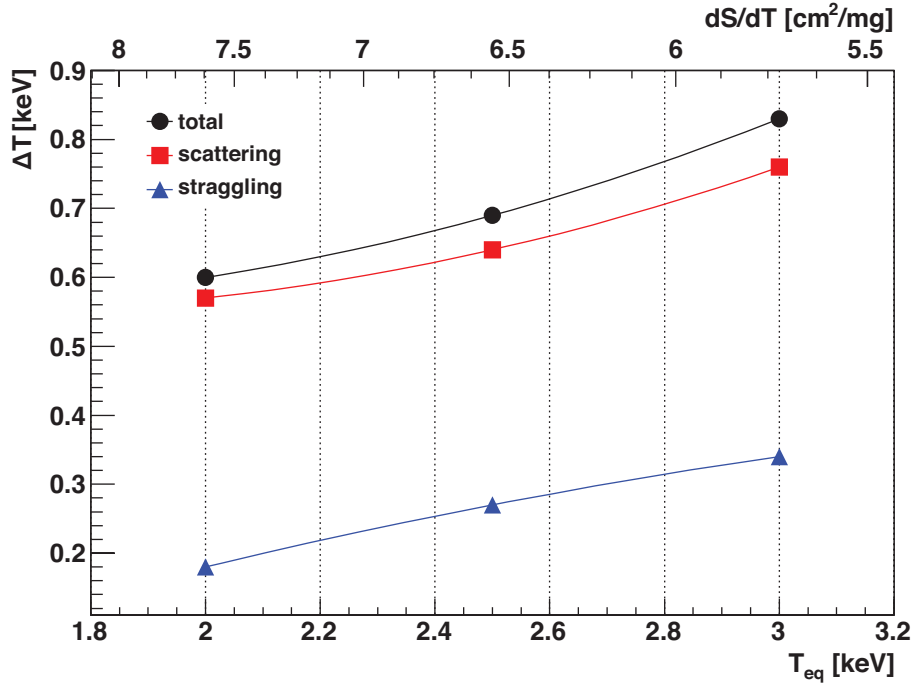
Figure 3.2: Energy spread of a frictionally cooled μ^- beam as a function of equilibrium energy, from [88] with H_2 gas as the stopping medium. The upper axis displays the gradient of the stopping power with respect to kinetic energy for H_2 on μ^- at T_{eq}.

At low energies, massive charged particles slow down by Coloumbic interactions with both the nuclei and the electrons of the medium; furthermore the interactions of positively charged projectiles with the medium electrons involve more than excitation and ionization, leading to a difference in the stopping powers for positive and negative projectiles.

3.2.1 *Velocity Scaling*

In the following discussion, except where noted, the data for μ^+ interactions are velocity scaled [91] from proton data. This is done by assuming that the cross sections for muon interactions and those of proton interactions are the same at equal velocity,

$$\sigma_\mu(v) = \sigma_p(v). \tag{3.1}$$

In terms of the particle energies,

$$\frac{E_\mu}{m_\mu} = \frac{v^2}{2} = \frac{E_p}{m_p}, \tag{3.2}$$

muon cross sections are calculated from proton cross sections according to

$$\sigma_\mu(E_\mu) = \sigma_p\left(\frac{m_p}{m_\mu}E_\mu\right). \tag{3.3}$$

27
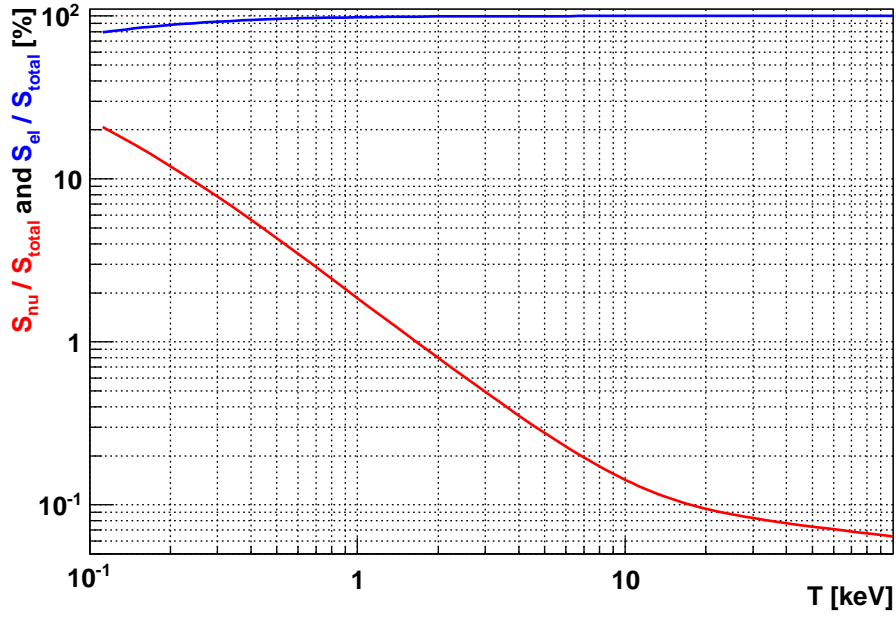
Figure 3.3: Fraction of the total stopping power ($S_{\text{total}} = S_{\text{el}} + S_{\text{nu}}$) for the electronic stopping power (S_{el}) and the nuclear stopping power (S_{nu}) for helium on μ^+, from [85].

3.2.2 *Nuclear Stopping*

Scattering of the projectile particle off of a nucleus of the stopping medium results in a loss of energy and a change of direction. This process has been well-described by theory that is matched to experimental data [90, 92].

Though, as described above, nuclear scattering has the largest impact on the final energy spread of a cooled μ^- beam, it is not the main mechanism of energy loss. As figure 3.3 shows, the nuclear stopping power (S_{nu}) is orders of magnitude smaller than the electronic stopping power (S_{el}) for all but the lowest kinetic energies.

3.2.3 *Electronic Stopping*

The interactions of the projectile[*] with the electrons of the stopping medium are the dominant mechanisms of energy loss. In the frictional cooling energy region these interactions are the excitation and ionization of electrons of the medium atoms (X),

$$\mu^{(+)} + \text{X} \quad \rightarrow \quad \mu^{(+)} + \text{X}^* \tag{3.4a}$$

$$\mu^{(+)} + \text{X}^q \quad \rightarrow \quad \mu^{(+)} + \text{X}^{q+n} + n\text{e}^- \tag{3.4b}$$

---
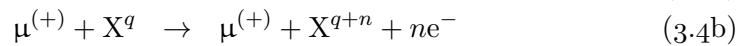
[*]The equations to follow are equally valid with μ^+ and Mu replaced by p and H.

and the capture and loss of an electron by the projectile,

$$\mu^{(+)} + X^q \quad \rightarrow \quad \mu^{(0)} + X^{q+1} \qquad\qquad (3.4\text{c})$$

$$\mu^{(0)} + X^q \quad \rightarrow \quad \mu^{(+)} + X^q + e^- \qquad\qquad (3.4\text{d})$$

$$\mu^{(0)} + X^q \quad \rightarrow \quad \mu^{(+)} + X^{q-1}, \qquad\qquad (3.4\text{e})$$

where we have introduced the notation $\mu^{(q)}$ to represent charge states of μ^+ as an ion of muonium (Mu):

$$
\begin{aligned}
\mu^{(+)} &= \text{Mu}^+ &= \mu^+, \\
\mu^{(0)} &= \text{Mu} &= \mu^+ e^-, \text{ and} \\
\mu^{(-)} &= \text{Mu}^- &= \mu^+ e^- e^-.
\end{aligned}
$$

It is obvious from the above processes that the slowing down of the neutral charge state plays a role in the slowing down of the positive charge state. Processes (3.4a)–(3.4e) must also be considered with the replacement of $\mu^{(+)}$ by $\mu^{(0)}$, and $\mu^{(0)}$ by $\mu^{(-)}$. Further processes involving the negative charge state must also be included: (3.4a) and (3.4b) with the replacement of $\mu^{(+)}$ by $\mu^{(-)}$, and double electron capture and loss

$$\mu^{(+)} + X^q \quad \rightarrow \quad \mu^{(-)} + X^{q+2} \qquad\qquad (3.4\text{f})$$

$$\mu^{(-)} + X^q \quad \rightarrow \quad \mu^{(+)} + X^{q-n} + me^-, \quad n + m = 2 \qquad (3.4\text{g})$$

The cross section for processes (3.4a)–(3.4g) for $\mu^{(+)}$, $\mu^{(0)}$, and $\mu^{(-)}$ are written with the notation $\sigma_{qq'}(T)$, denoting the total cross section for the processes taking a muon of charge state q and energy T to a muon of charge state q' (with an accompanied energy loss). To be clear, the charges q and q' refer to the charge state of the muonium ion $(+, 0, -)$, not to the charge of the individual muon itself, which remains positive in these purely electromagnetic interactions.

The total stopping power of the projectile is the combination of the individual stopping powers of the different charge states,

$$
\begin{aligned}
S(T) &= \sum_q f^q(T) S^q(T) \\
&= f^+(T) S^+(T) + f^0(T) S^0(T) + f^-(T) S^-(T), \qquad (3.5)
\end{aligned}
$$

where the f^q are the equilibrium charge state fractions [93], which are the solutions to

$$\frac{\mathrm{d}f^q}{\mathrm{d}x} \propto \sum_{q'} \left(f^{q'} \sigma_{q'q} - f^q \sigma_{qq'} \right) = 0, \qquad \forall q, \qquad (3.6)$$

and

$$\sum_q f^q = 1. \qquad\qquad (3.7)$$

where $\mathrm{d}f^q/\mathrm{d}x$ is taken at a fixed T, and so the f^q are functions of T. For the three-component system $(\mu^{(+)}, \mu^{(0)}, \mu^{(-)})$, the equilibrium charge states are

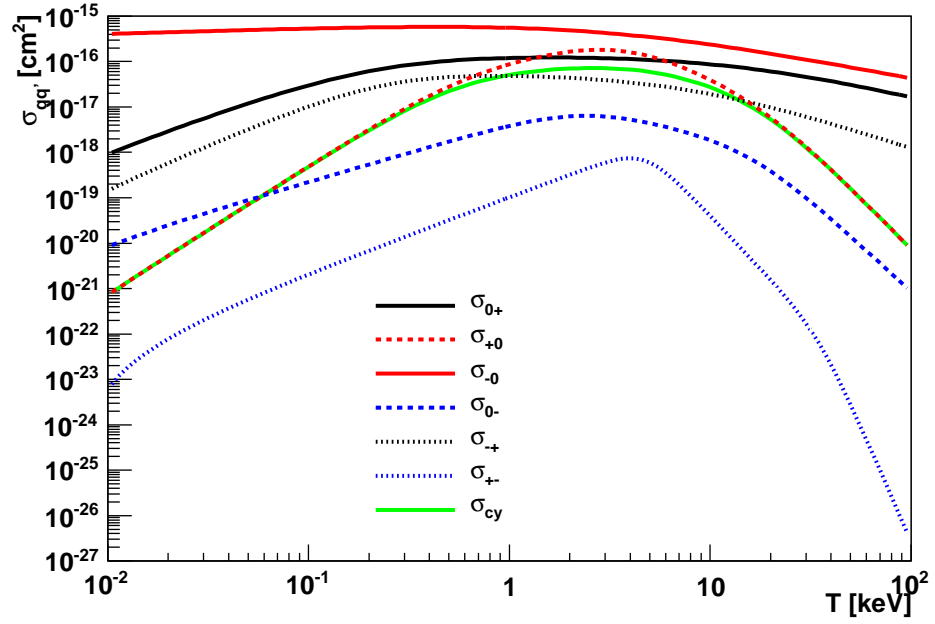$$f^q = A^q \left/ \sum_{q'} A^{q'} \right., \qquad\qquad (3.8\text{a})$$

Figure 3.4: Charge exchange cross sections for μ^+ in helium velocity scaled from proton cross sections in [94]: single electron loss (solid), single electron capture (dashed), and double electron capture and loss (dotted) resulting in final states with $\mu^{(+)}$ (black), $\mu^{(0)}$ (red), and $\mu^{(-)}$ (blue). The two-state charge exchange cycle cross section is shown in solid green.

where

$$A^q \equiv \sum_{i \neq j \neq q} \sigma_{ij}\sigma_{jq} + \prod_{i \neq q} \sigma_{iq} \tag{3.8b}$$

The stopping power shown in figure 3.1 is by the nature of its measurement [85] the total stopping power; that is, the left-hand side of equation (3.5).

3.3 EFFECTIVE CHARGE

It is clear from section 3.2.3 that when traveling through matter a μ^+ spends some time as Mu^0 and Mu^-. This changing of charge state will have a significant impact on the frictional cooling process, which involves the restoration of energy losses by an electric field according to qE.

Figure 3.4 shows the cross sections for the charge exchange processes of μ^+ in helium obtained by velocity scaling those for protons in [94]. The cross sections resulting in $\mu^{(-)}$ charge states are orders of magnitude smaller than those taking $\mu^{(-)}$ to $\mu^{(+)}$ or $\mu^{(0)}$. This means that a μ^+ traveling in helium (and in all the materials we will discuss) is nearly a two-state system consisting only of $\mu^{(+)}$ and $\mu^{(0)}$. This simplifies the calculation of the equilibrium charge
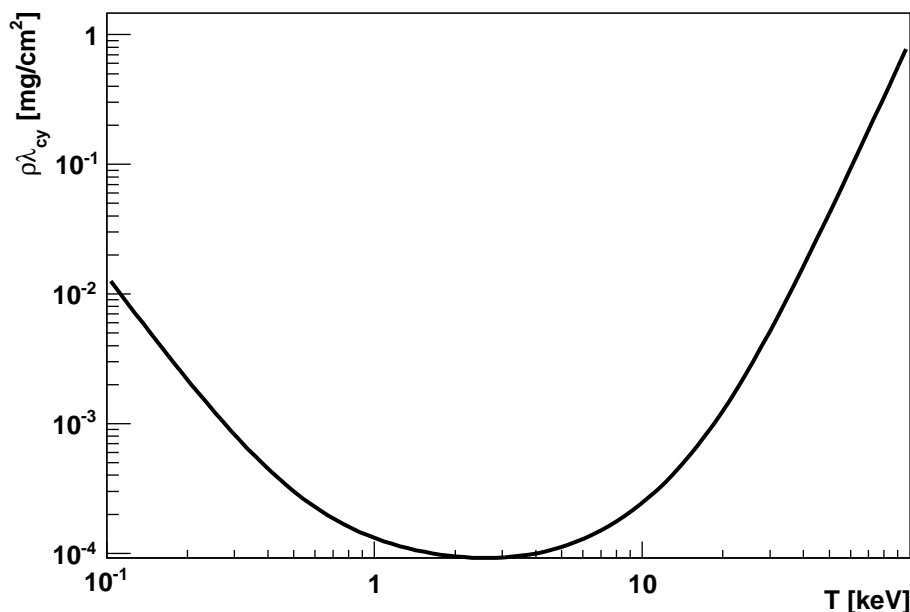
Figure 3.5: Mean free path for a two-state charge change cycle $\mu^+ \to Mu \to \mu^+$ in helium as a function of muon kinetic energy.

state fractions, which for the two-state system are

$$f^+ = \frac{\sigma_{0+}}{\sigma_{+0} + \sigma_{0+}} \quad \text{and} \quad f^0 = \frac{\sigma_{+0}}{\sigma_{+0} + \sigma_{0+}} \tag{3.9}$$

The mean free path for one charge change cycle $(\mu^{(+)} \to \mu^{(0)} \to \mu^{(+)})$ can be calculated from the mean free paths for the individual charge exchange processes, $\lambda_{\text{cy}} = \lambda_{0+} + \lambda_{+0}$. This yields a cross section for a charge exchange cycle to take place

$$\sigma_{\text{cy}} = \frac{\sigma_{+0}\,\sigma_{0+}}{\sigma_{+0} + \sigma_{0+}}. \tag{3.10}$$

The resulting λ_{cy} and σ_{cy} are shown in figures 3.5 and 3.4. Since the charge-state-changing interactions take place over distances much shorter than the overall distance the muon travels in the frictional cooling scheme, we can approximate the charge of the μ^+ by an effective charge according to

$$\eta \equiv \sum_q q f^q. \tag{3.11}$$

Figure 3.6 shows the effective charges of μ^+ in helium, hydrogen, and neon for both the two-state (η_2) and three-state (η_3) systems as calculated from the cross sections shown (for helium) in figure 3.4, which are calculated from empirical formulae from [95] fit to measured values [94]. The two-state effective charge is also shown for carbon—the three-state effective charge could not be calculated since the cross sections involving the negative charge state are unknown.
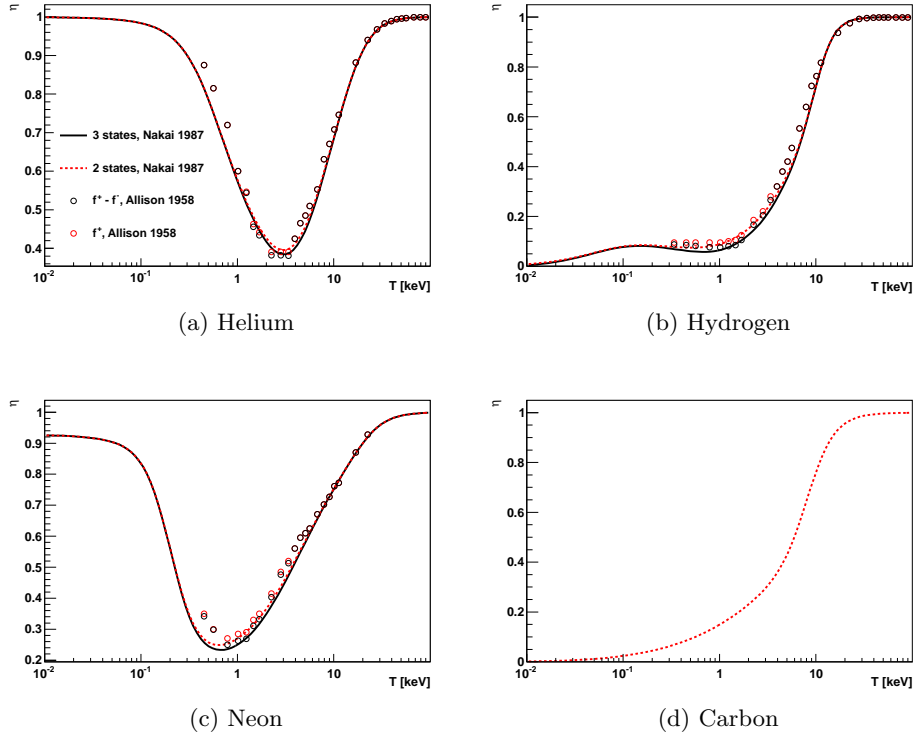
(a) Helium   (b) Hydrogen

(c) Neon   (d) Carbon

Figure 3.6: Effective charge (line) for μ^+ in He, H, Ne, and C for the three-state (solid black) and two-state (dashed red) systems. The data points show the equilibrium charge state fractions taken from [93]

For comparison to the calculated effective charge, we show experimentally measured charge state fractions from [93] for helium, hydrogen, and neon: f^+, which is the same as η_2; and $(f^+ - f^-)$, which is the same as η_3. The calculated effective charge matches very well with the measured data. As well, it can be seen that η_2 and η_3 differ only minutely and only over a small range of energy. The negative charge state fraction contributes to the three-state effective charge at percent level and lower in all three gases.

It is important to note that helium and neon are the only materials in which the effective charge of a positively charged projectile tends to a value of or near unity at low energies. In hydrogen and carbon (as well as water, oxygen, and nitrogen, and therefore air) the effective charge approaches zero at low energies.

3.3.1 *Accelerating Power & Gas Choice*

The effective charge of μ^+ in the retarding medium of a frictional cooling scheme can be absorbed into the accelerating power of the electric field. In effect, this makes the accelerating power dependent on the muon energy.

We reformulate here the requirements for frictional cooling discussed in section 3.1: An equilibrium energy must be established by balancing energy loss

	He	H$_2$	Ne	C	N$_2$	Ar	H$_2$O	O$_2$	Kr	Xe	
without η	8.4	6.2	14.1	9.6	9.0	7.9	9.0	10.7	9.0	9.0	keV
with η	3.9	0.9	1.1		0.33	0.23	4.5	3.1			keV

Table 3.1: Maximum energy at which a stable equilibrium can be established in a frictional cooling schemed for μ^+ with and without accounting for effective charge for several stopping media. A blank entry means no equilibrium energy can be established.

with energy gain,

$$S(T_{\mathrm{eq}}) = \frac{E}{\rho}\eta(T_{\mathrm{eq}}), \tag{3.12}$$

where ρ is the density of the stopping medium. At energies above T_{eq} the stopping power must be greater than the accelerating power

$$S(T_{\mathrm{eq}} + \epsilon) - \frac{E}{\rho}\eta(T_{\mathrm{eq}} + \epsilon) > 0. \tag{3.13a}$$

And at energies below T_{eq} the accelerating power must be greater than the stopping power

$$\frac{E}{\rho}\eta(T_{\mathrm{eq}} - \epsilon) - S(T_{\mathrm{eq}} - \epsilon) > 0. \tag{3.13b}$$

The last two equations can be combined to one statement about the slope of the stopping power relative to that of the accelerating power:

$$\left.\frac{\mathrm{d}S}{\mathrm{d}T}\right|_{T_{\mathrm{eq}}} - \frac{E}{\rho}\left.\frac{\mathrm{d}\eta}{\mathrm{d}T}\right|_{T_{\mathrm{eq}}} \equiv S'(T_{\mathrm{eq}}) - \frac{E}{\rho}\eta'(T_{\mathrm{eq}}) > 0. \tag{3.13c}$$

All three requirements are thus met when

$$S' - S\frac{\eta'}{\eta} > 0. \tag{3.14}$$

Figure 3.7 shows the slope of the stopping power relative to the accelerating power as a function of μ^+ kinetic energy for helium, hydrogen, neon, and carbon with and without accounting for effective charge. Highlighted in the plots is the sign of the slope. Only when the sign is positive can frictional cooling be accomplished. Accounting for the muon's effective charge greatly reduces the maximum energy at which the condition of equation (3.14) is met. Table 3.1 lists the cooling ranges for several materials with and without accounting for effective charge.

The effects of charge exchange processes also reduce the value of T'_{eq}, the maximum kinetic energy that can be deccelerated to T_{eq}. This effect is illustrated in figure 3.8, which shows the frictional cooling region of the stopping power of helium on μ^+. Superimposed on the stopping-power curve are three electric-field accelerating powers: The black dashed curve is the naive accelerating power of figure 3.1, with effective charge neglected, for a field strength
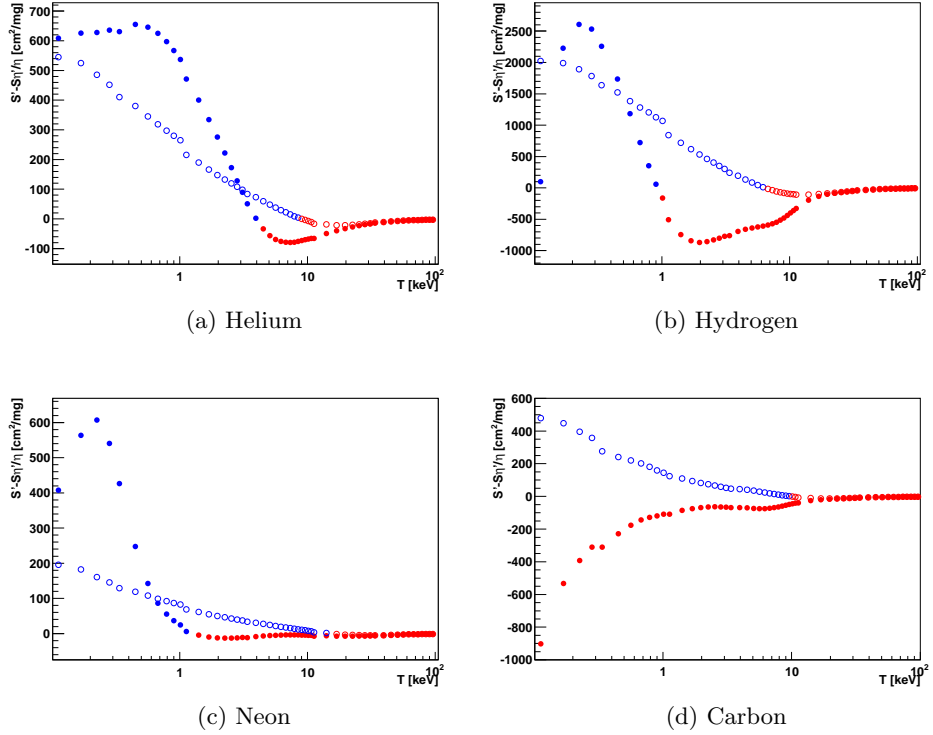
(a) Helium (b) Hydrogen (c) Neon (d) Carbon

Figure 3.7: Slope of the stopping power of the medium with respect to the accelerating power of the electric field for μ^+ in the helium, hydrogen, neon, and carbon with ($\bullet$) and without ($\circ$) accounting for effective charge. A blue marker indicates a positive relative slope, a red marker indicates a negative relative slope.

$560\,\mathrm{kV\,cm^2/mg}$ resulting in $T_{\mathrm{eq}} = 1\,\mathrm{keV}$. The lower red curve is the accelerating power for the same electric field strength, accounting for effective charge. The equilibrium energy is cut in half, but T'_{eq} remains the same. The upper red curve shows the accelerating power accounting for effective charge that results in $T_{\mathrm{eq}} = 1\,\mathrm{keV}$, which requires a field strength of $970\,\mathrm{keV\,cm^2/mg}$, and reduces T'_{eq} by a factor of two.

To achieve the desired equilibrium energy, accounting for effective charge, requires a greater electric-field strength than is expected in the naive scheme. The field strength may in fact have to be an order of magnitude larger, depending on what the desired T_{eq} and the stopping medium are (figure 3.9). On the bright side, as figure 3.7 indicates, for certain ranges of T_{eq}, the relative slope of the stopping power is larger when effective charge is accounted for, perhaps causing (according to [88]) the final energy spread of a cooled beam to be smaller.

The choice of stopping medium is even further limited than the requirement that the slope of the stopping power be greater than the slope of the accelerating power. This is illustrated by the example of oxygen as the stopping medium, as shown in figure 3.10: For oxygen, the relative slope of the stopping power
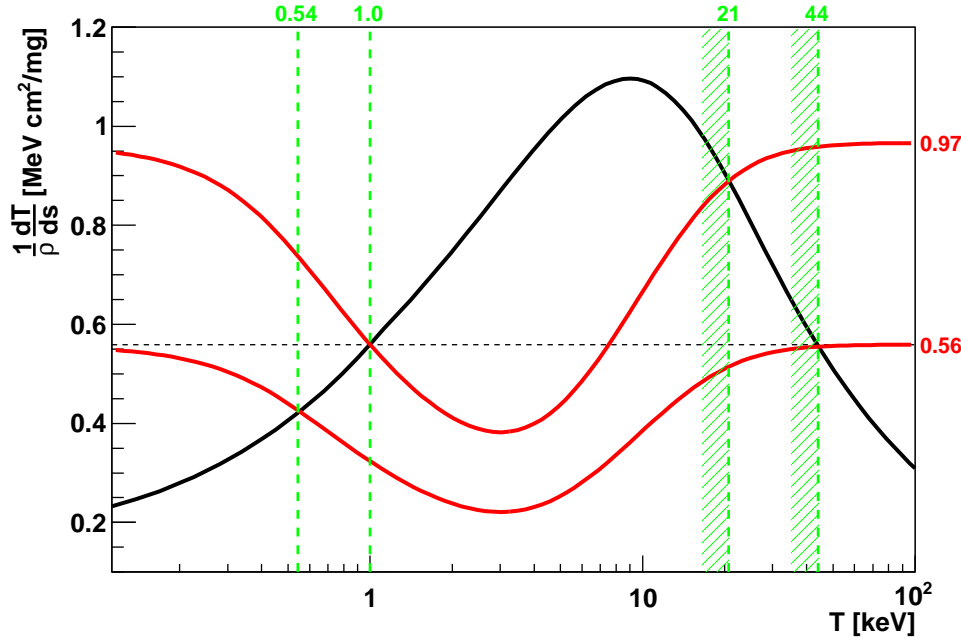
Figure 3.8: Stopping power of helium on μ^+ (black) and accelerating power of a uniform constant electric field of strength E on μ^+ in helium with (red) and without (dashed black) accounting for effective charge for two values of eE (as indicated on the right axis).

is just barely positive over a small region of energies; but it is not sufficiently large to clearly establish an equilibrium energy. In the figure, the stopping and accelerating powers have nearly identical shapes.

Furthermore, at low energies, the stopping power is proportional to the particle velocity, $S \propto T^{\frac{1}{2}}$, but η is proportional to T^k, with $k > \frac{1}{2}$, causing the accelerating power to decrease below the stopping power. A particle that experiences a large loss of energy in one interaction—or one that scatters into a direction opposite that of the electric field—will not reaccelerate up to T_{eq}, but rather continue decelerating to thermal energies and be lost to the cooling process. This would severely limit the use such a stopping medium in a frictional cooling scheme.

The only viable stopping media for a gaseous frictional cooling scheme for μ^+ with equilibrium energies at or above 1 keV are helium and water vapor. For T_{eq} just below 1 keV, hydrogen and neon also become viable; and for T_{eq} of a few hundred electron volts, argon and nitrogen are also viable.

3.3.2 Beam Neutralization & Foils

The frictional cooling experiment of [96] iterated energy loss and replacement by means of a series of moderating foils with electric fields between them. The experiment and a similar Monte Carlo simulation in [88] gave promising results
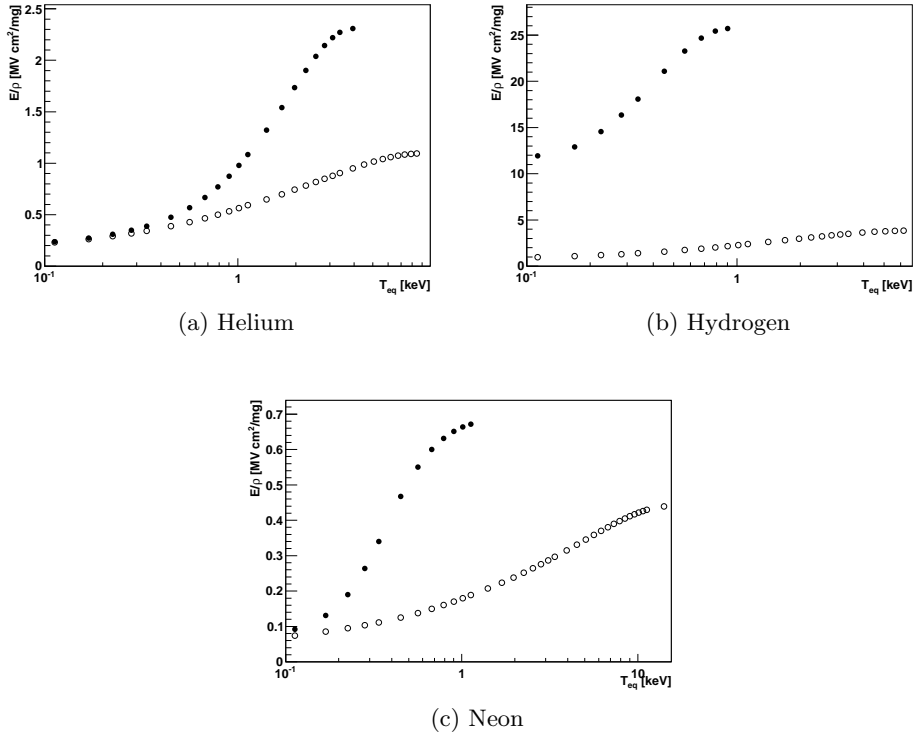
(a) Helium

(b) Hydrogen

(c) Neon

Figure 3.9: Electric field strength required to achieve the desired equilibrium energy as a function of equilibrium energy for μ^+ in helium, hydrogen, and neon with ($\bullet$) and without ($\circ$) accounting for effective charge.

for such a scheme for the cooling of negative muons. In both publications it was posited that the frictional cooling scheme used with μ^- could also work with μ^+; more recently this idea has been revisited in [97] and [98]. However, the presence of charge exchange interactions greatly limits the yield for such a scheme; in fact, leading to a zero yield.

A foil-based frictional cooling scheme has the benefit of using the full accelerating power of the electric field without needing to consider an effective charge, since the μ^+ are reaccelerated in vacuum between the foils of stopping material. However, particles that exit the moderator foils in the middle of a charge change cycle, being neutral, are blind to the reacceleration field.

The four studies cited above used or simulated carbon foils in their frictional cooling schemes. Since the reacceleration field can be chosen to precisely compensate the energy losses in the foils, with consideration of an effective charge unnecessary, according to table 3.1, T_{eq} can be as large as 9 keV. At this energy the positive charge state fraction f^+, equivalent to η_2 (figure 3.6), is already below 75% and drops rapidly to 15% at 1 keV. After exiting a foil of the cooling cell at an energy around T_{eq}, a beam of population N will be divided into two populations, a fraction $f^+(T_{eq})N$ in the μ^+ state and a neutralized fraction $(1 - f^+(T_{eq}))N$ in the Mu state. The μ^+ portion of the beam will be reacce-
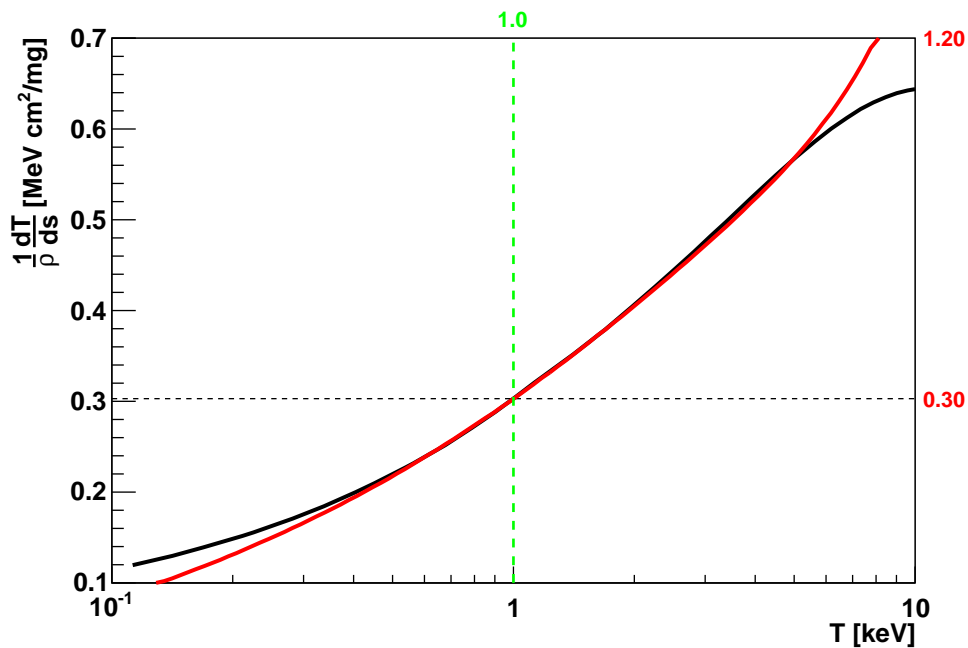
Figure 3.10: Stopping power of oxygen on μ^+ (black) and the accelerating power of a 1.2 MV cm^2/mg electric field with effective charge accounted for (red) and a 0.3 MV cm^2/mg electric field without effective charge (black dashed).

lareted towards T_{eq} and upon exiting the next foil in the cooling series, will have it's population further decreased to $(f^+(T_{eq}))^2 N$. The Mu portion of the beam will not have its energy losses to the previous foil restored by the electric field, and will exit the next foil at an energy now below T_{eq}, where f^+ is even smaller, and the chances of Mu atoms losing their electrons becomes smaller. As the beam passes through the array of foils it is neutralized and slowed down. Cooling becomes an impractical goal.

3.4 MUON CAPTURE

In accordance with the stopping-medium properties discussed above, the ideal gas choice for cooling μ^+ is helium. Negatively charged projectiles do not suffer from the effects of charge exchange processes, however they suffer from being captured into atomic orbits by the stopping medium atoms. Figure 3.11 shows the cross section for μ^- capture by a gaseous medium for the noble gases, from [99], and hydrogen, from [100]. The cross section falls very rapidly to zero in the 10s of eV range in hydrogen and helium gasses, making them the ideal choice for the cooling medium for μ^-.
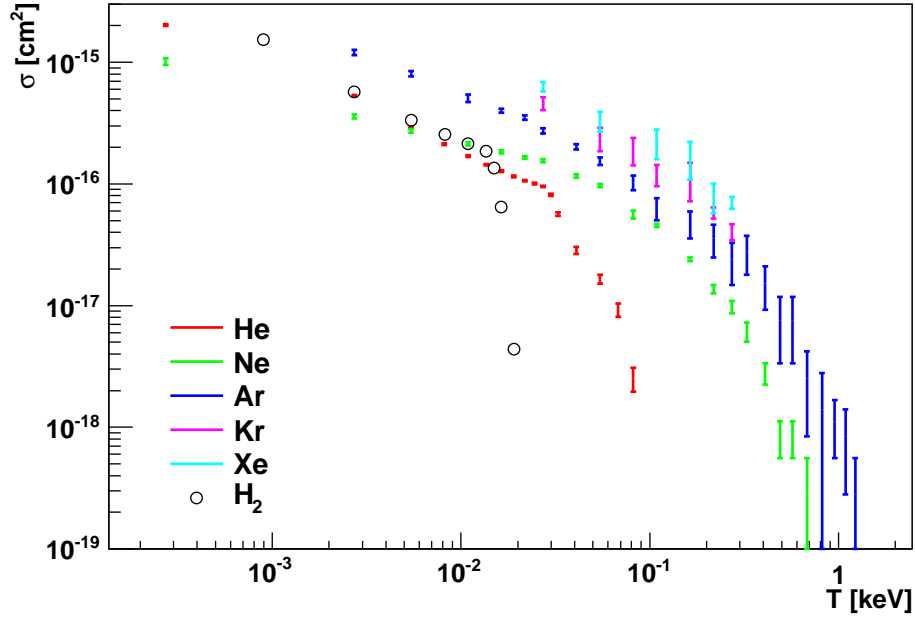
Figure 3.11: Capture cross section for μ^- by noble gasses [99] and hydrogen [100].

3.5 FRICTIONAL COOLING SCHEME FOR A MUON COLLIDER

A muon collider scheme using frictional cooling was investigated in [55]. The cooling channel in the scheme uses the principles of frictional cooling, but the geometry of the cooling cell is far more complicated than the simple geometry described above. As well, the optimized front end of the scheme differs from those described in other muon collider studies [14, 15, 54], which assume that ionization cooling techniques can be optimized to deliver the required emmitance reductions.

Frictional cooling requires that an input beam be at or brought to keV energies. To this end, the front end in [55] is optimized to increase the yield of muons at the lowest energies possible at the end of the pion decay channel. This is achieved by lowering the energy of the initial pion-production proton beam to 2 GeV and extracting the low-energy pions emitted from the target transverse to the proton beam. Transverse extraction has the added benefit of allowing the simultaneous collection of μ^+ and μ^-, so both beams can be prepared from each spill of the proton driver. In the study, this was simulated with a solid target; the feasibility of transverse extraction and a lowered-energy proton beam remains to be studied for use with a liquid jet target, which requires a strong magnetic field along the direction of the target stream.

Ionization cooling schemes, which utilize the high-energy pions emitted in the direction of the proton beam, require the pions (and subsequent muons) be accelerated in the decay channel by a series of fixed-frequency RF accelerating

	x	y	βct	p_x	p_y	p_z
Initial	4.47	8.98	374	42.9	42.9	74.2
Initial (coolable)	9.48	2.68	177	20.2	20.4	37.9
Final$_1$	4.48	4.76	1600	0.16	0.15	1.18
Final$_2$	5.30	3.85	1612	0.16	0.16	1.22

Table 3.2: RMS's of the distributions of position (in cm) and momentum (in MeV/c) for the full input μ^+ beam, the portion of the input beam that is cooled, and for the final cooled beams in the frictional cooling scheme simulated in [55].

3.5.1 Cooling Cell

Even with the efforts described above to lower the input muon energies, the beam still enters the cooling phase of the front end at a mean kinetic energy of 72 MeV, well above T'_{eq}. Table 3.2 lists the dimensions in phase space for the initial muon beam before entering the cooling phase, with the z direction being the initial direction of the beam. At these energies the accelerating power of the restoring electric field is orders of magnitude larger than the stopping power of a moderating gas (figure 3.1). Therefore, in the simplified cooling scheme described above, such a beam would be accelerated up to higher energies, and no phase space reduction would occur.

To bring the energy of the muon beam down below T'_{eq}, the beam is guided through the moderating gas—held in a meters-long cylindrical cell—by a strong magnetic field (5 T) in the same direction as the input beam (figure 3.12). The electric field for the establishment of T_{eq} is oriented perpendicular to the initial direction of the beam, defining the x direction. The force on a muon is

$$\boldsymbol{F} = \boldsymbol{v} \times q\boldsymbol{B} + q\boldsymbol{E} - \rho S \hat{\boldsymbol{v}}, \tag{3.15}$$

where $\hat{\boldsymbol{v}}$ is a unit vector in the direction of the particle's velocity $\boldsymbol{v}$. At high energy, the magnetic term in equation (3.15) is much larger than the electric term, so the muons mostly follow the magnetic field lines, spiraling through the gas, losing energy through the last term in the equation. The strengths of the electric and magnetic field must be tuned such that the $\boldsymbol{E}$ is comparable in magnitude to $\boldsymbol{v} \times \boldsymbol{B}$ in the frictional cooling energy range. For muons this is satisfied by $B/E \sim 1 \text{ T/MV} \cdot \text{m}^{-1}$.

Orienting $\boldsymbol{E}$ perpendicular to $\boldsymbol{B}$ also limits the onset of electric breakdown in a gas, by limiting the kinetic energies of electrons kicked out of the stopping medium atoms [101]. Limiting their kinetic energies decreases the possibility of creating an avalanche of these secondary electrons.

The perpendicularity of the electric and magnetic fields prevents the beam from accelerating away in the z direction, but it causes the muons to drift in the direction orthogonal to both fields, y. To prevent the muons from drifting
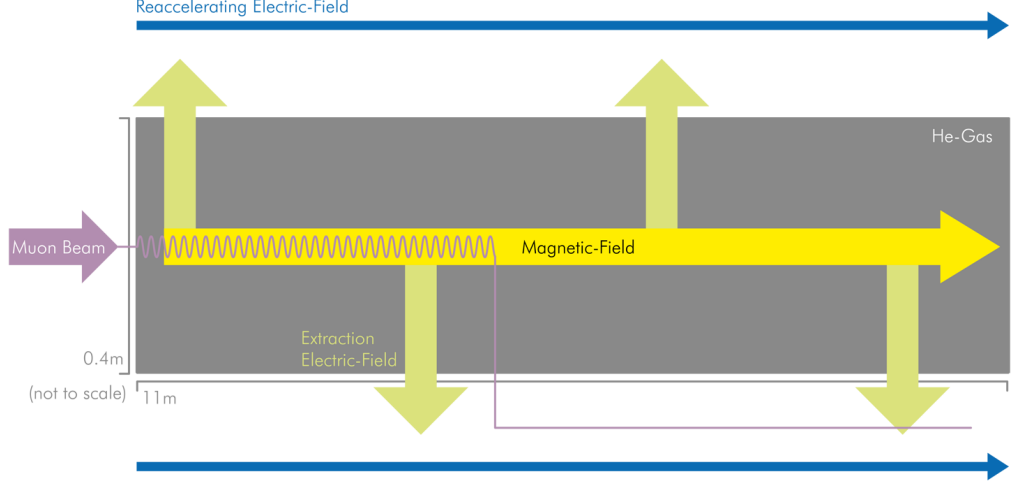
Figure 3.12: Schematic drawing of a frictional cooling cell for a collider front end.

completely out of the gas cell, the direction of the electric field is flipped periodically. In [55], this is achieved by varying the strength of the field in the x direction sinusoidally with respect to z with a period of 60 cm.

The length of the cooling cell in [55] was shortened (to 11 m) by letting the highest-energy muons pass through it, be reflected back into it, and have a second pass at slowing down to the frictional cooling energy region. To reflect the beam back into the cooling cell, a time-dependent electric field in the negative z direction is used at $z > 11$ m. The field strength is constant for a time t_0 and then linearly drops to zero at time t_1. These times were optimized to $t_0 = 100$ ns and $t_1 = 440$ ns to increase the yield of coolable muons entering the cooling cell on the second, reflected pass. This field rotates the phase-space volume of the beam, stretching it out in z, but decreasing the mean energy from approximately 50 MeV to approximately 10 MeV, and the energy spread from 10s of MeV to approximately 5 MeV.

After the muons slow down to the frictional cooling region, when $\boldsymbol{E}$ and $\boldsymbol{v} \times \boldsymbol{B}$ are of comparable magnitude, they begin to exit the cooling cell in the transverse direction. They very quickly reach T_{eq}, and their motion is confined to the $\boldsymbol{E}$-($\boldsymbol{E} \times \boldsymbol{B}$) plane (the x-y plane). The angle from $\boldsymbol{E}$ at which the muon travels now is given by [102]

$$\tan \theta = -\frac{\eta B}{\rho S(T_{\mathrm{eq}})/v_{\mathrm{eq}}} = -\frac{B v_{\mathrm{eq}}}{E}, \tag{3.16}$$

since $\rho S(T_{\mathrm{eq}}) = \eta(T_{\mathrm{eq}})E$. Since the field strengths E and B are chosen, as described above such that $E/B \sim v_{\mathrm{eq}}$, $|\theta| \sim 45°$.

At energies $T \ll m_{\mu}c^2$, the mean distance traveled by a muon before decaying is

$$v\tau_{\mu} \approx T^{\frac{1}{2}} \cdot 10 \text{ cm/eV}^{\frac{1}{2}}. \tag{3.17}$$
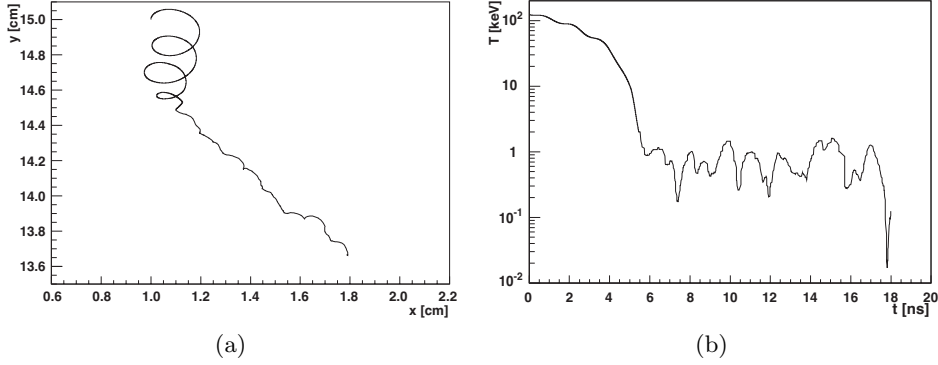
(a)   (b)

Figure 3.13: Portion of a trajectory of a sample μ^+ in a frictional cooling cell directly before and after reaching T_{eq} and begining to exit the gas cell.

Since the cooled muons, traveling at $T_{eq} = \mathcal{O}(keV)$ exit the cooling cell in the transverse direction, equation (3.17) imposes a limit on the diameter of the cooling cell of 10s of cm. The input beam of table 3.2 has a transverse spot size of 40 cm diameter; this is therefore chosen as the transverse size of the cooling cell.

FULL COOLING SCHEME

Incorporating the above considerations, the full scheme of the cooling cell in [55] consists of an 11-m-long helium gas cell (with a gas density of 1.25×10^{-4} g/cm^3), with the length oriented along the beam (z) direction; a 5-T magnetic field in the z direction; an electric field in the x direction, with its strength varied sinusoidally with z with a period of 60 cm and an amplitude of 5 MV/m; and a phase-rotating time-dependent electric field in the $-z$ direction for $z > 11$ m with a maximum strength of 5 MV/m.

Muons with kinetic energies less than approximately 50 MeV are stopped in the gas cell, and exit it in the transverse direction. Figure 3.13 shows an 18-ns window of the trajectory of a μ^+ in the gas cell around the time at which it decelerates to T_{eq}. The spiralling due to the magnetic field is visible, as is the decrease of the radius of motion with the decreasing energy of the muon. Furthermore, the swim in the y direction is apparent. The energy losses in the region around and above T_{eq} are very large, and the muon very rapidly decelerates to T_{eq}. Once at this energy it exits the gas cell at the characteristic lorenz angle, $|\theta| \sim 45°$. Nuclear scattering is visible in both the view of the trajectory in the x-y plane (as kinks in the motion) and most importantly in the T-t plane, where the effect of large angle scattering can be seen: the μ^+ is scattered into a direction opposed to $\boldsymbol{E}$ and brought nearly to rest as its direction is changed and it is reaccelerated to T_{eq}.

Due to the periodic flipping of the direction of the electric field, muons exit the gas cell in either of two directions $\pm R(\theta)\hat{\boldsymbol{x}}$, where $R(\theta)$ is a rotation about the z axis by the angle given by equation (3.16).

Outside the gas cell is a weakly reaccelerating electric field (10 kV/m). After exiting the gas cell through thin windows, the muons are reaccelerated in the z

	ϵ_{T} $[(\pi\mathrm{m})^2]$	ϵ_{L} $[\pi\mathrm{m}]$	ϵ_6 $[(\pi\mathrm{m})^3]$
Initial	9.51×10^{-6}	2.0×10^{-1}	1.92×10^{-6}
Final$_1$	4.56×10^{-10}	5.7×10^{-2}	2.61×10^{-11}
Final$_2$	4.71×10^{-10}	5.9×10^{-2}	2.79×10^{-11}

Table 3.3: Transverse, longitudinal, and 6D emittances of a μ^+ beam before and after frictional cooling as in the scheme described in [55].

direction towards the end of the gas cell. Since muons exit the gas cell all along its length, the reacceleration field introduces an energy spread of approximately 30 keV. The position and momentum spreads of the two beams exiting the $z = 11$ m plane of the gas cell region are listed in table 3.2.

The RMS time spread of the beam at the $z = 11$ m plane is 1 µs. Beyond this plane a time-dependent electric field rapidly reaccelerates the muons up to 150 MeV. The time dependence of the field is given by

$$E = E_0 + A(t - t_0) + B(t - t_0)^2, \qquad (3.18)$$

where $E_0 = 14$ kV/m, $A = 185$ kV/m $\cdot$ µs, $B = 6.78$ MV/m $\cdot$ µs^2, and t_0 is a timing offset accounting for the time for the first muons to reach the end plane of the cooling cell relative to the time of impact of the proton beam on the pion production target; t_0 is approximately 1 µs. The mean time difference between entering and exiting the cooling channel for a cooled muon is approximately 500 ns, with the maximum time (achieved by the fastest muons), approximately 1 µs.

The final RMS momentum spread of the beam is 5 MeV/c at a mean momentum of 150 MeV/c, with an RMS time spread of 3 ns. The initial and final emittances, calculated from the six RMS spreads in table 3.2, with no correlations accounted for, according to

$$\epsilon_{\mathrm{T}} = \frac{\sigma_x\sigma_y\sigma_{p_x}\sigma_{p_y}}{(\pi m_\mu c)^2}, \quad \epsilon_{\mathrm{L}} = \frac{\sigma_{\beta ct}\sigma_{p_z}}{\pi m_\mu c}, \quad \text{and} \quad \epsilon_6 = \epsilon_{\mathrm{T}}\epsilon_{\mathrm{L}}, \qquad (3.19)$$

are listed in table 3.3 for a μ^+ frictional cooling scheme using helium gas at 0.125 mg/cm^3. The initial emittance is calculated for the portion of the initial beam that is ultimately cooled. The final emittance achieved is an order of magnitude smaller than that required for a muon collider (see section 2.4.3). This emittance is achieved with a muon yield of 2.1×10^{-3} μ^+ per proton incident on the pion production target.

The luminosity of a collider is inversely dependent on the emittance and directly dependent on the population (N) of the colliding beams,

$$L \propto \frac{N^2}{\epsilon_{\mathrm{T}}}. \qquad (3.20)$$

By decreasing the emittance to an order of magnitude lower than required, frictional cooling would allow for beams with lower populations. This relaxes the requirements on the proton driver and reduces the total background per bunch crossing in the interaction point detectors.

CoolSim

Though mentioned as a concern, the effects of charge exchange processes were not accounted for in the calculations of [55]. To study the effects of charge exchange processes on a muon collider frictional cooling scheme as well as for the easy simulation of other frictional cooling schemes (for example [103]), we developed a new low-energy μ^+ and proton Monte-Carlo tracking program, CoolSim.

The basic tracking of particles is handled by the Geant4 [104] software from CERN. For the purposes of tracking low-energy massive particles, only electromagnetic interactions are accounted for. This includes the processes of most importance to frictional cooling: energy losses due to electronic interactions with matter; nuclear scattering and its accompanying energy losses; acceleration due to electric and magnetic fields; and decay of unstable particles. We also used Geant4's built-in handling of physics processes capable of tracking photons and electrons in matter, allowing CoolSim to accurately simulate the deposition of energy in a silicon drift detector by x-rays and protons.

We wrote a new process for the handling of the effects of charge exchange processes including effective charges and beam neutralization. The process was programmed in accordance with Geant4 standards, for versatile implementation.

CoolSim also contains components for the easy and quick building of simulation geometries common to cooling. Additionally it contains components for the input of initial particle distributions and electric and magnetic field maps, and the output of particle information during the tracking process.

4.1 LOW-ENERGY PHYSICS PROCESSES IN GEANT4

Geant4 implements physics processes as belonging to three overlapping categories: processes that occur when a particle is at rest; processes that occur continuously along a particle's trajectory; and processes that occur at discrete locations along a particle's trajectory.

A simple example of a process that belongs to the overlap of the first and last categories is that of particle decay, because a particle can decay while at rest and while moving. Nuclear scattering is an example of a process that belongs to the overlap of the second and third categories: the changes of direction due to scattering are applied at discrete locations; the changes in energy are applied as continuous-energy-loss approximations along a trajectory.

When a particle is at rest, Geant4 requests from all competing at-rest processes a lifetime for the process to occur; it then selects the process with the

shortest lifetime and invokes it. For a moving particle, Geant4 requests from each discretely occurring process an interaction length for the process to occur. These interaction lengths incorporate the distance the particle has already traveled without the process occurring, which is reset to zero after the process has occurred, and is randomly sampled from the mean free path for the interaction to occur given the particular particle being tracked and its current state. The process with the shortest interaction length is selected; the particle is transported by the interaction length to a new position, and the process is invoked. This distance traveled is then used to calculate changes to the particle according to processes that occur along its trajectory. This constitutes one step in the trajectory of the particle.

All three categories of processes may produce new, secondary particles. After the primary particle is tracked to a terminus (for example, it decays, it stops, or it exits the boundaries of the simulation "world"), secondary particles are tracked in the same way as the primary particle, each to its terminus. Then any tertiary particles created by the secondary particles are tracked, and so on. A single event ends when all particles have been tracked to their termini.

4.1.1 *Multiple Scattering*

To save calculation time, at high kinetic energies, individual nuclear scattering events are not calculated. Instead the model of multiple scattering in [105] as implemented according to [106] is used to calculate the collective deflection of numerous scattering events. This process also calculates the true distance traveled by a particle, which is longer than its displacement at the end of the step due to the individual scattering events that are not discretely simulated but are summarized by the model. This true distance is used for the interaction length evaluation of the other processes. At low kinetic energies, the process also implements individual scattering events according to a coulomb scattering model. In CoolSim, for muons and electrons of either charge, this physics process is handled by the Geant4 class G4MultipleScattering in default mode. For protons of either charge, it is handled by G4hMultipleScattering in default mode.

The accompanying energy loss is incorporated as a continuous-loss approximation with straggling given by the nuclear stopping power data for the tracked particle. This is handled by the class that handles electronic stopping energy losses.

4.1.2 *Electronic Stopping*

Low-energy electronic stopping in Geant4 incorporates the energy losses of all interactions with the stopping medium electrons, including those of charge exchange processes. However, it does not alter the charge of a μ^+ or p, neither discretely nor via an effective charge. Energy loss is calculated along the particle's trajectory using the continuous-loss approximation with energy straggling according to the electronic stopping power data for the tracked particle, and includes the accompanying nuclear stopping energy losses. The model and data

44

Helium	He	Water	H_2O
Neon	Ne	Carbon	C
Argon	Ar	Methane	CH_4
Krypton	Kr	Ethylene	C_2H_4
Xenon	Xe	Ethane	C_2H_6
Hydrogen	H_2	Butane	C_4H_{10}
Nitrogen	N_2	Carbon Monoxide	CO
Oxygen	O_2	Carbon Dioxide	CO_2

Table 4.1: Materials supported by CSEffectiveCharge in CoolSim.

used to calculate both energy losses is that given in [85], including the effects of the Barkas model for the differences between the stopping powers on positive and negative particles. Though applied along the tracking step, this process can create discrete new particles in the form of δ-rays—high-energy secondary electrons. In CoolSim, for electrons, this process is handled by G4LowEnergyIonisation; for positrons, it is handled by G4eIonisation. For muons and protons of either charge, it is handled by G4hLowEnergyIonisation.

4.1.3 *Transportation*

Perhaps the most fundamental process in Geant4 is its handling of the transportation of particles in the simulation world. This is handled by the G4Transportation class via a Runge-Kutta stepping process. This class accesses information about the electric and magnetic fields set by the user; in CoolSim the information about these fields are stored in classes described in section 4.3.1. This process also keeps track of when particles exit a volume and enter the next one, and therefore reports back an "interaction length," which here corresponds to a maximum distance traveled before changing simulation volumes. Volumes are described in section 4.3.

4.2 EFFECTIVE CHARGE & BEAM NEUTRALIZATION

The energy losses of charge exchange interactions are simulated by the processes described above. To incorporate the effects of charge state cycles on the trajectories of μ^+ and protons in a gas in the presence of an electric field, a new process was added to the Geant4 framework in CoolSim. This process, CSEffectiveCharge, also handles the neutralization of a positively charged beam upon exiting a material and entering a vacuum.

The effective charge is calculated according to equation (3.11) at the end of each tracking step. The charge of the tracked particle is then replaced with the updated value, and this value is used by the transportation process to calculate the motion of the particle in the present electric and magnetic fields. To reduce the CPU time required per step, only two charge states—positive and neutral—are included in the effective charge calculation. This also allows for a consistent

model across many materials, since the negative-state cross section are unkown for many materials. The negative charge state fraction contributes to the effective charge at the percent level or less, and only for select energy ranges (see section 3.3 for more details). Table 4.1 lists the materials that are currently supported by CSEffectiveCharge. The cross sections for electron capture by p and electron loss by H are taken from [94] with the equivalent cross sections for μ^+ and Mu provided from these by velocity scaling.

CoolSim will also assign an integer charge state to a proton or μ^+ upon exiting a volume in which an effective charge was simulated and entering vacuum. It assigns the new charge probabilitistcally according to the charge state fraction f^+ calculated for the material of the exited volume and the projectile's energy upon exit.

When a particle crosses a boundary between two volumes of different materials, in both of which effective charge is simulated, CoolSim assigns the particle a charge at the end of the step according to the effective charge of the material of the volume being entered and the energy at which the particle enters it.

The conformity of the CoolSim simulation of effective charge to the analytical calculations of chapter three is discussed in section 6.3.

4.3 GEOMETRY

We built into CoolSim several standard components of cooling schemes, so that a complete simulation can be built up from macro files that conform to the Geant4 standards. These components are based on the basic geometric volumes of Geant4, with additions for handling arbitrary electric and magnetic fields.

4.3.1 *Electric & Magnetic Fields*

To replace the cumbersome implementation of electric and magnetic fields in Geant4—which must be hard-coded into each simulation—we harnessed the function-handling capabilities of the CERN ROOT calculation package [107]. This allows any number of electric and magnetic fields to be specified for a volume or collection of volumes by any functions of space and time.

Additionally, CoolSim can read a map of electric or magnetic field values from a file, and interpolate between map points to provide fields for volumes. This function was used in the simulations of the experiment, described in chapter six.

4.3.2 *Cooling Cell*

The most essential building block of simulations of a frictional cooling scheme is the cooling cell itself. This consists of a cylindrical container (with imaginary walls) containing a gas at a specified density (or pressure and temperature). The ideal simple gas cell has parallel, uniform, and constant electric and magnetic fields aligned down the central axis of the cylinder. The orientation of the fields can be changed, as can their uniformity. For a realistic cell, such as described

in chapter five, the field equations can be replaced with field maps.

4.3.3 *More Complicated Components*

We wrote the CoolSim package so as to allow for the easy expansion of the library of often-used components. Extensive use of common accelerator magnets was made in [103], which simulated low-energy μ^+ beam production with a frictional cooling scheme. For these and similar studies, standalone quadrupole and dipole volumes were created; as well, more complicated composite components, such as FODO cells and wedge-shaped absorbers, were implemented.

4.4 OUTPUT

To facilitate easy analysis of simulation results, the data storage power of ROOT was harnessed. All physical information about every tracked particle, as well as unphysical information (such as its tracking status or the name of the volume it is traveling in), can be stored in ROOT's TTree storage container and saved to a ROOT file.

CHAPTER 5

FCD Experiment

Motivated by the promising results of the frictional cooling simulations of [88] and [55], the Frictional Cooling Demonstration (FCD) experiment was established to verify the working principles behind the simulations. The FCD experiment is at the Max-Planck-Institut für Physik in Munich, Germany. The experiment consists of a gas cell mounted inside an accelerating grid that provides the restoring electric field (figure 5.1), with a particle source and detector on opposite ends of the gas cell. The detector will measure the energies of protons that are accelerated from rest at the opposite end of the gas cell to an energy dependent on the source–detector separation, the moderator material and density, and the electric field strength. We can compare these measurements to Monte-Carlo simulations of the experiment (chapter six) and achieve a better understanding of the simulated processes, which are the same as those involved in larger simulations of frictional cooling schemes.

5.1 EXPERIMENT COMPONENTS

The gas cell is a cylinder made of polyether ether ketone (commercially known as PEEK) with an outer radius of 31 mm and an inner radius of 27 mm. One end of the cell (the left side of figure 5.1) is sealed but for a small hole on the central axis of the cylinder (the z axis), through which the proton source is mounted, creating a gas-tight seal. The opposite end of the cell is completely open, and is sealed by a metal flange containing a central bore for holding the detector and houses input and output gas feedthroughs.

The proton source (figure 5.2) consists of an open alpha source covered with a Mylar foil. The alpha particles free protons from the Mylar (see section 5.1.2). The alpha source is embedded in the top of a lollipop made of PEEK. A cap, also constructed from PEEK, fastens to the lollipop head and holds the Mylar foil in place. Foils of various thicknesses can be swapped into the construction easily and quickly.

The lollipop stick screws at one end into the head and at the other end into a cylindrical platform 25 mm in diameter with a threaded rod extending out of the side opposite to that which the lollipop is attached. The platform with the attached lollipop fastens to the gas cell through the small hole mentioned above. An o-ring sandwiched between the platform and the gas cell wall (shown in cross section as two small black circles in figure 5.1) provides a gas-tight seal when the a nut is fastened to the rod, fastening the platform in place. Three copies of the
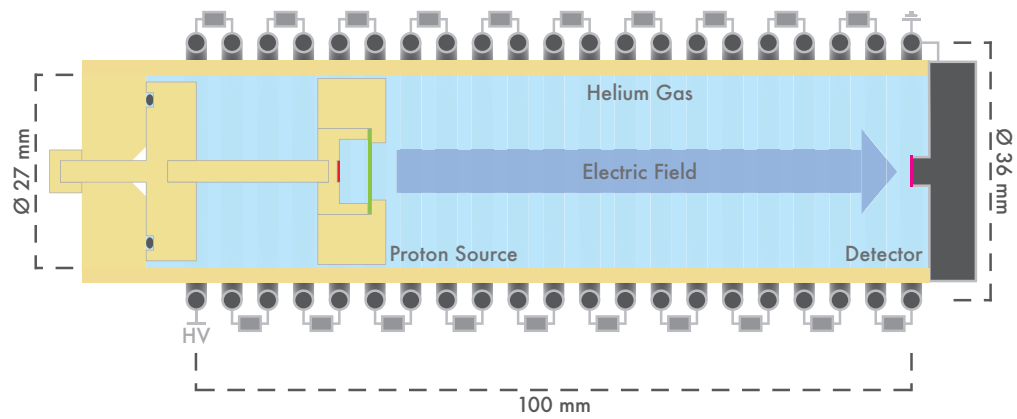
Figure 5.1: Scale diagram of the FCD cooling cell.

Figure 5.2: Photo of the proton source assembled (left) and disassembled (right). The gold-colored disc is the americium alpha source. The cylindrical cap holds the mylar foil.

source holder were manufactured with identical shapes but different materials: one each of PEEK, stainless steel, and copper.

Different lengths of the stick of the source lollipop were manufactured at increments of 5 mm. By swapping the stick in the construction, the z position of the proton source can be changed, allowing for measurements at different source–detector separation lengths.

The particle detector (figure 5.3), a silicon drift detector (SDD), is mounted to the gas feedthrough flange (figure 5.4) at the end of the cell opposite the proton source. It is mounted via a PEEK holder that is also a feedthrough for all electronic connections to the SDD. This construction allows for a quick exchange of the SDD and provides a gas-tight seal for the cell.

The entire construction thus far described is placed inside the accelerating grid, which is constructed from twenty-one metal rings, 3 mm thick, spaced 5 mm apart, connected in series by 64-MΩ resistors. The rings enclose a cylindrical space 33 mm in diameter and 100 mm long from the center of the first ring to the center of the last ring. The first ring—numbering from the proton-source side to the detector side—is connected to a power supply capable of providing voltages up to 100 kV; the last ring is grounded to the gas feedthrough flange.
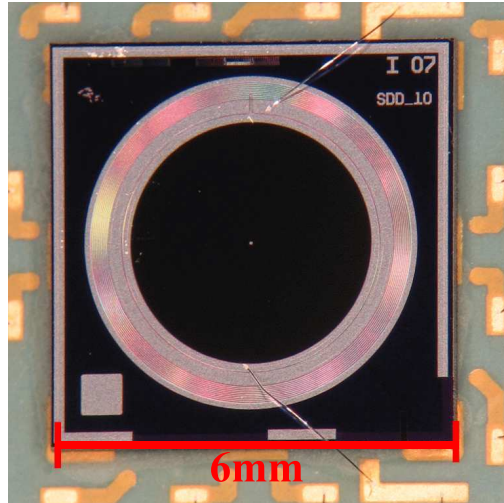
50

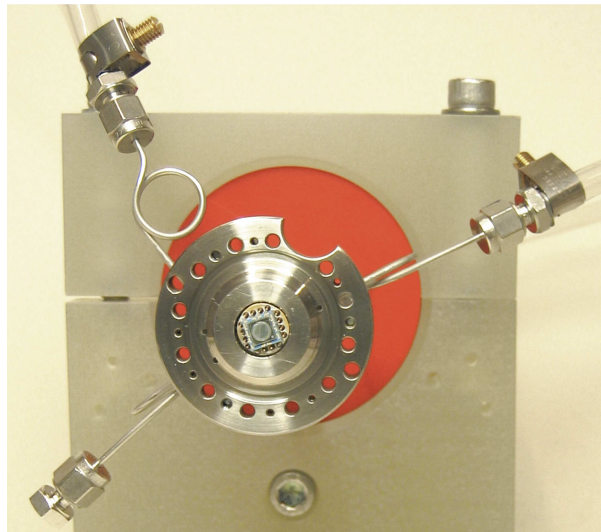Figure 5.3: Photo of the SDD. The inner black circle is the back surface of the active region.

Figure 5.4: Photo of the SDD mounted into the gas feedthrough flange.

The central axis of the grid defines the z axis for all discussions of position in this chapter, with $z = 0$ mm at the plane through the center of the high-voltage (HV) ring and $z = 100$ mm at the plane through the center of the grounded ring. The grid creates nearly uniform electric fields along the z axis with strengths up to 1 MV/m.

The accelerating grid with the gas cell, source, detector, and gas and electronics feedthroughs is placed inside a vacuum tank, capable of being evacuated down to pressures as low as 10^{-7} mbar. Figure 5.5 shows the placement of the construction described above in the vacuum tank.
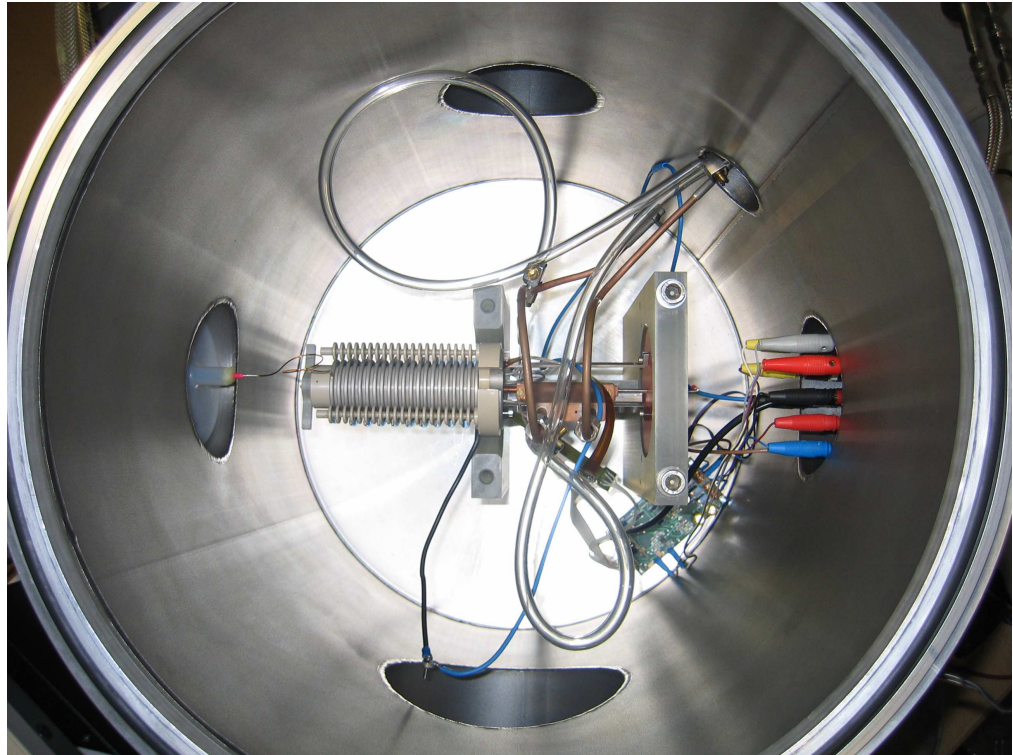
Figure 5.5: Photo of the FCD cooling cell: visible are the gas cell (center) with the source on the left-hand side and detector on the right-hand side; the connection to HV (left); electronics feedthroughs (right) leading to the electronics (bottom right); and the gas feedthroughs (top right).

5.1.1 Electric Field

A map of the electric field created by the accelerating grid is needed for the full simulation of the FCD experiment as well as for characterizing the detector's response to protons. We used a successive overrelaxation algorithm to calculate the electric potential in the z–r plane (figure 5.6). This calculation revealed that, the potential is at its maximum not at $z = 0$ mm, but instead at $z = 9$ mm. Therefore the surface of the proton source must be placed at $z > 9$ mm. The electric field is strongest and also nearest to uniform at $z \geq 20$ mm. In the simulation of the FCD cell and in the measurement of proton spectra in the actual experiment, the source surface is therefore placed at $z \geq 20$ mm.

5.1.2 Proton Source

The proton source contains a 74-kBq ^{241}Am alpha source covered by a thin Mylar foil. The americium emits alpha particles with energies approximately 5 MeV (table 5.1). As they pass through the Mylar, they break carbon–hydrogen bonds, freeing hydrogen nuclei from the Mylar molecule (figure 5.7). When these bonds are broken near the outer surface of the foil, the electric field can accelerate the
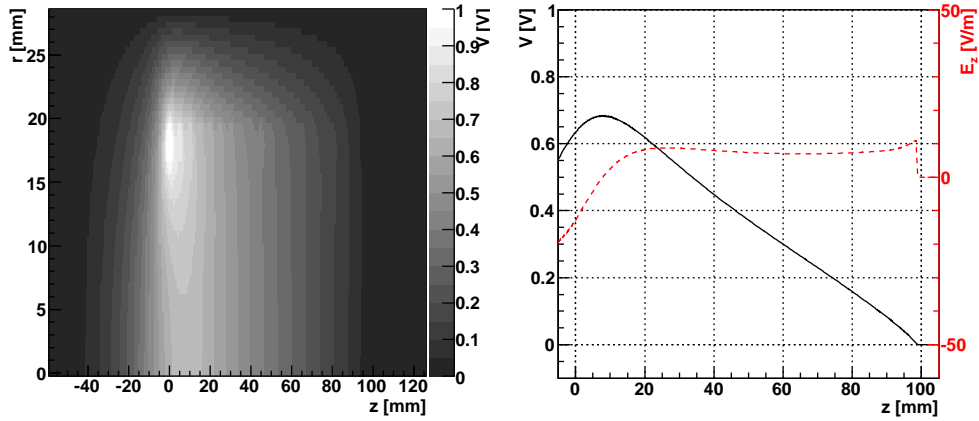
Figure 5.6: Map of the potential, for a voltage of 1 V applied to the first ring, in the z–r plane (left) and as a function of r on the z axis (right) created by the accelerating grid (with plastic source holder). The longitudinal electric field strength (dashed; right-hand axis) as a function of r on the z axis is also shown.
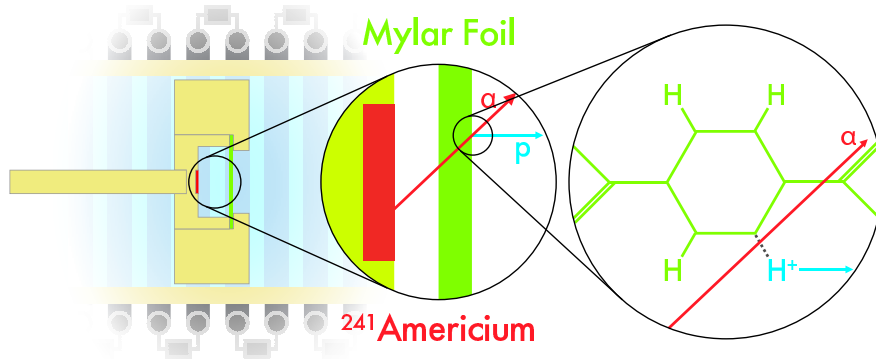

Figure 5.7: Schematic of the proton production mechanism

Energy	5.388	5.422	5.485	MeV
Branching Ratio	1.0	13.0	84.5	%

Table 5.1: Energies and branching ratios for alpha particles emitted by ^{241}Am with branching ratio greater than 0.4%

resultant protons out of the foil before they are recaptured.

The number of bonds an α breaks per unit distance is

$$n_p(T) = \sigma_{ion}(T) \cdot \rho_H, \qquad (5.1)$$

where σ_{ion} is the cross section for ionization of molecular hydrogen by He^{2+} and ρ_H is the concentration of hydrogen in Mylar, 34.35 nm^{-3}. The measured cross
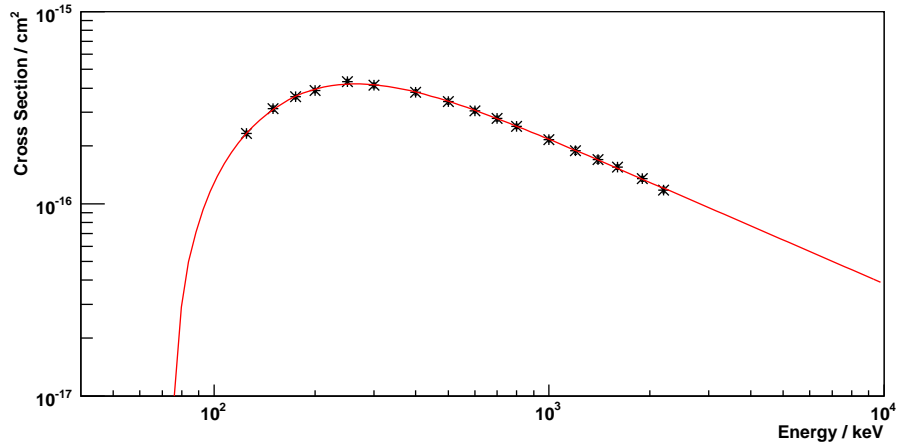
Figure 5.8: Measured cross section for the ionization of molecular hydrogen by He^{2+} [108] (points) and a fit adapted from [95] (line).

section for ionization of molecular hydrogen,

$$\text{He}^{2+} + \text{H}_2 \rightarrow \text{He}^n + \text{p}, \tag{5.2}$$

where He^n is any charge state of helium, was reported in [108]. To interpolate and extract to low energies the cross section (figure 5.8), we fit to the data a semi-empirical formula for the cross section of hydrogen on helium found in [95] in the reformulation of [94] adapted for He^{2+} projectiles

$$\sigma = \sigma_0 \cdot a_1 \left(\frac{T'}{E_R} \right)^{a_2} \bigg/ \left(1 + \left(\frac{T'}{a_3} \right)^{a_2 + a_4} + \left(\frac{T'}{a_5} \right)^{a_2 + a_6} \right),$$

where $T' = T - I$ is the kinetic energy of the α above the threshold energy I for ionization to occur; E_R is the Rydberg energy scaled up by m_He/m_e; and σ_0 is a scaling factor equal to 10^{-16} cm^2. The a_i are fit parameters empirically motivated by the behavior of the cross section at small and large energies as described in [95].

The americium is in the form of a disc 2.5 mm in diameter, which is embedded in a PEEK lollipop-shaped holder. It is completely open on its exposed side. A cap fits over the lollipop to hold the Mylar foil in place at a distance of 2.45 mm from the source. The cap has a circular opening 3.5 mm in diameter centered over the source.

We simulated this proton source in Geant4, to predict the spatial distribution of the breaking of C–H bonds at the surface of the foil furthest from the americium (that is, the side exposed to the gas cell). The number of bonds broken per unit volume is

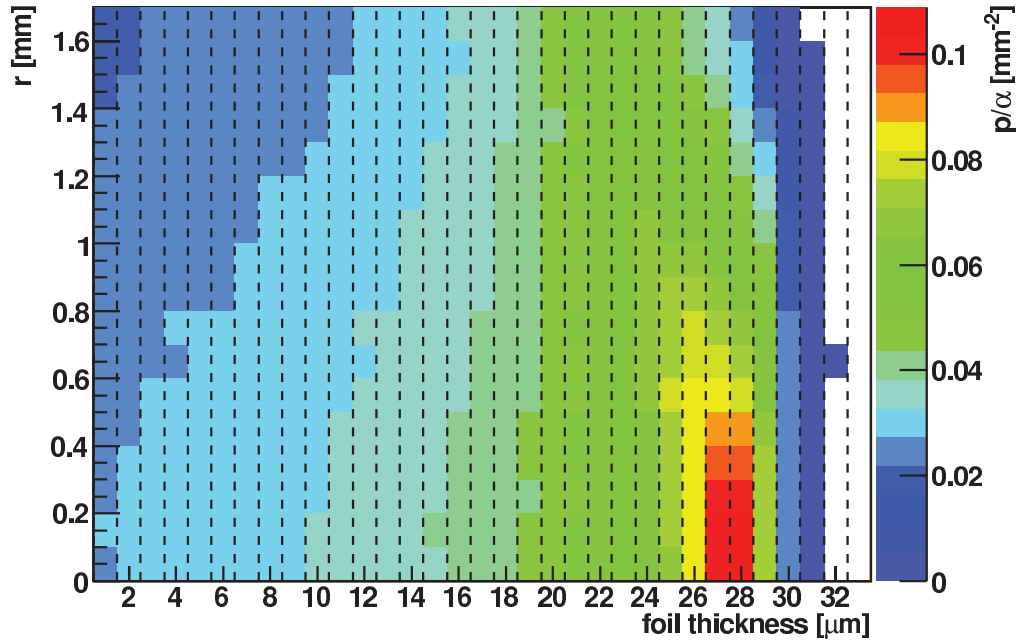$$N_\text{p}(r, z) = \int \sigma_\text{ion}(T) P(T; r, z) \text{d}T, \tag{5.3}$$

54

Figure 5.9: Proton production density p/α in the last 1 nm of foil as a function of radial position and Mylar foil thickness.

where $P(T; r, z)$ is the probability density for a single α to have kinetic energy T at position (r, z) given the spectrum of americium and the geometry of the source; r and z are as defined for the gas cell, since the source has the same cylindrical symmetry as the cell (figure 5.1). To calculate this we track α's that pass through the Mylar foil. Using their locations and energies, we calculate the number of C–H bonds broken. The number of protons is calculated as the number of bonds broken in the last 1 nm (in z) of Mylar before the outer surface of the foil. This distance is the approximate size of the Mylar monomer, and is taken as an ansatz for the distance a proton can travel before being recaptured.

Figure 5.9 shows the r and z dependence of the density of protons produced per incident α in the last 1 nm of foil before the surface. The results are presented for thickness of foil from 1 µm to 33 µm in 1-µm increments, since this is the precision to which such foils are manufactured. The range of ^{241}Am α's in Mylar is less than 33 µm, which conforms to the range listed in [85].

We also calculated the total proton production (again in the last 1 nm) as a function of thickness of the Mylar foil (figure 5.10). The shape of the rate–thickness relationship is similar to that of the Bragg peak for α's in Mylar; however, it is broadened by the distribution of the incidence angles of the α's and the shape of the ionization cross section. The rate is maximum in the region of 25 µm and is zero above 30 µm, since the α's are stopped in the foil before reaching the surface. Around the rate-maximizing thickness, the proton production is spatially uniform, and at larger thicknesses, the protons are produced mainly at the center of the foil surface. Though at the larger thicknesses the total rate is lower, when detector acceptance is taken into account (see section 6.2),
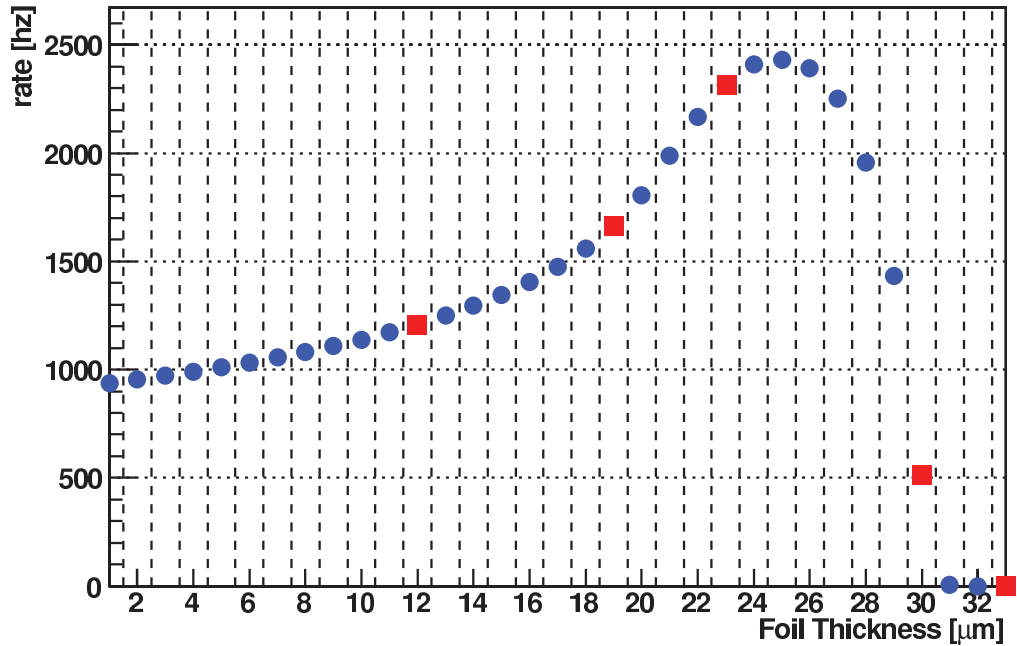
Figure 5.10: Proton production rate in the last 1 nm of foil as a function of Mylar foil thickness for an ^{241}Am source activity of 74 kBq. The highlighted points indicate the five thicknesses of foil available to the FCD experiment.
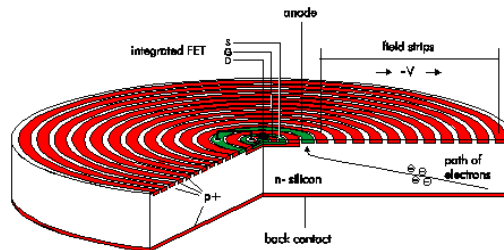

Figure 5.11: Schematic of the SDD from [109], showing the electrode structure used to deplete the detector bulk and setup the charge-collection field, and the FET.

the centralized proton production may be beneficial. The square-shaped markers in figure 5.10 indicate the five thicknesses available for the experiment: 12, 19, 23, 30, and 33 μm. By sandwiching foils together, we are also able to test thicknesses of 24 and 31 μm.

5.1.3 *Silicon Drift Detector*

The SDD, designed by the MPP's Semiconductor Laboratory and constructed by PNSensor [110] measures particle energies in the range 100s eV to approximately 150 keV. The detector is constructed on an n-type silicon wafer 450 μm thick. The exposed (back) surface of the detector is covered uniformly with a
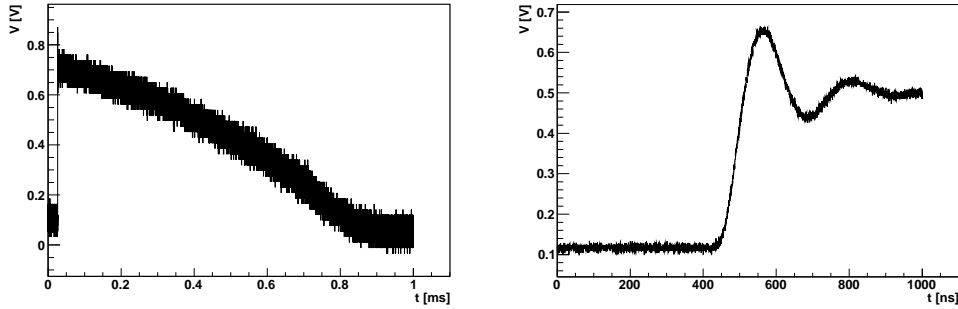
Figure 5.12: Signal from a SDD after initial amplification. The plot on the right is zoomed in on the rising edge of the full signal shown on the left.

30-nm-thick aluminum electrode. The opposite surface is implanted with concentric rings of p-type silicon (figure 5.11). A negative potential (on the order of -100 V) on the aluminum depletes the silicon. The p-type rings are placed at voltages that produce a well-shaped potential inside the silicon. Ionizing particles produce a number of electron-hole pairs in the silicon in proportion to the amount of energy they deposit along their trajectory; the electrons then drift to the center of the p-doped surface of the detector, where a field-effect transistor (FET) produces a signal.

The voltages for depletion of the silicon and setting up of the potential well are regulated by electronics manufactured by PNSensor [110]. The detector outputs a saw-tooth-shaped voltage pulse that after initial amplification by these electronics has a rise time of 30 to 40 ns (figure 5.12) and an amplitude

$$V_{\mathrm{det}} \approx (1.2 \ \mathrm{mV/keV}) \cdot T_{\mathrm{dep}}, \tag{5.4}$$

where T_{dep} is the energy the particle deposits in the active layers of the detector.

5.2 DETECTOR READOUT

A shaping amplifier with a shaping time of 0.25 μs converts the SDD's quickly rising signal to a fin-shaped pulse 3 to 4 μs wide (figure 5.13). The shaper preserves the linearity of the signal amplitude's dependence on T_{dep}. The shaped signal is split in two: one part is used for triggering; the other is digitized and saved for offline analysis.

5.2.1 *Recorded Signal*

A 12-bit analog-to-digital converter (ADC) from National Instruments [111], interfaced with a computer via a program we wrote in the LabView [112] language specifically for the FCD detectors, digitizes the signal with a sampling rate of 10 MHz. Before entering the ADC, the signal is delayed 4.75 μs with respect to the trigger signal, so that the baseline voltage before the signal is recorded as well. When triggered, the ADC records an event for 10 μs (100 samples).
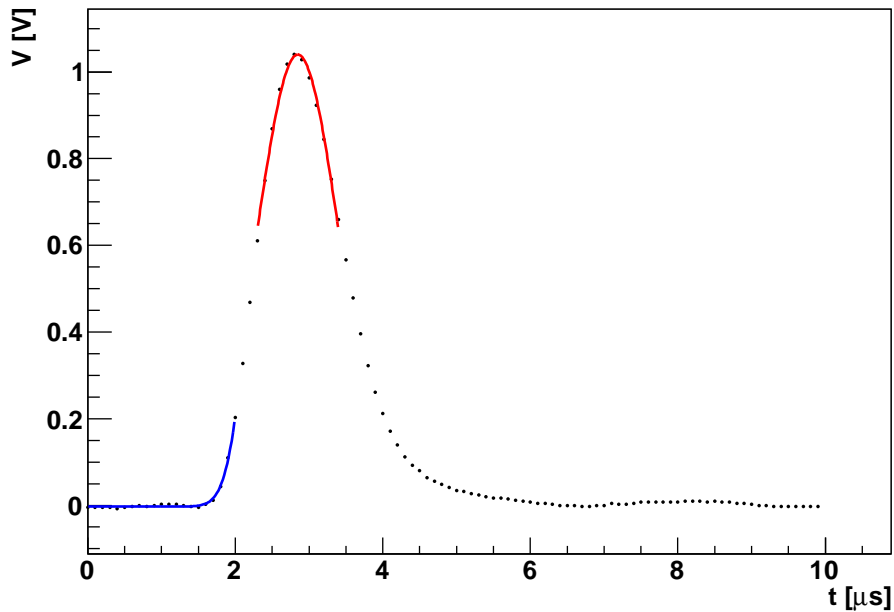
Figure 5.13: Shaped and digitized signal from the SDD with pedestal and peak fits.

LabView also records the start time for each event relative to the start of the run.

5.2.2 *Trigger*

A window discriminator, consisting of two trailing-edge constant fraction discriminators (CFD), one setting a low threshold, the other a high threshold, produces the trigger signal for the ADC to begin sampling. The low-threshold CFD filters out low-amplitude voltage fluctuations—thermal noise from the detector and electronic noise picked up by cabling or shaping components. Since the ADC has a maximum trigger rate of 30 Hz, when needed, the high-threshold CFD is used to filter out unimportant signals that have large amplitudes, namely those from α particles.

5.2.3 *Run Parameters*

The LabView program that records the digitized event signals, also records the parameters of the run. These are input by hand into the program for each run. The parameters are the amplification level of the signal, the shaping time, and the delay of the signal with respect to the trigger; the sampling time of the ADC and number of samples per event; the type of particle source, its distance from the detector, and the thickness of Mylar foil placed over the source; the identification number of the detector and the voltages applied to it
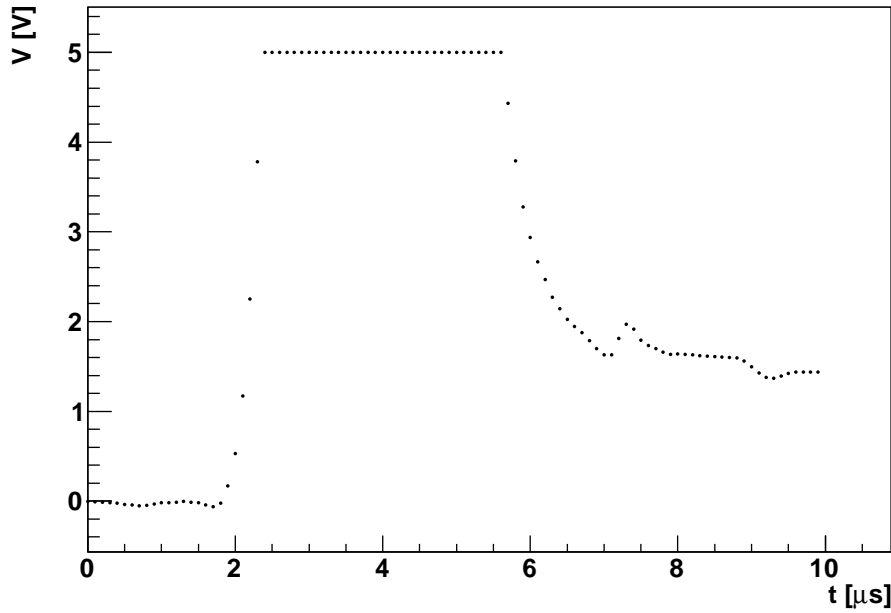
Figure 5.14: Saturated signal from the SDD.

for its operation; the current supplied to the detector's Peltier cooling element and the detector's temperature; the pressure of the helium gas in the cooling cell; and the voltage applied to the accelerating grid.

5.2.4 Saturated Signal

A particle that deposits too much energy ($T_{dep} \gtrsim 150$ keV) in the detector produces a charge-saturated signal (figure 5.14). The signal is distorted and the energy of the particle cannot be reconstructed. These signals can be filtered out by the window discriminator; however, the saturation often produces secondary signal peaks in the trailing edge of the original signal. Such a peak is visible in the tail of the main peak in figure 5.14, beginning around $t = 7.5$ µs. These peaks are large enough to pass the low-threshold CFD but small enough for the high-threshold CFD to not veto them. To prevent these signals from swamping the ADC, a gate generator can produce a veto signal from the high-threshold CFD's trigger pulse. The length of the gate can be set within a large range of times from less than 100 ns to greater than 11 s.

5.3 OFFLINE ANALYSIS

The analysis of the recorded data proceeds in stages (figure 5.15): the data and run information from LabView are read in from ascii files and converted into ROOT ntuples; a fit method is used to describe the signal in each event and produce an "event value"; information about the fit and the signal's samples
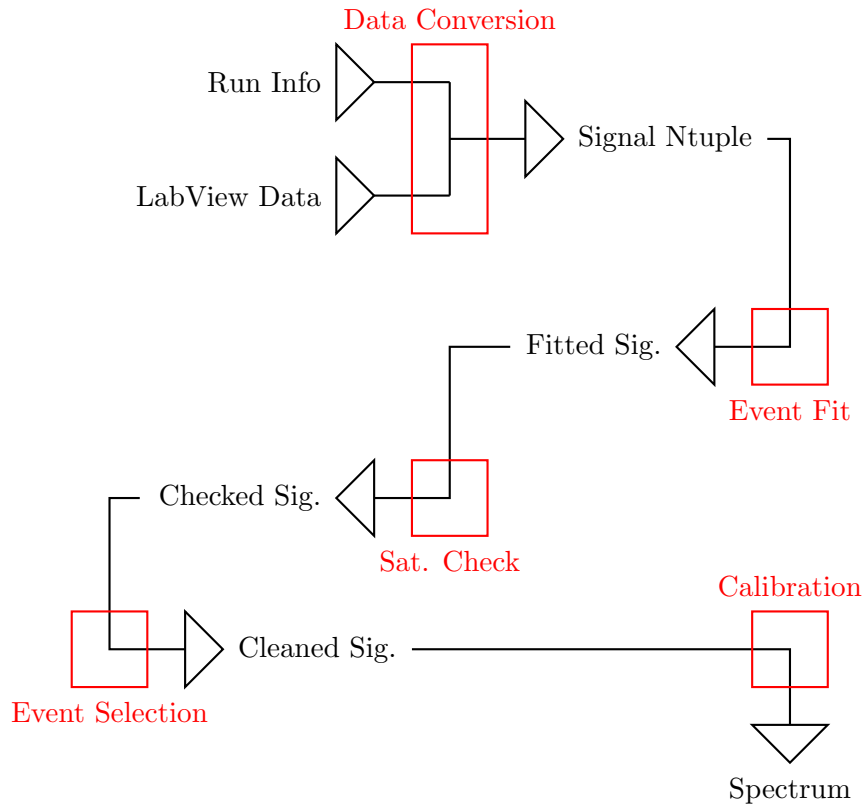
Figure 5.15: Schematic diagram of offline data processing.

are used to determine if the signal is saturated or not; an event selection based on results of the signal fit and saturation determination is made; an energy–event-value calibration is applied and a spectrum is produced. The analysis was broken into these steps in order to facilitate changing any one part.

5.3.1 *Event Fitting*

The amplitude of an SDD signal above the baseline corresponds linearly to the energy deposited in the detector by the incoming particle. The shape of the signal around its peak is approximately Gaussian; however, outside this region the signal is not perfectly Gaussian. Therefore we cannot fit the whole signal with a Gaussian shape plus a pedestal to get both the amplitude and the baseline. Instead, we fit the peak and the samples before the signal separately (figure 5.13). To determine the baseline throughout the entire signal, we fit the first approximately 2 μs with a constant pedestal plus a Gaussian function that describes the start of the signal. To determine the signal amplitude, we fit a symmetric 2 μs window around the peak time with a Gaussian function, and record the difference between the peak value and the baseline.
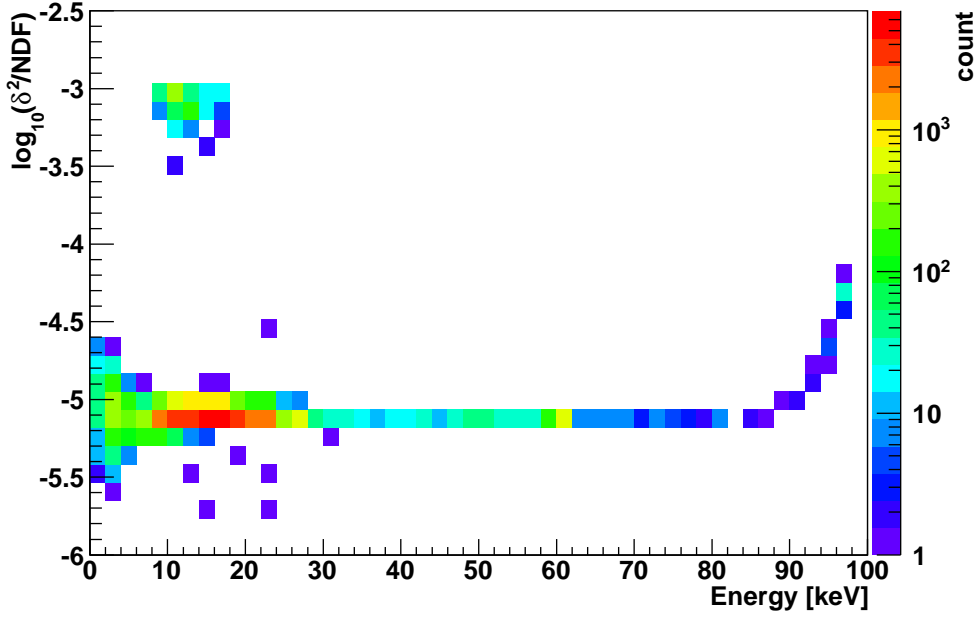
Figure 5.16: δ^2/NDF distributions as a function of event energy for a background run.

5.3.2 *Saturated-Signal Rejection*

Saturated signals (figure 5.14) are not Gaussian in shape and are thus ill fit by the event fitting described above. They can be rejected by looking at the goodness of fit in the same way as described in the section 5.3.3.

5.3.3 *Noise Rejection*

A visual investigation of the pulses revealed two different classes of signal: one that contained one peak, which the baseline and amplitude fits mentioned above matched well to; and one that contained multiple peaks, which the fits did not match well to. The poorly fitted pulses were clearly due to noise. To measure the goodness of the signal fitting, we define

$$\delta^2 = h^{-2} \sum_i [V_i - f(t_i)]^2, \tag{5.5}$$

where V_i and t_i are the voltage and time of the ith voltage sample, $f(t_i)$ is the fitted voltage at time t_i, and h is the maximum voltage of the event samples. Figure 5.16 shows δ^2 divided by the number of degrees of freedom (NDF) in the fit, for the Gaussian fit of the signal peak as a function of the signal peak height above the baseline. The cluster of events at large δ^2/NDF and low energy are the multipeak noise events. Requiring $\delta^2 < 10^{-4}$ rejects these erroneous signals.
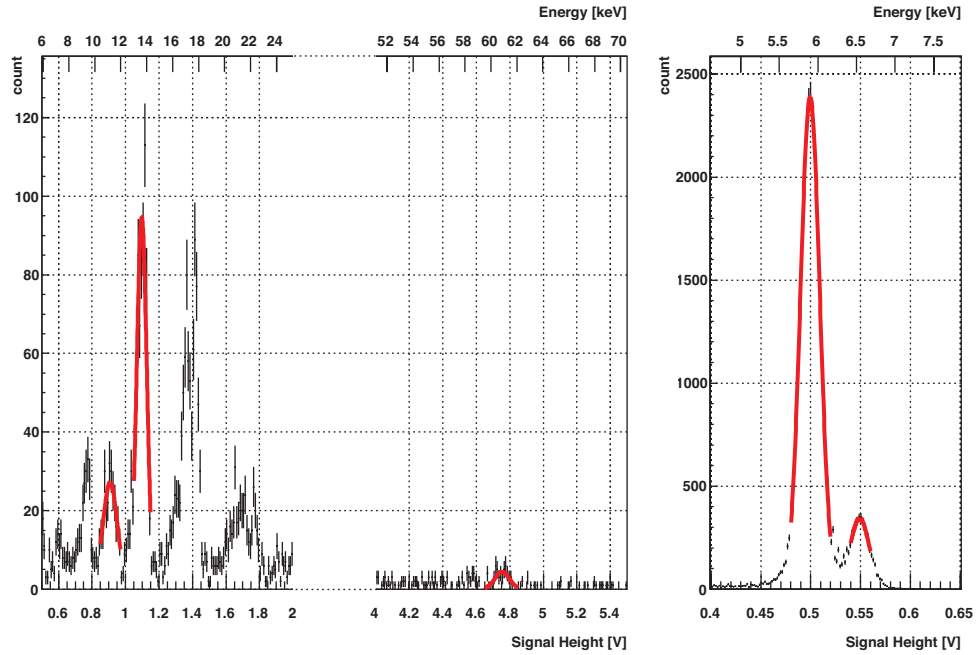
Figure 5.17: ^{241}Am (left) and ^{55}Fe (right) X-ray spectra with fitted calibration peaks.

5.3.4 *Detector Calibration*

To calibrate the detector and readout system, we record the spectra of the known X-ray sources ^{55}Fe and ^{241}Am (figure 5.17). The two sources provide X-rays at many energies between 5 keV and 60 keV, allowing us to measure the proportionality of the detector's signal amplitude to T_{dep} (figure 5.18) and to check the linearity of the detector response.

Since X-rays deposit their energy locally and uniformly inside the silicon, these sources also allow us to measure the energy resolution of the detector and our read-out system without influences from any dead layer structure. The resolution, here defined as the FWHM of an energy peak, is greatly affected by the temperature of the detector. Figure 5.19 shows the X-ray spectra from an ^{55}Fe source measured at room temperature and at $-20\,^{\circ}$C. At room temperature, the detector has resolutions at the Mn Kα line of ^{55}Fe (5.9 keV) greater than 400 eV. When cooled to temperatures below $0\,^{\circ}$C, the detector reaches resolutions around 150 eV at the same line.

5.4 GAS PURITY

The frictional cooling effect and the operation of the open SDD require that the moderating gas be uncontaminated.

The detector has a dead layer of 30 nm of aluminum on top of the silicon that forms its active volume. As well, in the first approximately 200 nm of the
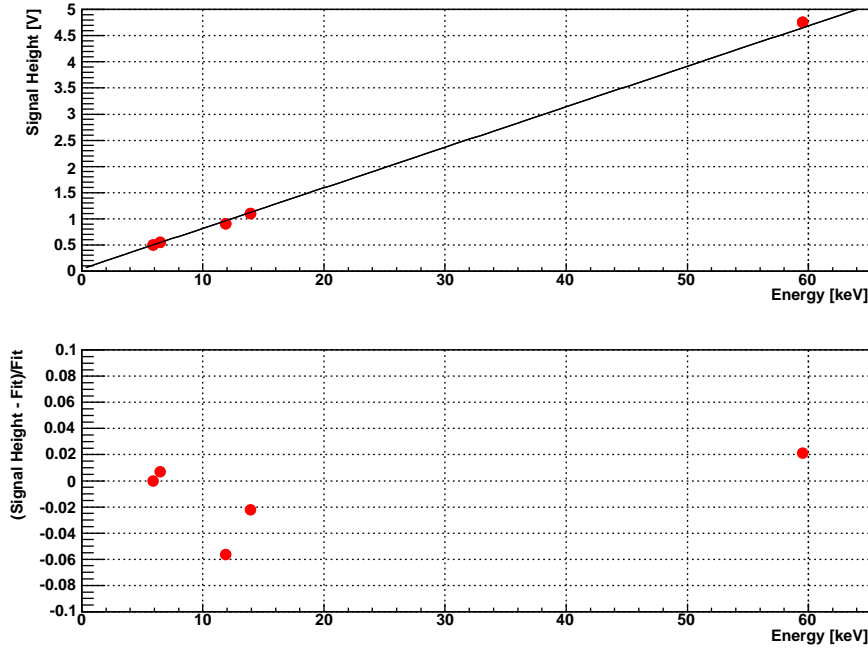
Figure 5.18: Signal-voltage–energy calibration fit for the spectra of figure 5.17.

silicon, the detector has a charge collection efficiency below 100%. In the energy range of interest, $T \lesssim 30$ keV, protons deposit a significant amount of energy in the aluminum and deposit their remaining energy largely in the region of reduced collection efficiency. Therefore, the SDD measures only 35% to 65% of the proton's energy (see section 7.2).

Impurities in the gas environment can build up on the detector's surface, which is the coldest surface in the experiment setup, increasing the amount of material that protons must traverse before entering the active layers of the detector. Even a thin layer of built-up gas impurities significantly reduces the amount of energy measured and, due to straggling in the trajectories of protons through the dead layers, greatly reduces the detector's energy resolution. The main sources of impurities are outgassing of molecules from the plastic pieces in the experiment construction and contamination of the gas from impurities either in the gas source or entering along the gas transfer line. The effects of outgassing can be greatly reduced by pumping the gas cell down to a low pressure (10^{-6} mbar) for several days. During this time, the plastic pieces expel foreign molecules, leaving the environment cleaner for data-taking runs. All experiment components in close proximity to the accelerating grid must be cleaned with alcohol, to remove any dust particles that can initiate an electric breakdown. After being cleaned, these components must be kept in vacuum for several days to allow for the alcohol to outgas.

The boil-off from cryogenic liquids is used as an ultrapure gas source. The gas transfer lines are tightly sealed, capable of holding pressures down to 10^{-9} mbar, to prevent air leaking into the gas. As well, the transfer lines are entirely
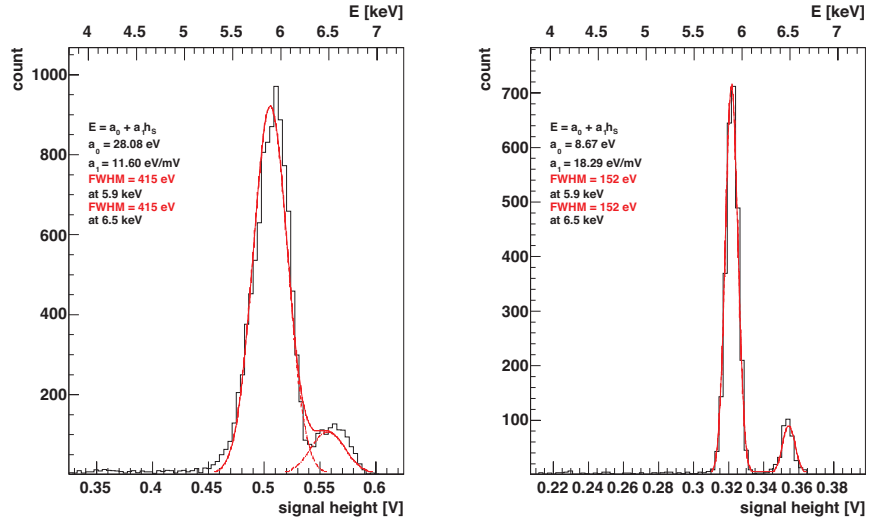
Figure 5.19: ^{55}Fe spectra taken with the SDD at room temperature (left) and cooled to $-20\,^\circ$C (right).

constructed from stainless steel, so no outgassing can contaminate the gas on the way from the source to the cell.

5.5 ELECTRIC BREAKDOWN

Breakdown of the electric field provided by the accelerating grid was observed taking place both outside the gas cell and inside the gas cell. Such breakdowns interfere with the experiment by preventing the establishment of a stable electric field and by damaging the SDD or its electronics.

5.5.1 *Breakdown Outside the Gas Cell*

Due to the large electric field strengths it provides, the accelerating grid must be kept in high vacuum ($P < 10^{-4}$ mbar) in order to prevent breakdown of the electric field between grid rings. Even at high vacuum, breakdown can occur if the wire carrying the high voltage comes too near to lower voltage rings or grounded pieces. Such breakdowns were observed in early versions of the experiment construction in which the high voltage was led to the HV ring by a Teflon-insulated wire that passed along the length of he accelerating grid. Electric discharges originated at the HV ring and traveled down the surface of the wire's insulation to the grounded detector flange, when high voltages as low as 15 kV were applied to the HV ring. To prevent this from occurring, the construction was altered to bring high voltages to the HV ring from the opposite side (figure 5.5)

The gas seal at the source side of the cell must be very tight since it is at the HV end of the grid. A small leak can stream gas over the rings, creating

a path for breakdown between them. It can also provide a path for charge to flow in a breakdown from inside the gas cell to the HV ring. Both breakdown mechanisms were observed in an early version of the experiment construction in which the proton source lollipop was mounted directly through the gas cell wall. This construction did not create a tight-enough gas seal, and breakdowns were observed at gas pressures above several 10^{-1} mbar, when high voltages as low as 10 kV were applied to the HV ring. To prevent gas leaks causing such breakdowns, we constructed the source-holder platform described above. Installing it stopped such breakdowns.

5.5.2 *Breakdown Inside the Gas Cell*

Breakdown of the electric field also occurs entirely inside the gas cell. This can be particularly dangerous since a breakdown that strikes the detector can destroy it or the detector electronics. The frequency and strength of these breakdowns depends greatly on the source-holder platform.

We constructed two types of platform: one made of PEEK which does not alter the electric field of the accelerating grid; and one made of stainless steel or copper, which can be connected to the HV ring or left unconnected (floating), and alters the shape of the electric field at the HV end.

When the metal platform is connected to the HV ring, such a large current is drawn at any gas pressure that the high voltage supply is incapable of providing enough current to hold a voltage above 1 kV. However, when the platform is left floating, higher voltages can be reached before a breakdown from the platform to a point inside the gas cell occurs.

A photodiode, mounted onto an empty SDD housing that was mounted inside the gas cell in place of the detector, measured the light from discharges in the gas, allowing for measurement of the frequency of electric breakdown. We observed that discharges of a harmless size occurred frequently ($\gtrsim 1$ Hz), but did not drain enough current to alter the voltage. However, above a voltage threshold that depends on the pressure of the gas in the cell, we observed large discharges occurring with higher frequency. These discharges prevented the high-voltage supply from providing a constant voltage. Figure 5.20 shows the measured dependence of the threshold voltage V_{br} on gas pressure p. Such breakdown has been described by Paschen's equations for discharge between two parallel plate electrodes [113],

$$V_{\mathrm{br}} = \frac{Bpd}{\ln(Apd) - \ln(\ln(1 + \gamma^{-1}))} \tag{5.6}$$

where d is the distance over which the discharge takes place, A and B are the Townsend coefficients, and γ is the secondary emission coefficient. Coefficients A, B, and γ are different for each gas. Though the conditions for breakdown in gas with no electrodes present (as is the case in the FCD cell) have not been thoroughly investigated[*], the Paschen formula can still give us a clue as to the

---

[*]See [114], one of the few publications on the subject; though it is concerned with discharge with AC fields, rather than DC fields.
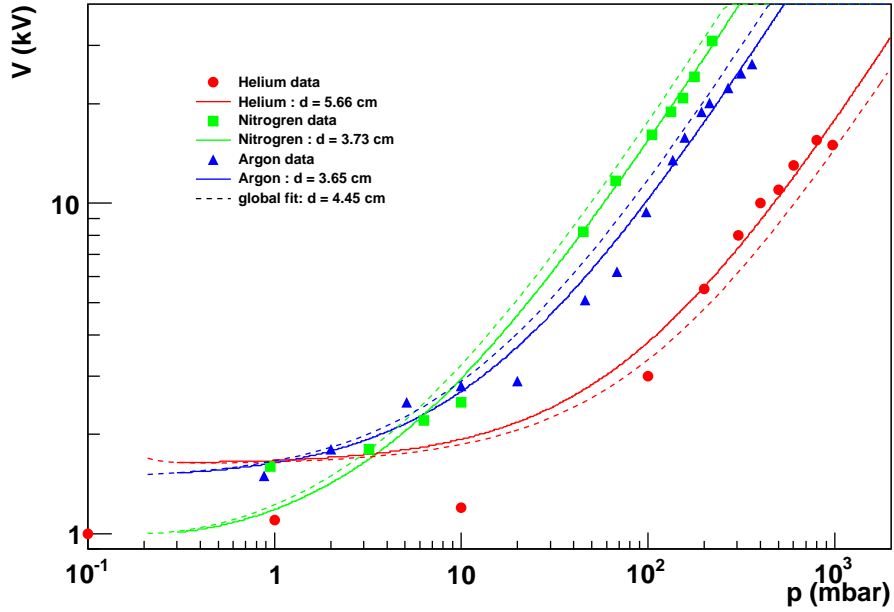
Figure 5.20: Threshold voltage for breakdown of the electric field inside the gas cell for helium, nitrogen, and argon with a floating metal source-holder platform.

order of size of the distance traversed by the avalanche of electrons in the breakdown. We fit the Paschen equation to our measurements, with the addition of an offset voltage V_0 to equation (5.6), with d and V_0 as the only free parameters. The best fit indicates a discharge distance on the order of half the size of the gas cell.

Tests conducted with the PEEK platform and americium source indicate that charge freed from the gas by the americium alphas builds up on the platform until a breakdown occurs from the platform to the HV ring. These breakdowns create large discharges and are fatal to the detector and detector electronics. However, these breakdowns do not occur when the seal between the PEEK platform and the end of the gas cell is made gas tight, closing the path for charge to take during a breakdown. In the gas-tight cell, electric fields of strengths up to $650\,\text{kV/m}$ have been reached without breakdown at gas pressures from 10^{-7} mbar to 1.25 bar.

FCD Simulation

Using CoolSim, we simulated the trajectories of protons in the FCD cooling cell. The simulated cell was exactly as described in chapter five: The electric field in the simulation is that of figure 5.6, calculated by successive overrelaxation. The proton source is taken to be a point source located on the z axis at the center of the 5th grid ring ($z = 20$ mm). The detector surface is located at $z = 100$ mm and is a 10 mm^2 circular surface centered on the z axis.

In the following discussion all results are taken from simulation runs in which ten thousand protons were simulated for combinations of electric field strengths between 0.1 MV/m and 0.5 MV/m, corresponding to high voltages between 10 kV and 50 kV; and helium gas densities between 1.6×10^{-4} mg/cm^3 and 1.2×10^{-1} mg/cm^3, corresponding to pressures (at room temperature) between 1 mbar and 700 mbar.

6.1 PROTON ENERGY

In each simulation run, protons start at rest and accelerate through the gas in the positive z direction, approaching the equilibrium energy, but not necessarily reaching it before crossing the detection plane 80 mm away. Figure 6.1 shows the change of the kinetic energy distribution as a function of depth traversed for a sample run in which the electric field strength is $E = 0.15$ MV/m and the helium density is $\rho = 1.63 \times 10^{-3}$ mg/cm^3 (10 mbar at room temperature). The mean energy of the protons approaches the equilibrium energy for this combination of field strength and gas density ($E/\rho \approx 0.9$ MV cm^2/mg), approximately 8 keV.

Scattering can be seen in the highlighted trajectory of figure 6.1: after scattering into a direction opposed to the electric field, the proton decelerates, turns around, and then reaccelerates. This produces the abrupt kinetic energy fluctuation seen in the highlighted trajectory.

For each combination of electric field strength and gas pressure the mean of the kinetic energy distribution at the SDD ($z = 10$ cm, $r \leq 1.78$ mm) is calculated; figure 6.2 shows the results for the simulation runs. For a fixed electric field strength, raising the gas pressure increases the energy loss to the helium, decreasing the mean energy at the detector. For a fixed gas pressure, raising the electric field strength increases the restorative energy gain, increasing the mean energy. Both behaviors are as expected from figure 3.1.
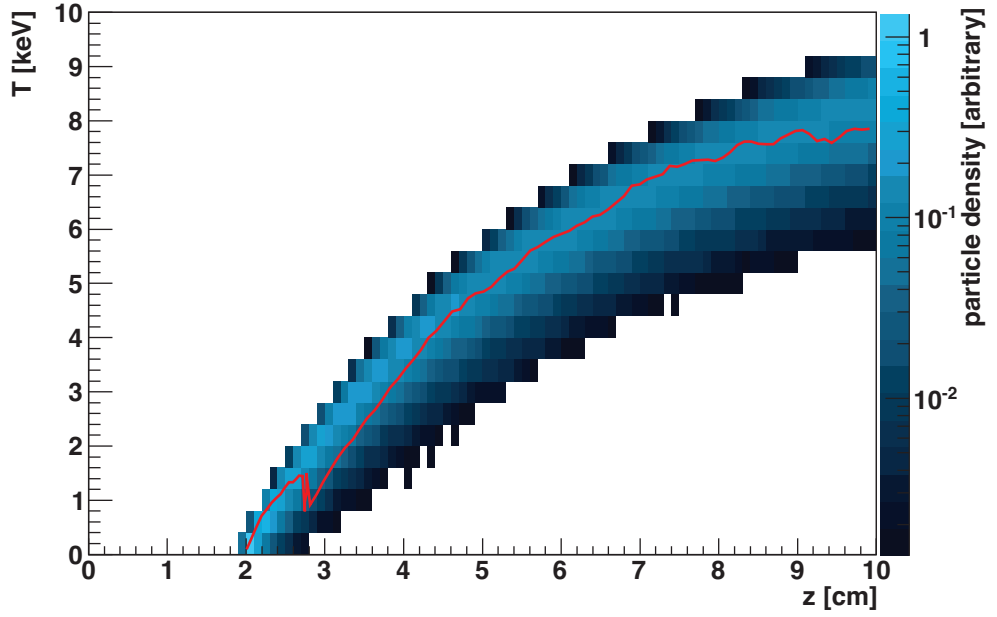
Figure 6.1: Simulated kinetic energy distributions of protons (shaded) and the kinetic energy of a single proton (line) as a function of z in the FCD cooling cell filled with helium gas at 1.63×10^{-3} mg/cm^3 and an electric field strength of 0.15 MV/m.

6.2 DETECTOR ACCEPTANCE

As they accelerate, protons interact with the helium gas, scattering away from the z axis and decreasing acceptance in the SDD, which has a radius of 1.78 mm. Figure 6.3 shows the acceptance of the SDD as a function of electric field strength divided by the helium gas density. The mean free path for scattering decreases with increasing density, causing more muons to scatter away from the SDD at higher densities. A stronger electric field refocuses more of those scattered protons towards the detector than a weaker field. The larger the ratio of the field strength to the density—the accelerating power divided by unit charge—the higher the acceptance of the detector. The acceptance of the detector is zero for ratios below approximately 0.3 MV $\cdot$ cm^2/mg.

6.3 EFFECTIVE-CHARGE CONTRIBUTION

The agreement between the analytical calculations of chapter three and the Monte-Carlo simulation is best seen in figure 6.4. It shows the analytically calculated E/ρ required to achieve T_{eq} for a proton with effective charge accounted for (●) and without (○)—the identical calculation as was used for muons in figure 3.9. The figure also plots E/ρ versus the mean kinetic energy of protons at the detection plane in the simulation (colored squares) for several densities
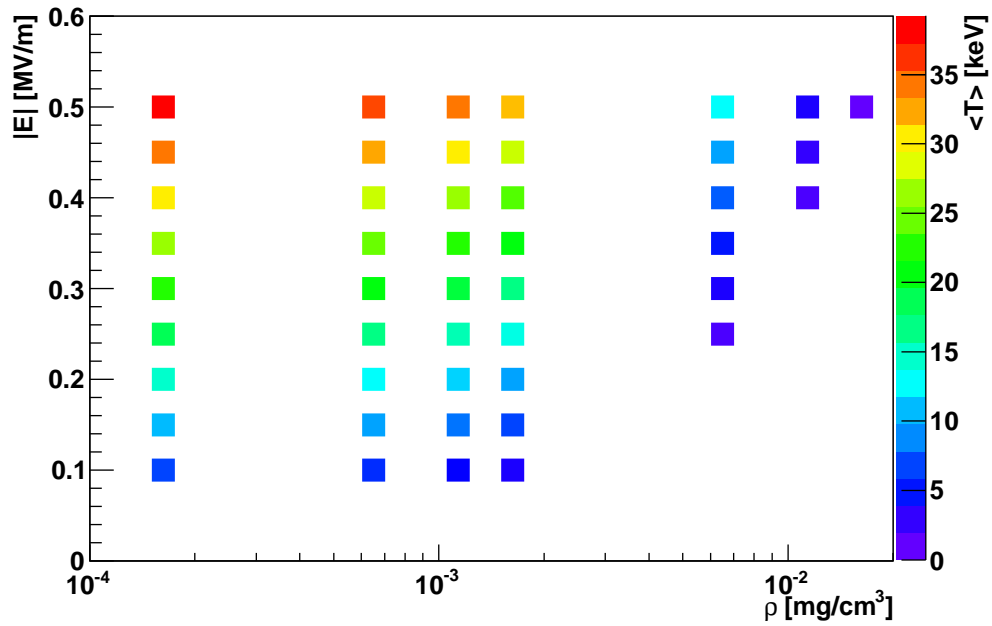
Figure 6.2: Simulated mean kinetic energy of protons at the SDD as a function of electric field strength and helium gas density.

of the helium gas. It is important to note that the mean kinetic energy at the detection plane is not necessarily the T_{eq} for the simulated E/ρ. At the lighter densities of gas, 80 mm is not a long enough distance for the protons to accelerate up to T_{eq}; therefore these data points are shifted down to lower energies.

The higher densities of the helium gas require greater strengths of the electric field than the lower densities to achieve the same E/ρ. The higher strengths of the field accelerate the protons up to or nearly up to T_{eq} before they reach the detection plane. The results of the three most dense set of runs shown in figure 6.4 conform to the analytic calculation that accounts for effective charge, confirming that CoolSim correctly handles this process in this density range.
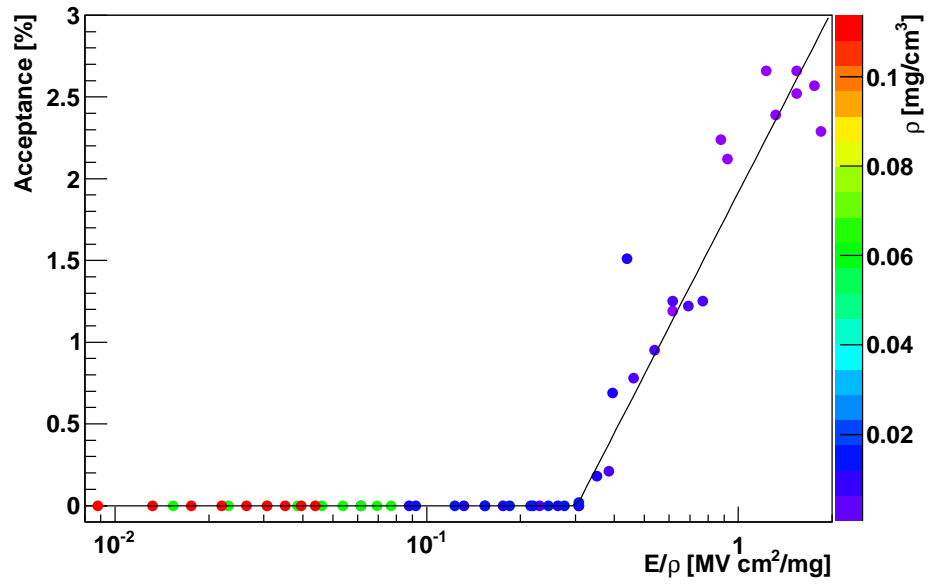
Figure 6.3: Simulated detector acceptance as a function of electric field strength per unit density, with the density of the helium indicated by the color of the marker.
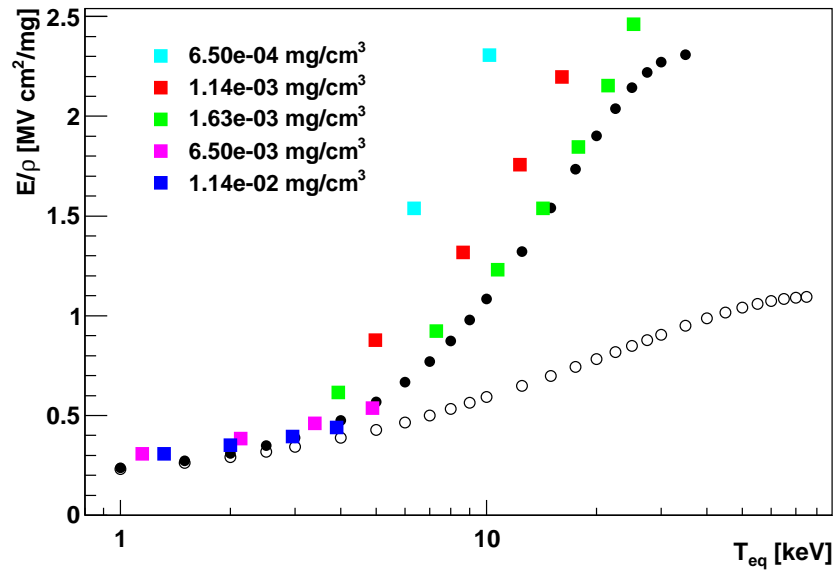
Figure 6.4: Field strength per unit density required to achieve the desired T_{eq} as a function of T_{eq} for protons in helium with ($\bullet$) and without ($\circ$) accounting for effective charge; and mean kinetic energy of the proton beam in the FCD simulation in helium given the designated E/ρ for several densities of the gas (colored squares).

70

CHAPTER 7

First FCD Measurements

We have made several measurements using the parts of the full experiment setup to calibrate the detectors (section 5.3.4) and measure the effect of their dead layers, as well as to measure the x-ray background, and verify the production of protons. All of the following measurements were made with the proton source, with a 23-μm-thick Mylar foil, mounted in the accelerating grid at $z = 20$ mm and the detector cooled to approximately 15 °C. Background and gasless proton measurements were made with the gas cell evacuated. The total data-taking rate was approximately 10 Hz. The x-ray rate was approximately 1.5 Hz; the proton rate was approximately 2 Hz; and the remaining rate was due to saturated pulses from MeV alpha particles.

7.1 BACKGROUND

The ^{241}Am in the proton source emits x-rays in the energy range of interest for the proton measurements ($E \lesssim 30$ keV). The observed rate of x-rays is comparable to that of protons, so the background energy spectrum must be measured for subtraction from the proton energy spectra. The background spectrum, shown in figure 7.1, contains several peaks from the ^{241}Am spectrum as well as low-amplitude noise, and possibly fluorescence peaks from the silicon and aluminum of the detector (at approximately 2 keV). To reduce the low-amplitude noise rate, a voltage threshold corresponding to an energy threshold of 1 keV is used in data recording. The probability that the x-rays interact in the SDD, which is 450 μm thick, rapidly decreases with increasing energy in the range of interest. Table 7.1 lists the branching ratio (BR); detectability (D), defined as the percentage of x-rays that pass through the detector that interact in its sensitive volume; and detectable branching ratio (BR $\cdot D$) for the prominent x-ray lines.

7.2 PROTON OBSERVATIONS

To understand the effect of the helium gas on the energy distribution of protons accelerated through it, we first had to measure the energy distribution of protons with no gas present in the cell. Energy spectra were measured with electric field strengths evenly spaced from 70 kV/m to 300 kV/m in 10 kV/m steps.

   The background spectrum ($E = 0$ kV/m) and proton spectra ($E > 0$ kV/m) were analyzed together to discover the overall background rate and the signal
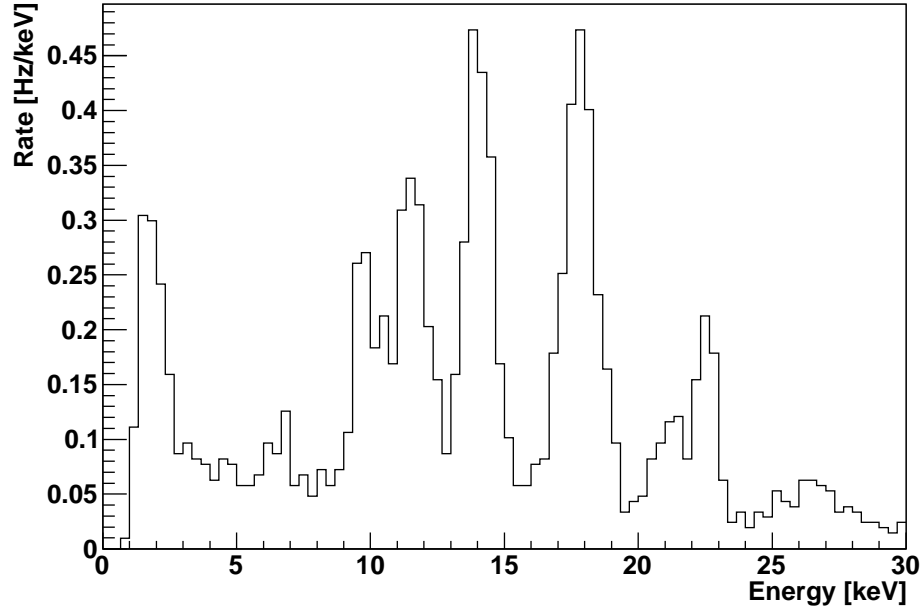
Figure 7.1: Background spectrum with ^{241}Am source present, the gas cell evacuated, and no voltage placed on the accelerating grid.

rate above that background for each spectrum. Each measured spectrum is divided into two regions: the portion below the expected energy of protons according to the numerically calculated potential difference between the proton source and the SDD given the applied high voltage of the run; and the portion of the spectra above this energy. Bins of the spectrum histogram below the expected energy boundary are assumed to contain contribution from signal and background; bins above the boundary contain only background contributions. The information from all measured spectra are then used to calculate the background rate and the individual signal rates in each bin for each run according to Poisson statistics. The signal rates are then extracted bin by bin for a particular run, and this is referred to as the spectrum with the background subtracted.

Figure 7.2 shows an example resultant spectrum, for $E = 230 \, \text{kV/m}$. The background spectrum as calculated from all the measured spectra is shown for comparison. The spectrum has a prominent proton peak centered around approximately 11 keV, which is lower than the 18.4 keV expected from the calculation of the electric field. The discrepancy is due to energy deposition in the dead and partially inactive layers of the detector. The peak has a FWHM of approximately 2 keV. This is larger than the x-ray energy resolution at the same energy, but is as expected from the distribution of proton energy loss in the dead layers.

The proton peak also has a tail to lower energies. This is due to protons striking the outer edges of the detector surface where they encounter larger dead layers. The increase in the low-energy noise above the background rate may be

Energy (keV)	BR (%)	D (%)	BR $\cdot D$ (%)
11.87	0.66	92	0.61
13.76	1.07	81	0.87
13.95	9.6	79	7.6
15.86	0.15	62	0.10
16.11	0.18	61	0.11
16.82	2.5	58	1.4
17.06	1.5	56	0.8
17.50	0.65	54	0.35
17.99	1.37	51	0.70
20.78	1.39	36	0.50
21.10	0.65	35	0.23
21.34	0.59	35	0.20
21.49	0.29	34	0.10
26.34	2.40	23	0.56
59.54	35.90	3	1.21

Table 7.1: Energies, branching ratios (BR), detectability (D), and BR $\cdot D$ for x-rays emitted by ^{241}Am with branching ratio greater than 0.2%

due to fluorescence of the silicon and aluminum of the detector, which produces peaks in this range.

Figure 7.3 shows five of the proton spectra. The peak centers are evenly spaced in accordance with the field strengths at which they were measured. As well, the proton rate remained nearly constant with changing electric field strength, as we expect since the gas cell is evacuated.

7.3 SDD RESPONSE TO PROTONS

The surface of the SDD that is exposed to the gas cell, through which the protons enter the detector, is covered in 30 nm of aluminum, which acts as an electrode for the voltage that depletes the active layers of the detector. Protons, which lose energy continuously along their trajectory through matter, deposit a significant amount of their energy in the aluminum layer (approximately 2 keV for protons in the energy range of the FCD experiment). A SDD functions by collecting the electrons ionized out of the detector bulk by the radiation being detected. It outputs a signal proportional to the amount of charge collected. None of the electrons ionized by the proton in the aluminum layer are collected, therefore none of the energy deposited in this layer is measured.

As well, the initial layers of the silicon closest to the aluminum do not have a 100% efficiency to collect electrons created by the protons. The charge collection efficiency is typically around 40% near the aluminum-silicon interface, and then rises to 100% within several hundred nanometers [115, 116]. (The exact shape varies depending on the silicon wafer from which the detector is cut.)
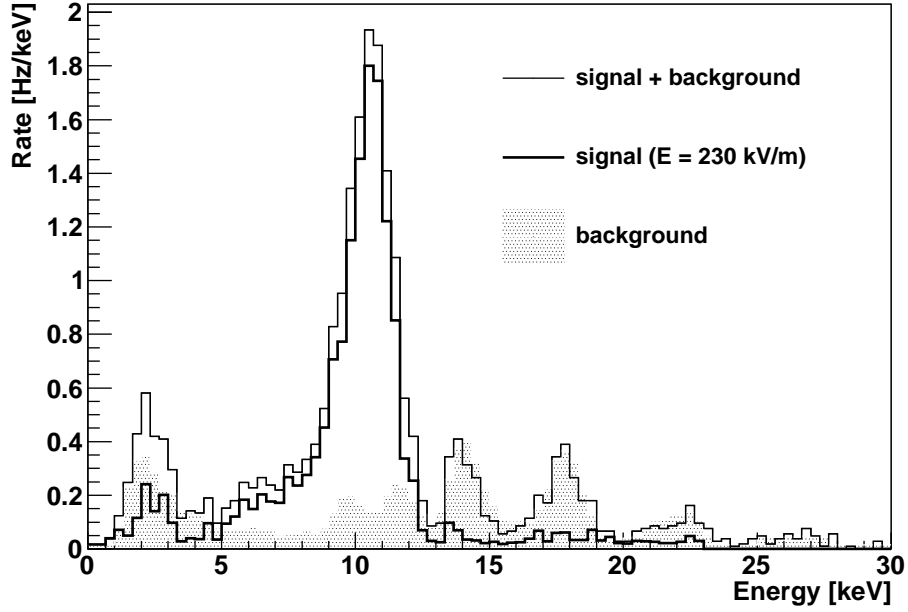
Figure 7.2: Energy spectrum for an $E = 230\,\mathrm{kV/m}$ run: full spectrum (line), background-removed spectrum (thick line), and background (highlighted).

The upper plot of figure 7.4 shows the measured proton energy T_{meas} as a function of the expected proton energy T_{exp}. The measured energy is obtained from the energy spectra that are discussed in section 7.2 by first subtracting the background, and then fitting the remaining peak with a Gaussian distribution to obtain the mean. The expected proton energy is equal to the potential difference between $z = 20\,\mathrm{mm}$ and $z = 100\,\mathrm{mm}$ times unit charge, for the on-axis field shown in figure 5.6.

As mentioned above, the region of decreased charge collection efficiency has thickness on the order of 100s of nanometers. This is also the order of size of the penetration depth of keV protons. The higher-energy protons travel further into the detector, depositing a larger ratio of their energy in fully active layers of the detector. The bottom plot of figure 7.4 shows the fraction of the expected proton energy that is measured by the SDD.

The lowest energy run in figure 7.4, for which $E = 70\,\mathrm{kV/m}$, has $T_{\mathrm{meas}} = 0\,\mathrm{keV}$ because after depositing energy in the dead layers, the protons didn't have enough energy left to be measureable above the low-energy threshold, which vetoes electronic noise in the detector readout system. Any further build up of a dead layer increases the minimum energy protons must have in order to be detectable. Thus it is vitally important to keep impurities out of the gas in the cell, since they will deposit on the surface of the detector and increase the thickness of the dead layer.
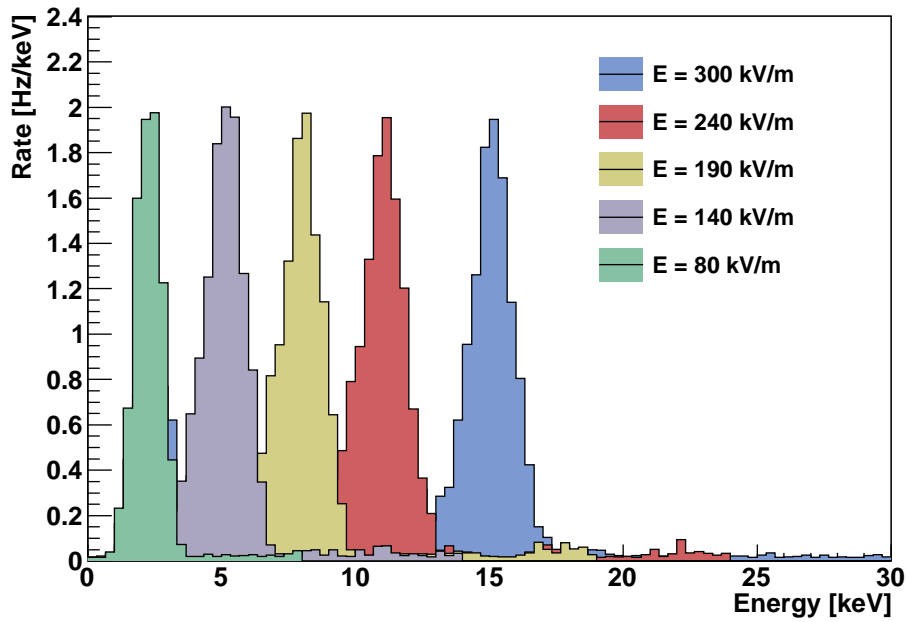
Figure 7.3: Proton energy spectra, with background removed, for five representative strengths of the electric field.

7.4 CURRENT STATUS & FUTURE OF THE EXPERIMENT

As detailed in the previous chapters, all individual parts of the experiment—the gas cell, accelerating grid, detector system, and proton source—have been commissioned, and a Monte Carlo simulation package has been built up for simulating the full experiment. Spectra have recently been recorded for low densities of the helium gas—too low to test the cooling effect, but high enough to investigate some of the effects of charge exchange processes in helium gas. We will continue analysis of these spectra, and will investigate solving the gas-purity issues in order to measure spectra at higher gas densities and record spectra that will allow us to validate our simulations of the cooling effect.
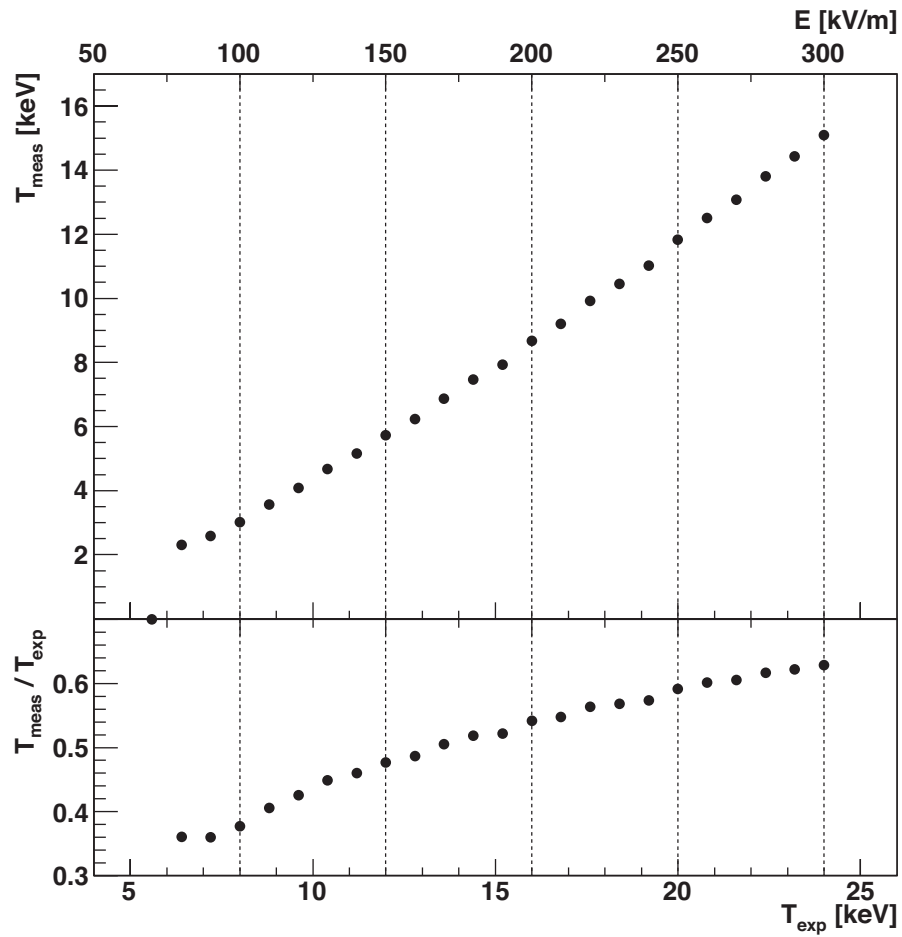
Figure 7.4: SDD-measured energy as a function of expected proton energy (top) and the ratio of measured to expected energy as a function of expected energy (bottom).

The reader will notice a signficant shift in topic for the next two chapters. Up to this point, this work has been concerned with muon colliders and frictional cooling. As we presented in chapter two, the discovery potential of BSM physics at a muon collider is one of the motivations behind its development. The next chapter discusses in detail a particular BSM physics model called universal extra dimensions; the chapter following it describes the phenomenology of the model at a muon collider.

CHAPTER 8

Universal Extra Dimensions

In 1914, Gunnar Nördstrum discovered that classical electromagnetism and gravity could be simultaneously described by tensors in five dimensions [117]: "a uniform treatment of electromagnetic and gravitational fields is possible, if one treats four-dimensional spacetime as a surface in a five-dimensional world."[*] This concept was rediscovered a few years later by Theodor Kaluza in an attempt to unify classical electromagnetism with general relativity [118]. Oskar Klein then introduced the concept of compactifying the extra dimension [119]. The interesting story of the initial development of what came to be known as Kaluza Klein (KK) theory is told in [120, 121]. Kaluza Klein theory was first developed at an unfortunate time, when many of the proposals were quickly made obsolete by the rapid advancements in general relativity and quantum physics. And what ideas remained valid were quickly set aside as those who developed them set their attention to further developing quantum physics.

In the last twenty years, several modern versions of KK theory have been posited to address such issues as gauge-coupling unification and the hierarchy problem [122], proton decay [123], the hierarchy of fermion generations [124, 125], and electroweak symmetry breaking [126]. They are characterized by the number of extra dimensions, their shapes, and which of the SM fields permeate them. For a good survey of these theories see [127, 128].

A natural KK model is that of universal extra dimensions [33], which posits the existence of compact flat extra dimensions accessible to all standard-model fields. To describe these extra dimensions we use the following notation: The total number of dimensions of the theory $d = (4 + \delta)$, δ being the number of extra space dimensions. Coordinates in the d-dimensional space are written as $X^M = (x^\mu, y^a)$, with uppercase roman letters running over all d dimensions; x, is a coordinate in the usual 4D spacetime, with lowercase Greek indices; y is a coordinate in the compact δ-dimensional space, with lowercase roman indices running over $5, \ldots, 4 + \delta$.

The effective 4D theory is described by the Lagrangian obtained by integrating out the extra dimensions,

$$\mathscr{L}_4(x^\mu) = \int \mathrm{d}^\delta y \; \mathcal{L}_\delta(x, y). \tag{8.1}$$

---

[*] "eine einheitliche Behandlung des elektromagnetischen Feldes und des Gravitationsfeldes möglich ist, wenn man die vierdimensionale Raumzeitwelt als eine durch eine fünfdimensionale Welt gelegte Fläche auffaßt."

Compactifying each of the extra dimensions associates a coordinate y^a with $(y^a + 2\pi R_a)$, with $2\pi R_a$ being the size of dimension a. To see the effects of compactification, we will take as an example a single extra dimension, compactified as the 1D sphere S^1 with radius R, and a real scalar field Φ. We can Fourier expand the field in terms of even and odd modes in y as

$$\Phi(x,y) = \frac{1}{\sqrt{2\pi R}} \left(\phi_+^0 + \sqrt{2} \sum_{n=1}^{\infty} \left[\phi_+^n \cos \frac{ny}{R} + \phi_-^n \sin \frac{ny}{R} \right] \right), \qquad (8.2)$$

with the standard-model field ϕ_+^0 and the KK$_n$ modes $\phi_\pm^n$ depending only on x. The kinetic term in the 4D Lagrangian is

$$
\begin{aligned}
\mathscr{L}_4^{\text{kin}} &= \int_{-\pi R}^{\pi R} \mathrm{d}y\; \frac{1}{2} \partial_M \Phi \partial^M \Phi = \int_{-\pi R}^{\pi R} \mathrm{d}y\; \frac{1}{2} \partial_\mu \Phi \partial^\mu \Phi - \frac{1}{2}(\partial_y \Phi)^2 \\
&= \frac{1}{2\pi R} \int_{-\pi R}^{\pi R} \mathrm{d}y\; \frac{1}{2} \partial_\mu \phi_+^0 \partial^\mu \phi_+^0 \\
&\quad + \frac{1}{\pi R} \int_{-\pi R}^{\pi R} \mathrm{d}y\; \sum_{m,n} \left[\partial_\mu \phi_+^m \partial^\mu \phi_+^n - \frac{n^2}{R^2} \phi_+^m \phi_+^n \right] \cos \frac{my}{R} \cos \frac{ny}{R} \\
&\quad + \frac{1}{\pi R} \int_{-\pi R}^{\pi R} \mathrm{d}y\; \sum_{m,n} \left[\partial_\mu \phi_-^m \partial^\mu \phi_-^n - \frac{n^2}{R^2} \phi_-^m \phi_-^n \right] \sin \frac{my}{R} \sin \frac{ny}{R} \\
&\quad + \dots \\
&= \frac{1}{2} \partial_\mu \phi_+^0 \partial^\mu \phi_+^0 + \sum_{n=1}^{\infty} \partial_\mu \phi_\pm^n \partial^\mu \phi_\pm^n - \frac{n^2}{R^2} \phi_\pm^n \phi_\pm^n, \qquad (8.3)
\end{aligned}
$$

where terms integrating to zero have been omitted in the intermediary step. The 4D kinetic term contains new terms resembling masses for the KK$_n$ excitation modes; these are the quantized momenta in the y direction. So the KK modes have masses,

$$m^2 = m_0^2 + p_y^2 = m_0^2 + m_n^2, \quad m_n = \frac{n}{R}. \qquad (8.4)$$

A similar result is obtained for a gauge field,

$$A_M(x,y) = \frac{1}{\sqrt{2\pi R}} \left(A_{+M}^0 + \sqrt{2} \sum_{n=1}^{\infty} \left[A_{+M}^n \cos \frac{ny}{R} + A_{-M}^n \sin \frac{ny}{R} \right] \right), \qquad (8.5)$$

where the kinetic term of the 4D Lagrangian is

$$
\begin{aligned}
\mathscr{L}_4^{\text{kin}} &= -\frac{1}{2\pi R} \int_{-\pi R}^{\pi R} \mathrm{d}y\; \frac{1}{4} F_{MN} F^{MN} \\
&= -\frac{1}{2\pi R} \int_{-\pi R}^{\pi R} \mathrm{d}y\; \left[\frac{1}{4} F_{\mu\nu} F^{\mu\nu} + \frac{1}{2} \left(\partial_\mu A_5 - \partial_5 A_\mu \right) \left(\partial^\mu A^5 - \partial^5 A^\mu \right) \right] \\
&= -\frac{1}{4} F_{+\mu\nu}^0 F_+^{0\mu\nu} + \frac{1}{2} \partial_\mu A_5^0 \partial^\mu A_5^0 \\
&\quad - \sum_{n=1}^{\infty} \left[\frac{1}{4} F_{\pm\mu\nu}^n F_\pm^{n\mu\nu} - \frac{1}{2} \left(\partial_\mu A_{\pm 5}^n \mp \frac{n}{R} A_{\mp\mu}^n \right) \left(\partial_\mu A_{\pm 5}^n \mp \frac{n}{R} A_{\mp\mu}^n \right) \right],
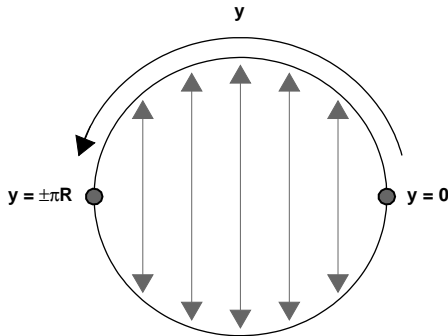\end{aligned}
$$

Figure 8.1: Illustration of the S^1 extra dimension with the coordinate identification of the P_y symmetry.

where $F_{MN} = (\partial_M A_N - \partial_N A_M)$. With a suitable choice of gauge [129], $A^n_{\pm\mu} \to A^n_{\pm\mu} + \frac{R}{n} A^n_{\pm 5}$ and $A^n_{\pm 5} = 0$ for $n > 0$, this becomes

$$\mathscr{L}^{\text{kin}}_4 = -\frac{1}{4} F^0_{+\mu\nu} F^{0\mu\nu}_+ - \sum_{n=1}^{\infty} \left[\frac{1}{4} F^n_{\pm\mu\nu} F^{n\mu\nu}_\pm + \frac{1}{2} \frac{n^2}{R^2} A^n_{\pm\mu} A^{n\mu}_\pm \right] + \frac{1}{2} \partial_\mu A^0_5 \, \partial^\mu A^0_5. \quad (8.6)$$

Again new mass terms arise, giving masses to the excitations of the gauge field. The same arises for each standard-model field that propagates in the extra dimension (the bulk), resulting in a tower of states for each SM particle with masses approximately $1/R$, $2/R$, $3/R$, etc.

8.1 ORBIFOLDING

An unwanted new feature of equation (8.6) is the last term, the kinematic term for a massless scalar arising from the fifth component of the zero mode. Another unwanted feature of compactifying on S^1 is in the fermion sector: In five dimensions, fermion fields $\psi(x, y)$ have four components and the Clifford algebra gives Dirac gamma matrices $\Gamma_M = (\gamma_\mu, i\gamma_5)$, with γ_μ and γ_5 the usual 4D Dirac matrices. The 5D fermions are thus vectorlike, and an additional symmetry is needed to reproduce chirality in the standard-model modes ($n = 0$).

Both unwanted features can be removed by orbifolding the extra dimension, introducing a new symmetry requirement on the Lagrangian [129, 130]. For a single extra dimension there is only one choice: $S^1/\mathbb{Z}_2$. This orbifolding consists of requiring all fields be even or odd under the $P_y : y \to -y$ transformation (figure 8.1)

$$P_y \Psi(x, y) = \mathcal{P}_y \Psi(x, y), \quad \mathcal{P}_y = \pm 1 \quad (8.7)$$

with the parity of fields assigned so that the Lagrangian remains invariant under the transformation. We redefine boson (Φ) and fermion (Ψ) fields on the orbifold

according to [131] by

$$\Phi(x, y) \quad \to \quad \frac{1}{2}\left[\Phi(x, y) + \mathcal{P}_y \Phi(x, -y)\right], \text{ and} \tag{8.8a}$$

$$\Psi(x, y) \quad \to \quad \frac{1}{2}\left[\Psi(x, y) + \mathcal{P}_y \gamma^5 \Psi(x, -y)\right], \tag{8.8b}$$

where y now runs from 0 to πR and the fields inside the brackets on the right-hand side are those of the S^1 theory without the $\mathbb{Z}_2$ constraint.

For the gauge field, invariance of $F_{\mu\nu}F^{\mu\nu}$ means that A_μ and A_y must have opposite $\mathcal{P}_y$ parity, since $\partial_\mu \to \partial_\mu$ and $\partial_y \to -\partial_y$. We assign $\mathcal{P}_y = +1$ to A_μ, and $\mathcal{P}_y = -1$ to A_y. Equation (8.5) becomes

$$A_\mu(x, y) \quad = \quad \frac{1}{\sqrt{\pi R}}\left(A_\mu^0(x) + \sqrt{2}\sum_{n=1}^{\infty} A_\mu^n(x)\cos\frac{ny}{R}\right) \tag{8.9a}$$

$$A_y(x, y) \quad = \quad \sqrt{\frac{2}{\pi R}}\sum_{n=1}^{\infty} A_y^n \sin\frac{ny}{R}. \tag{8.9b}$$

The zero mode of A_y disappears, and so does the unwanted massless scalar of equation (8.6).

Since $\mathcal{P}_y(\partial_y) = -1$, the invariance of the fermion kinetic term

$$\mathscr{L}_5^{\mathrm{kin}} = i\overline{\Psi}(x, y)\slashed{\partial}_M \Psi(x, y) = i\overline{\Psi}\slashed{\partial}_\mu\Psi + \Psi_{\mathrm{R}}\partial_y\Psi_{\mathrm{L}} - \overline{\Psi}_{\mathrm{L}}\partial_y\overline{\Psi}_{\mathrm{R}}, \tag{8.10}$$

$$\text{with } \Psi = \begin{pmatrix} \Psi_L \\ \overline{\Psi}_R \end{pmatrix},$$

requires Ψ's component spinors to have opposite $\mathcal{P}_y$ parity. The $\mathrm{SU}(2)_{\mathrm{W}}$ lepton doublet fields ($\mathcal{L}$) are assigned even parity for the left-handed component spinors, and the $\mathrm{SU}(2)_{\mathrm{W}}$ lepton singlet fields ($\mathcal{E}$) are assigned even parity for the right-handed component spinors

$$\mathcal{L}(x, y) \quad = \quad \frac{1}{\sqrt{\pi R}}\mathcal{L}_{\mathrm{L}}^0(x)$$

$$+ \quad \sqrt{\frac{2}{\pi R}}\sum_{n=1}^{\infty}\mathcal{L}_{\mathrm{L}}^n(x)\cos\frac{ny}{R} + \mathcal{L}_{\mathrm{R}}^n(x)\sin\frac{ny}{R}, \tag{8.11a}$$

$$\mathcal{E}(x, y) \quad = \quad \frac{1}{\sqrt{\pi R}}\mathcal{E}_{\mathrm{R}}^0(x)$$

$$+ \quad \sqrt{\frac{2}{\pi R}}\sum_{n=1}^{\infty}\mathcal{E}_{\mathrm{R}}^n(x)\cos\frac{ny}{R} + \mathcal{E}_{\mathrm{L}}^n(x)\sin\frac{ny}{R}, \tag{8.11b}$$

eliminating the zero modes of the right-handed doublet and the left-handed singlet. Thus the standard-model modes have the usual chirality—left-handed doublets and right-handed singlets—but the KK_n ($n > 0$) excitations of the doublet and singlet states have *both* left- and right-handed components

$$\mathcal{L}^n(x) \quad = \quad \mathcal{L}_{\mathrm{L}}^n(x) + \mathcal{L}_{\mathrm{R}}^n(x) \tag{8.12a}$$

$$\mathcal{E}^n(x) \quad = \quad \mathcal{E}_{\mathrm{L}}^n(x) + \mathcal{E}_{\mathrm{R}}^n(x). \tag{8.12b}$$

The same holds for the quark doublets $\mathcal{Q}(x, y)$, and singlets $\mathcal{U}(x, y)$ and $\mathcal{D}(x, y)$.
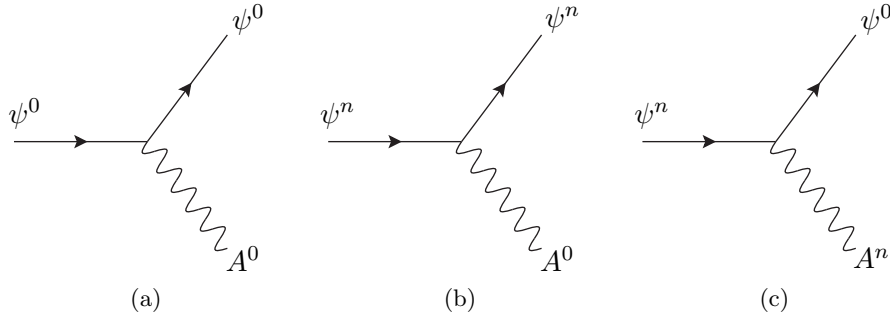
Figure 8.2: Allowed fermion–gauge-boson interactions involving one or two SM ($n = 0$) particles and zero or two KK excitations.

8.1.1 *Neumann & Dirichlet Boundary Conditions*

An equivalent picture of the projecting out of unwanted states is through the requirement of boundary conditions on a finite-sized extra dimension. If we take the extra dimension to be the interval $[0, \pi R]$, to preserve unitarity, the field current must vanish at the endpoints

$$i\Psi^\dagger \partial_y \Psi(x, 0) = i\Psi^\dagger \partial_y \Psi(x, \pi R) = 0. \qquad (8.13)$$

This is fulfilled by imposing at each endpoint either a Neumann boundary condition, $\partial_y \Psi = 0$, or a Dirichlet boundary condition, $\Psi = 0$. In terms of the Fourier expansions of the standard-model fields in y, this is mathematically equivalent to the orbifolding above: $\mathcal{P}_y$-even states obey Neumann boundary conditions at both endpoints; $\mathcal{P}_y$-odd states obey Dirichlet boundary conditions.

8.2 KK-NUMBER CONSERVATION & KK PARITY

When we integrate out the fifth dimension from the interaction term for the 5D fermions and gauge boson in the Lagrangian,

$$\mathcal{L}_5^{\text{int}} = e_5 \overline{\Psi}(x, y) \Gamma^M A_M(x, y) \Psi(x, y), \qquad (8.14)$$

with $e_5 = e\sqrt{\pi R}$, due to the orthogonality of the modes of the Fourier expansion, only terms respecting a conservation of KK number n_{KK} remain in the effective 4D Lagrangian. For example, the only allowed interactions involving standard-model modes come from the terms,

$$\mathcal{L}_4^{\text{int}} \supset e\overline{\psi^0}A\!\!\!/^0\psi^0 + e\overline{\psi^n}A\!\!\!/^0\psi^n + e\overline{\psi^0}A\!\!\!/^n\psi^n + \text{h.c.}, \qquad (8.15)$$

the diagrams of which are shown in figure 8.2. The conservation of momentum in the extra dimension manifests itself as KK number conservation after compactification. The same conservation rule applies at the tree level for all excitation levels and requires that the total n_{KK} carried into a vertex equal that carried out.

Figure 8.1 shows that two points get identified with themselves under the $S^1/\mathbb{Z}_2$ orbifolding, $y = 0$ and $y = \pi R$. The existence of these orbifold fixed points
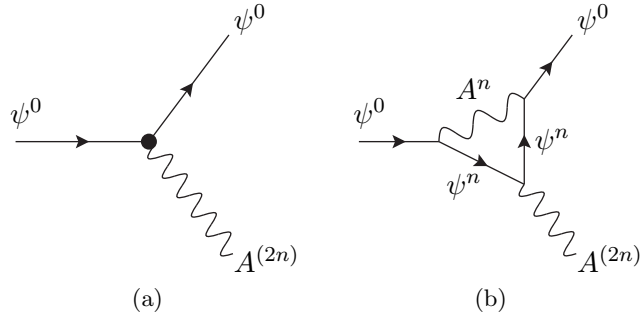
Figure 8.3: Allowed fermion–gauge-boson interaction involving SM particles that breaks n_{KK} conservation but preserves $\mathcal{P}_{\text{KK}}$. The effective vertex (a) is generated from the loop vertex (b).

breaks the translational symmetry in y that generates the n_{KK} conservation. However the symmetry under P_y still exists. As is shown explicitly in [131, 132], the conservation of n_{KK} is broken down to the conservation of KK parity, $\mathcal{P}_{\text{KK}} = (-1)^{n_{\text{KK}}}$. KK-number-violating, but KK-parity-conserving processes can occur at the fixed points (figure 8.3). However, the amplitudes for such interactions are suppressed from those of the KK-number-conserving interactions by the ratio of the volume of 4D space at the fixed points to the total volume of the 5D space. As well, due to gauge invariance, KK-number-violating interactions involving zero-mode gauge bosons may not occur [132].

8.3 MINIMAL-UED MASS SPECTRUM

Since experimental limits require $m_n \gg m_0$ (see section 8.4) for all but the heaviest standard-model particles,[*] the tree-level mass spectrum at each level n, calculated according to equation (8.4), is highly degenerate and decays of KK excitations are kinematically forbidden. For example, in the decay of a KK muon,

$$\mu_n \to \mu_{n'} + \gamma_{n-n'} \tag{8.16}$$

the difference in mass from the incoming to outgoing states is negative. However, the mass difference is very small, $\Delta m/m_{\mu_n} \approx -m_\mu^2/m_n^2$ (for $n' > 0$; $\Delta m/m_{\mu_n} \approx -m_\mu/m_n$ for $n' = 0$), with typical values of m_n in the range of hundreds of GeV to TeV. When radiative corrections to the masses are included, the spectrum degeneracy is lifted and the phase space for decays is enlarged.

The radiative corrections to the masses at each KK mode were calculated in [132]. In carrying out the calculations, the model is treated as an effective theory valid below an energy scale Λ at which possible contributions to the self-energies of the KK excitations at the fixed points is assumed to be small. We refer to the model with this assumption as minimal universal extra dimensions (mUED) theory. This assumption also prevents the mixing of KK modes due to loops involving violation of n_{KK} conservation at the fixed points.

---

[*]And even for these heavy particles, m_n for $n > 1$ is significantly larger than m_0.

We summarize here the results that are useful for the discussion in the next chapters, namely the mass corrections to the hypercharge (B) and weak (W^i) gauge bosons, and the lepton $SU(2)_W$ doublets and singlets. The mass corrections are calculated in two parts, those that arise from processes in the bulk, namely loops that wind around the y dimension, and those that arise at the orbifold fixed points. The bulk corrections are zero for $n = 0$ and independent of n otherwise:

$$\delta(m_{B_n}^2) = -\frac{39}{2}\left(\frac{g_1}{4\pi}\right)^2\frac{\zeta(3)}{\pi^2}R^{-2} \tag{8.17a}$$

$$\delta(m_{W_n}^2) = -\frac{5}{2}\left(\frac{g_2}{4\pi}\right)^2\frac{\zeta(3)}{\pi^2}R^{-2}, \tag{8.17b}$$

and

$$\delta m_{\mathcal{L}_n} = \delta m_{\mathcal{E}_n} = 0, \tag{8.17c}$$

where g_1 and g_2 are the weak hypercharge and isospin coupling constants, and ζ is the Riemann zeta function.

The fixed-point corrections depend on the cutoff scale Λ, which is here represented by the dimensionless parameter ΛR that indicates how many KK excitation levels are present below the cutoff scale:

$$\bar{\delta}(m_{B_n}^2) = -\frac{1}{3}\left(\frac{g_1}{4\pi}\right)^2\ln\left(\frac{\Lambda R}{n}\right)n^2R^{-2} \tag{8.18a}$$

$$\bar{\delta}(m_{W_n}^2) = 5\left(\frac{g_2}{4\pi}\right)^2\ln\left(\frac{\Lambda R}{n}\right)n^2R^{-2} \tag{8.18b}$$

$$\bar{\delta} m_{\mathcal{E}_n} = \frac{9}{2}\left(\frac{g_1}{4\pi}\right)^2\ln\left(\frac{\Lambda R}{n}\right)nR^{-1} \tag{8.18c}$$

$$\bar{\delta} m_{\mathcal{L}_n} = \left(\frac{9}{8}\left(\frac{g_1}{4\pi}\right)^2 + \frac{27}{8}\left(\frac{g_2}{4\pi}\right)^2\right)\ln\left(\frac{\Lambda R}{n}\right)nR^{-1}. \tag{8.18d}$$

The hypercharge boson B_n and the neutral weak isospin boson W_n^3 mix to produce the KK$_n$ photon and Z^0. Their squared masses are the eigenvalues of the matrix of squared masses of the B_n and W_n^3 with the usual electroweak mixing terms,

$$M^2 = \begin{pmatrix} m_{B_n}^2 & \frac{1}{4}g_1g_2v^2 \\ \frac{1}{4}g_1g_2v^2 & m_{W_n}^2 \end{pmatrix}, \tag{8.19}$$

with $m_{B_n}^2 = m_n^2 + \delta(m_{B_n}^2) + \bar{\delta}(m_{B_n}^2) + \frac{1}{4}g_1^2v^2$ and the squared mass of W_n similarly defined, and v the vacuum expectation value of the Higgs field. The largeness of $m_{B_n}^2$ and $m_{W_n}^2$ with respect to the mixing term causes the electroweak mixing angle to be much smaller for KK modes than for the standard-model modes. The mixing at $n > 0$ is nearly negligible, meaning that the KK photon and Z^0 are nearly pure B and W^3.

Figure 8.4 lists the masses of the first KK excitation level including the radiative corrections for a typical benchmark set of parameters $R^{-1} = 500$ GeV $\approx 10^{-19}$ m, $\Lambda R = 20$. (We use the helpful notation convention of [133], indicating $SU(2)_W$ doublet states with a superscript $\bullet$ and singlet states with a superscript
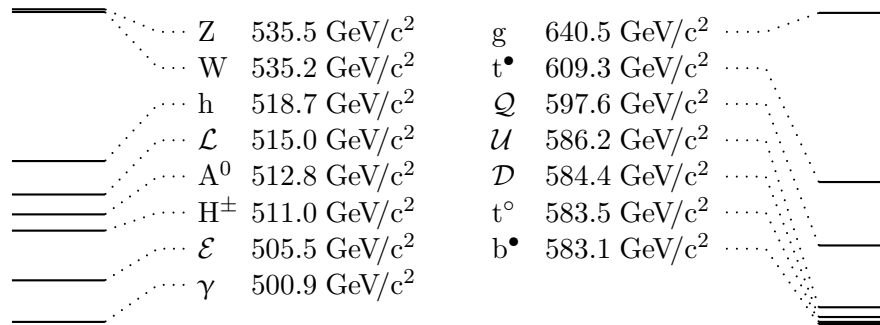
Z	535.5 GeV/c²	g	640.5 GeV/c²	
W	535.2 GeV/c²	t•	609.3 GeV/c²	
h	518.7 GeV/c²	$\mathcal{Q}$	597.6 GeV/c²	
$\mathcal{L}$	515.0 GeV/c²	$\mathcal{U}$	586.2 GeV/c²	
A⁰	512.8 GeV/c²	$\mathcal{D}$	584.4 GeV/c²	
H±	511.0 GeV/c²	t°	583.5 GeV/c²	
$\mathcal{E}$	505.5 GeV/c²	b•	583.1 GeV/c²	
γ	500.9 GeV/c²			

Figure 8.4: Masses of the first KK excitation level in the mUED model for $R^{-1} = 500$ GeV, $\Lambda R = 20$, and $m_\mathrm{h} = 120$ GeV. The spectrum is graphically indicated by the horizontal lines on the left and right sides; note that the two sides have different scales.

∘.) The corrections to the masses of the third generation doublet quarks t• and b•, third generation singlet quarks t° and b°, and Higgs bosons h⁰, H±, and A⁰ all depend on the mass of the Higgs boson, here taken to be 120 GeV, and any additional mass picked up by the Higgs at the orbifold fixed points, here taken as zero.

The color-charged particles, which comprise the right-hand, heavy side of the figure, receive the largest mass corrections. The KK gluon g_n is the heaviest particle at each KK level, picking up a mass correction on the order of 25% of m_n. The first KK excitation photon γ_1 is the lightest Kaluza-Klein particle (LKP).[*]

8.3.1 KK Particle Decay

When the mass corrections of [132] are taken into account the decays discussed above, which are forbidden with tree-level masses, are no longer forbidden. Figure 8.5 diagrams the possible decay chains of the first KK excitation level of the fermions and gauge bosons as described in [135].

While the decay channels of figure 8.5 are now open, the mass spectrum at each KK level is still highly degenerate. The standard-model particles emitted in the decay of KK₁ particles will therefore be rather soft. This phenomenology is discussed in greater detail in chapter nine.

8.3.2 LKP Stability

The conservation of KK parity makes the LKP stable and therefore an interesting dark matter candidate. The γ_1 can only interact with standard-model particles through the diagrams of figure 8.2, so Compton scattering in a collider detector is kinematically forbidden. The γ_1 will therefore escape the experiment unde-

---

[*]As pointed out in [134], the KK₁ charged higgs H±₁, KK₁ graviton G₁, or right-handed neutrino N₁ ≡ ν°₁, should they exist, could also be the LKP. However the decay from γ_1 to any of them would proceed so slowly that for the collider phenomenology of the following chapters the γ_1 can be considered stable; and it would also play a role in cosmology.
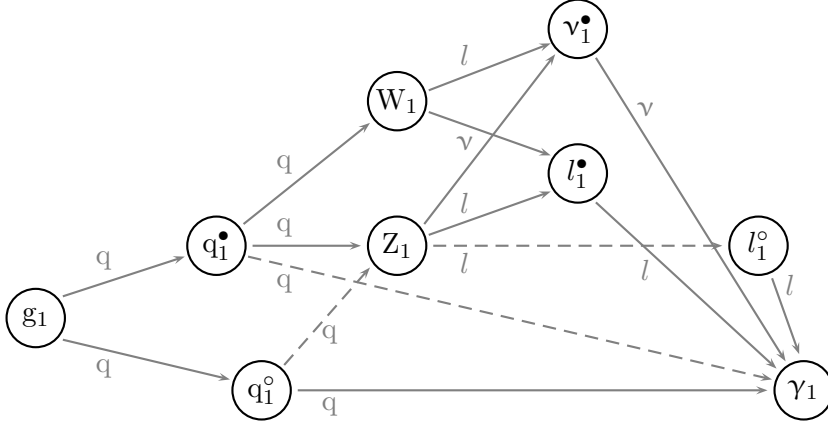
Figure 8.5: Diagram of possible decay chains in the first KK level of the fermions and gauge bosons. Standard-model particles emitted in the decays are shown in gray. Solid lines indicate dominant decay channels and dashed lines indicate rare decay channels, from [135]. Though not to scale, the masses of the particles decrease from left to right.

tected; the impact of this on collider searches for MUED is discussed in detail in chapter nine.

8.4 CONSTRAINTS ON MUED

The MUED model as described above contains only three unfixed parameters: R^{-1}, the inverse size of the single extra dimension and compactification scale, which has units of energy; ΛR, the number of KK excitations before the cutoff scale, Λ; and m_{h}, the mass of the standard-model Higgs boson. The coupling strengths of KK particles to each other or to standard-model particles are obtained by expanding out the 5D fields in the fashion of equations (8.9) and (8.10) for the 5D interaction Lagrangians like equation (8.14) and integrating out the y dimension. The coupling strengths are then those of the standard model up to a factor (for example, $\sqrt{2}$ for interactions between KK particles and each other).

The main role of $\{R^{-1}, \Lambda R, m_{\mathrm{h}}\}$ is in calculating the mass corrections discussed above. These corrections, as equations (8.18a)–(8.18d) show, depend logarithmically on ΛR and are not greatly changed over the range of Λ several times to a few tens of times larger than R^{-1}. This is a natural interval to focus on, since it means that the the cutoff scale for the effective theory is not too close to the compactification scale, allowing for interesting phenomenology with at least a few KK excitation levels; and that the model will be matched to a larger theory at energies only one or two orders of magnitude greater than the compactification scale.

Conservation of KK parity means that KK_1 excitations must be produced in pairs. This allows the limits on R^{-1} from direct collider searches to be as low as a couple hundred GeV. Though there is relative agreement that the best constraints on R^{-1} come from electroweak precision observables, there is no

great agreement on what those constraints are.

Calculating contributions to the anomalous value of the muon's magnetic moment is often used as a constraint on BSM physics, since it has been measured to a precision of 6×10^{-10} (see section 2.2.5). Appelquist and Dobrescu [136] calculated the contributions to a_μ from a single universal extra dimension and found

$$a_\mu^{\text{KK}} = -\frac{\pi\alpha}{32\sin^2 2\theta_{\text{W}}} \left(\frac{m_\mu}{R^{-1}}\right)^2 \approx -14 \times 10^{-10} \left(\frac{M_{\text{Z}}}{R^{-1}}\right)^2, \qquad (8.20)$$

which gives a lower limit on R^{-1} of a couple hundred GeV. Rizzo performed the same calculation [137] and found,

$$a_\mu^{\text{KK}} \approx -44 \times 10^{-10} \left(\frac{M_{\text{Z}}}{R^{-1}}\right)^2 \left[1 - 0.23\left(\frac{M_{\text{Z}}}{R^{-1}}\right)^2\right], \qquad (8.21)$$

which gives a limit on R^{-1} of about 250 GeV.[*]

Several calculations have been published of the lower limit on R^{-1} using the parameterizations of effects on the self-energies of the gauge bosons from new physics formulated in [138] and [139]. Appelquist et al. in [33] calculate a lower limit on R^{-1} of approximately 300 GeV with a light Higgs mass. This calculation was extended in [140] and the dependence of the lower limit on m_{h} was calculated; the absolute lower limit remained approximately 300 GeV but only at a heavy Higgs mass (greater than 500 GeV). The lower limit on R^{-1} was seen to decrease with increasing m_{h}.

Flacke et al. contradict this in [141], finding the lower limit on R^{-1} to increase with increasing m_{h} and to be much larger than the previously mentioned calculations. Figure 8.6 shows the results from [141] at the 99% confidence level alongside those from Gogoladze and Macesanu [142], which reconfirm the m_{h} dependancy of [140]. The last calculation sets the mass of the top quark to be $m_{\text{t}} = 173\,\text{GeV/c}^2$. Though ΛR does not enter explicitly into the calculation, it is taken implicitly to be ten in cutting off any Riemann ζ functions after ten KK excitation levels. They calculate a lower limit on R^{-1} of less than 300 GeV at heavy m_{h}—the upper limits on m_{h} are considerably relaxed by the existence of KK states. The lower limit on R^{-1} is also greatly relaxed for decreasing values of m_{t}.

These limits and some further ones are listed in table 8.1. The general lower limit on R^{-1} is in the several hundred GeV range. This is low enough to accommodate the LKP as a dark matter candidate [147]. Cosmology considerations lead to an upper bound on the compactification scale: Assuming the γ_1 is the LKP and explains cold dark matter, the observations of the Wilkinson Microwave Anisotropy Probe constrain the compactification scale to be less than a few TeV [147–149]. These constraints apply only to light Higgs boson masses (less than approximately 300 GeV). At larger Higgs masses, there is the possibility (at large R^{-1}) that the LKP is a charged Higgs boson; this is disfavored

---

[*]The 250-GeV limit is stronger than that quoted by Rizzo, who writing in 2001 calculated with an older value for the uncertainty on a_μ.
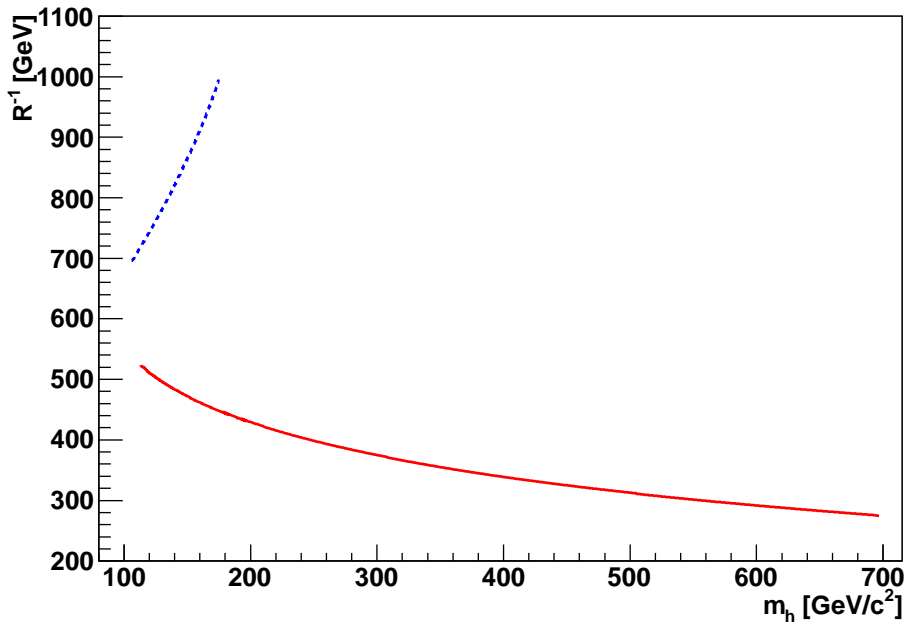
Figure 8.6: 99%-confidence lower limit on R^{-1} as a function of the Higgs mass m_{h} from [141] (dashed blue) and [142] (solid red).

by cosmologists [148]. The lightness requirement on m_{h} translates to a lower bound in cosmology models on R^{-1} of approximately 400 GeV.

8.5 LHC PHENOMENOLOGY

The lower limits on R^{-1} already lie above the reach of LEP II and the Tevatron [135], and no analyses pertaining to UED have yet emerged from the LHC experiments. However, the phenomenology of the model at the LHC has been much discussed. Three main discovery channels have been looked into, the single and pair production of KK$_2$ states, the pair production of KK$_1$ gauge bosons, and the production of a q$_1$ and a KK$_1$ gauge boson. The first two are discussed in detail in [135, 150–153], where it is shown that the two have similar signals, namely the production of multileptonic final states with missing transverse momentum.

The production of KK$_2$ states, since they decay either to KK$_1$ states or in ways that mimic the decay of KK$_1$ states, would be perceived as enhancements of the cross sections for the production of KK$_1$ states. It has been observed that the mass spectrum of UED can closely mimic that of the minimal supersymmetric standard model [35, 36, 154]. Identifying the production of the second KK excitation level would be a clear signal of UED, verifying the presence of the KK towers, since no such states exist in the MSSM.

The last channel listed above is particularly interesting in terms of the possible confusion between UED and SUSY at a collider. This was investigated

Reference	Lower Limit [GeV]	Method
[33]	300	Z-pole EWPO
[140]	250	Z-pole EWPO
[141]	700	Z-pole EWPO
[142]	300	Z-pole EWPO
[136]	300	a_μ
[137]	350	a_μ
[143]	280	FCNC
[144, 145]	200	FCNC
[146]	300	FCNC

Table 8.1: Approximate lower limits on R^{-1} and the methods used for their calculation; EWPO stands for electroweak precision observables, FCNC for flavor-changing neutral current. Values in the table are directly quoted from the references, and in some instances are slightly different than those mentioned in the text, which use updated values from [25].
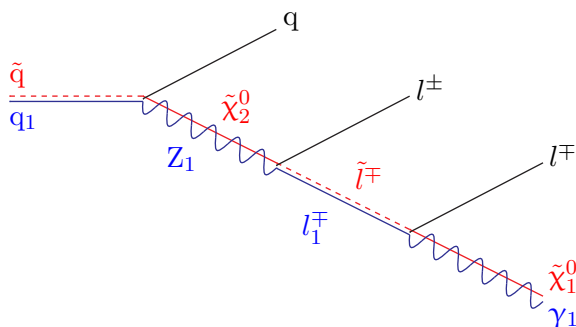
Figure 8.7: Decay channel of a SUSY squark (red) and a KK$_1$ quark (blue), showing the emitted SM particles common to both decays (black).

in [151, 154] using the methods developed by Barr in [155]. The authors looked at the production of KK$_1$ quarks and SUSY squarks ($\tilde{q}$) and their subsequent decays, which have similar forms (figure 8.7). Both new particles decay into a quark jet, a pair of opposite-sign same-generation leptons, and a noninteracting neutral particle, which results in missing energy in the detected final state.

However the spins of the initial and intermediary states of the two models differ greatly: In SUSY the decay chain proceeds from scalar ($\tilde{q}$) to fermion (the second-lightest neutralino $\tilde{\chi}_2^0$) to scalar (a slepton $\tilde{l}$) to fermion (the lightest neutralino $\tilde{\chi}_1^0$). Whereas in UED the KK$_1$ states have the same spins as their SM counterparts[*] and the decay proceeds from fermion to vector to fermion to vector. By measuring the angles between the jet and fermions, one could discover the spin structure of the model. But this requires that we know which lepton is emitted first in the decay chain. Since all the decays are prompt, this is

---

[*]Though the l_1 is a vector particle, it is produced in a $\mathcal{P}_y$ eigenstate and therefore has chirality.
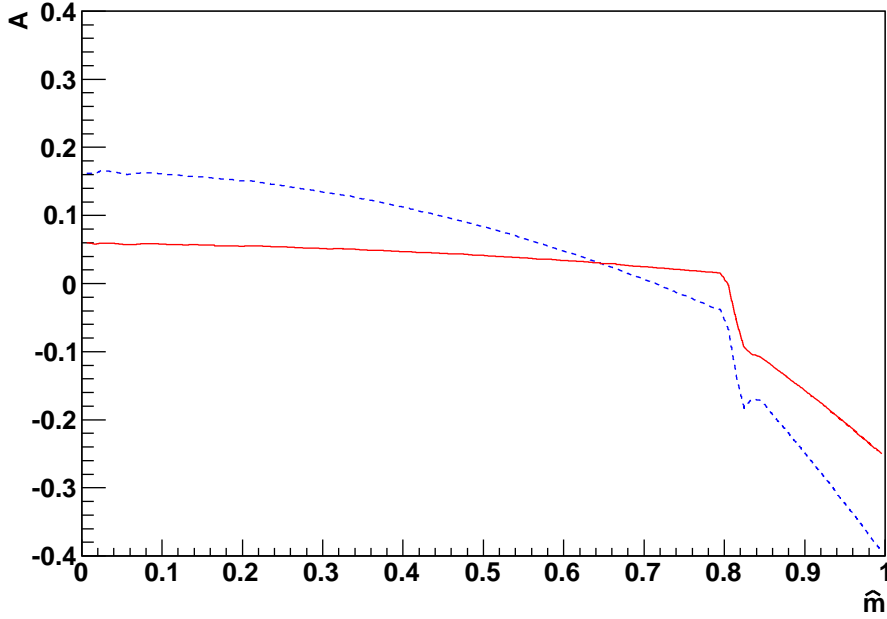
Figure 8.8: Barr's charge asymmetry variable [155] as a function of normalized invariant jet-lepton mass for a UED-like decay (solid red) and a SUSY-like decay (dashed blue) for a UED-like mass spectrum, from [154].

not possible. However, Barr discovered that knowledge of the spin structure can be obtained by comparing $\mathrm{d}\sigma/\mathrm{d}m_{\mathrm{jl}+}$ and $\mathrm{d}\sigma/\mathrm{d}m_{\mathrm{jl}-}$, where m_{jl} is the invariant mass of the jet-lepton system. He defined the charge asymmetry,

$$A = \frac{\mathrm{d}\sigma/\mathrm{d}m_{\mathrm{jl}+} - \mathrm{d}\sigma/\mathrm{d}m_{\mathrm{jl}-}}{\mathrm{d}\sigma/\mathrm{d}m_{\mathrm{jl}+} + \mathrm{d}\sigma/\mathrm{d}m_{\mathrm{jl}-}}, \tag{8.22}$$

which Smillie and Webber used to compare UED and SUSY. Figure 8.8 shows their results for a UED-like mass spectrum for UED and SUSY as a function of normalized jet-lepton invariant mass, $\hat{m} = m_{\mathrm{jl}}/m_{\mathrm{jl}}^{\mathrm{max}}$. Clearly the two theories have different shapes for the dependency of A on $\hat{m}$. However, in simulations with the HERWIG event generator [156] with simulated detector effects, the differences were not pronounced [154], and it has not yet been investigated whether the two shapes could be discerned at the LHC with SM backgrounds accounted for.

UED at a Muon Collider

In the previous chapter, we discussed the phenomenology of UED at a hadron collider, at which discovery is accomplished in much the same way as for supersymmetry. However, discerning between the two theories at such a collider may be very difficult. At a lepton collider discovery and discernment of the two theories could be accomplished more easily. We present here the phenomenology of UED at a 3-TeV-center-of-mass muon collider and briefly compare it to that of SUSY.

The UED discovery channel we investigate is the pair production of KK$_1$ muons. The pair production of KK$_1$ electrons and muons at an e$^+$e$^-$ linear collider was discussed in [36] and is very similar. Our discussion proceeds along the same lines, but attempts to include SM background processes in a more comprehensive way and to reduce the impact of data-selection cuts on the analysis.

For all following discussion, we take 3 TeV as the center-of-mass energy, and an energy spread on the muon beams of $\Delta E/E = 0.16\%$, a typical value quoted in the muon collider studies discussed in chapter two. We will pay particularly close attention to the dependence of our results on the angular acceptance of a muon-collider detector. As was discussed in section 2.4.5, shielding against background radiation at a muon collider may greatly limit the angular acceptance of its detectors. A goal of our analysis is to quantify the effects of such limitations on the ability to measure the compactification scale of UED.

9.1 KK$_1$-MUON-PAIR PRODUCTION

Figure 9.1 shows the Feynman diagrams for tree-level pair production of μ_1. In total there are twelve distinct diagrams. The $n_{\rm KK}$-conserving diagrams are s-channel production of a $\mu_1^\bullet$ or μ_1° pair through a γ or Z^0 (four diagrams); t-channel production of a $\mu_1^\bullet$ pair by exchange of a γ_1 or Z$_1^0$ (two diagrams); and t-channel production of a μ_1° pair or $\mu_1^{\bullet\pm}\mu_1^{\circ\mp}$ by exchange of a γ_1 (three diagrams). The $n_{\rm KK}$-violating (but $\mathcal{P}_{\rm KK}$-conserving) diagrams are s-channel production of a $\mu_1^\bullet$ pair through a γ_2 or Z$_2^0$ (two diagrams), or μ_1° pair through a γ_2 (one diagram).

The μ_1's decay promptly to standard-model muons and γ_1's. The γ_1's will be undetectable; so the characteristic signal of μ_1-pair production is a dimuonic final state with missing energy,

$$\mu^-\mu^+ \rightarrow \mu_1^-\mu_1^+ \rightarrow \mu^-\mu^+\gamma_1\gamma_1 = \mu^-\mu^+ + \not{E}. \qquad (9.1)$$

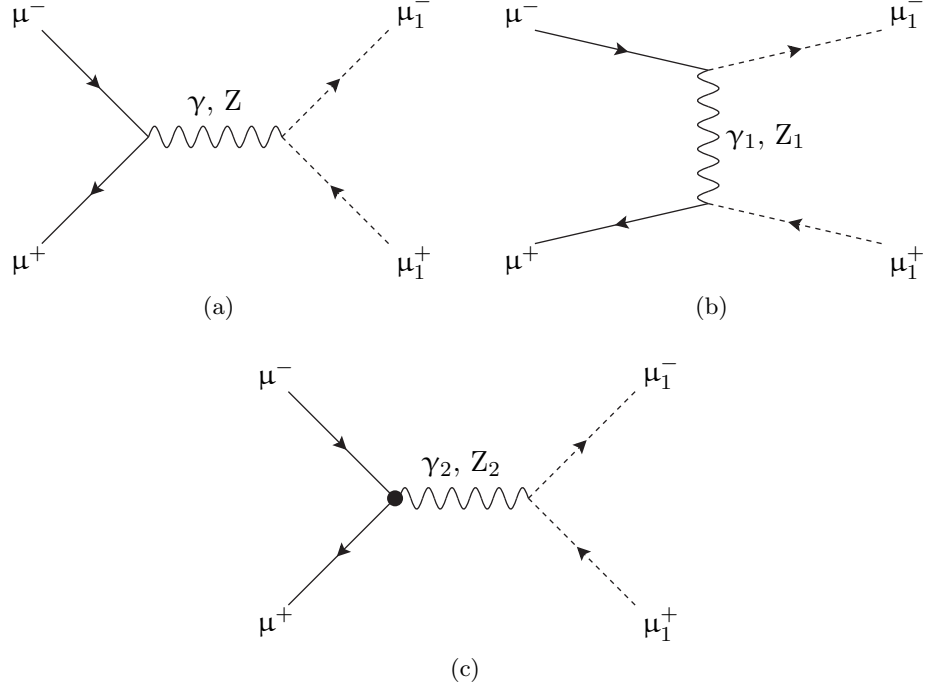Figure 9.1: μ_1-pair-production diagrams: n_{KK}-conserving (a) and (b), and n_{KK}-violating (c).

The lab-frame energy of the μ from the two-body decay of the μ_1, is

$$E_\mu = \frac{1}{2} E_{\mu_1} \left(\frac{\Delta m_1^2 + m_\mu^2}{m_{\mu_1}^2} \right) (1 + \beta \cos \theta), \tag{9.2}$$

where $\Delta m_1^2 \equiv m_{\mu_1}^2 - m_{\gamma_1}^2$ is the squared-mass difference between the KK-level-one muon and photon, E_{μ_1} and β are the energy and velocity of the μ_1 in the lab frame, and θ is the angle between the μ_1 lab-frame momentum direction and the μ in the μ_1 rest frame. The energy of the SM muons in the final state is limited by $\Delta m_1^2/m_{\mu_1}^2$; figure 9.2 shows that the squared-mass difference is never larger than a few percent. The final-state SM muons are therefore very soft. Figure 9.3 shows the maximum energy for a final-state muon ($\cos \theta = 1$, $\mu_1 = \mu_1^\bullet$) for $E_{\mu_1} = E_{\text{beam}} = 1.5$ TeV. The maximum energy is achieved for R^{-1} between 500 GeV and 600 GeV. Above this compactification scale, the squared-mass difference increases very slowly with R^{-1}, but since E_{μ_1} is fixed at E_{beam} while $m_{\mu_1^\bullet}$ continues to increase, β rapidly decreases; this causes the maximum final-state energy to drop.

The transverse energy of the dimuonic system is at its maximum when $\cos \theta_{\mu^-} = -\cos \theta_{\mu^+} = \pm 1$, with the θs as defined above, and therefore also related to the squared-mass difference.

In summary, the characteristic signal of μ_1-pair production at center-of-mass energy 3 TeV is a final state consisting of only two muons, with individual energies less than 80 GeV and transverse event energy of less than 80 GeV. The
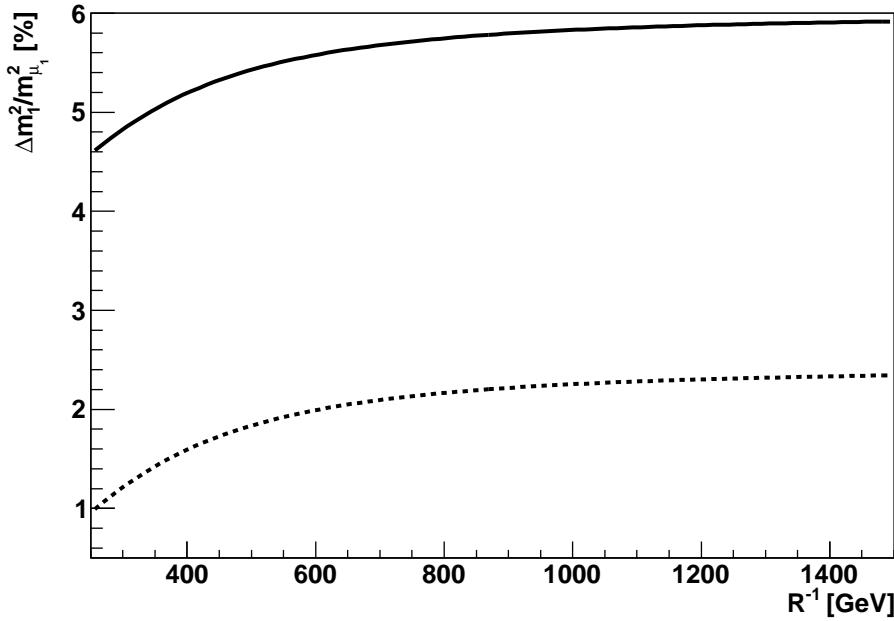
Figure 9.2: Squared-mass difference between μ_1 and γ_1 as a function of R^{-1} for $\mu_1^\bullet$ (solid) and μ_1° (dashed) with $\Lambda R = 20$.

SM processes that can mimic this signal are the production of a muon pair and n neutrino pairs

$$\mu^-\mu^+ \to \mu^-\mu^+ + (n)\nu\bar{\nu} = \mu^-\mu^+ + \not{E}. \tag{9.3}$$

We calculate the cross section from the diagrams in figure 9.1 using the CompHEP event generator [157] modified to accommodate the energy spread characteristics of the input muon beams; we use the model implementation of [158] to simulate the mUED spectrum and interactions. Figure 9.4 shows the μ_1-pair production cross section σ_{UED} for R^{-1} between 250 GeV and 1475 GeV. The cross section is of order pb at small compactification scales and decreases rapidly to 10s of fb at $R^{-1} \gtrsim 1$ TeV. The peak at large R^{-1} in figure 9.4 is due to the resonant production of Z_2^0 at $R^{-1} \approx 1434$ GeV, at which $m_{Z_2^0} = \sqrt{s}$. Above this compactification scale, the pair-production cross section falls rapidly to zero as the μ_1 mass rises above $\sqrt{s}/2$.

Figure 9.5 shows the differential cross section as a function of outgoing muon energy at a representative compactification scale $R^{-1} = 850$ GeV; the two energy plateaus correspond to the two-body decays of the $\mu_1^\bullet$ and μ_1° states; with their minimum and maximum energies (highlighted in the figure) given by equation (9.2) with $\cos\theta = \pm 1$. Figure 9.6 shows the angular distribution of the outgoing muons with respect to the incoming muons for the same value of R^{-1}; the distribution is heavily skewed towards small angles, showing the dominance of the forward-scattering t-channel diagram of figure 9.1b in the cross section calculation.
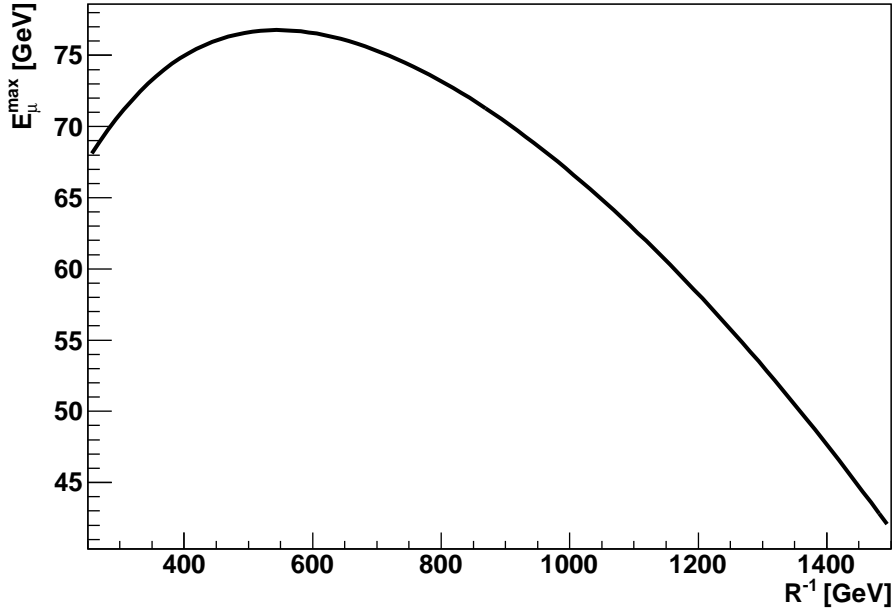
Figure 9.3: Maximum final-state muon energy in $\mu^+\mu^- \to \mu^+\mu^- + \not{E}$ via μ_1-pair production as a function of R^{-1} with $\Lambda R = 20$ and $E_{\text{beam}} = 1.5$ TeV.

9.2 STANDARD MODEL SOFT MUON-PAIR PRODUCTION

As we noted above, the standard-model processes that have final states that mimic that of μ_1 production are those in which neutrinos carry away large fractions of the interaction energy without being detected. The number of tree-level Feynman diagrams matching equation (9.3) with $n = 1$ is 144. When $n = 2$, the number jumps to over three thousand. Using the CompHEP event generator to calculate the total cross section from all $n{\leq}2$ diagrams is not possible. We therefore first investigate which diagrams are dominant for the production of a muon pair with individual energies $E_\pm \leq 80$ GeV and combined transverse energy $E_{\text{T}} \leq 80$ GeV.

We begin with the $n{=}1$ diagrams. Diagrams for $n = 2$ can be generated by modifying $n{=}1$ diagrams for the production of a second neutrino pair. Since the cross section for these processes will be a factor of the coupling constant smaller than their $n{=}1$ parents, we expect only the most dominant $n{=}1$ diagrams to yield significantly influential $n{=}2$ diagrams. Therefore we also identify the $n{=}1$ diagrams which are dominant for the production of muon pairs without the energy requirements listed above.

The details for all $n{=}1$ diagrams is presented in appendix A. We present here the dominant diagrams. Figure 9.7 shows the Feynman diagrams wherein the muon pair is produced from a γ or Z^0; figure 9.8 shows those diagrams wherein one or both muons are produced by a W. By imposing the requirement that the outgoing muons have angles with respect to the beam axis of greater
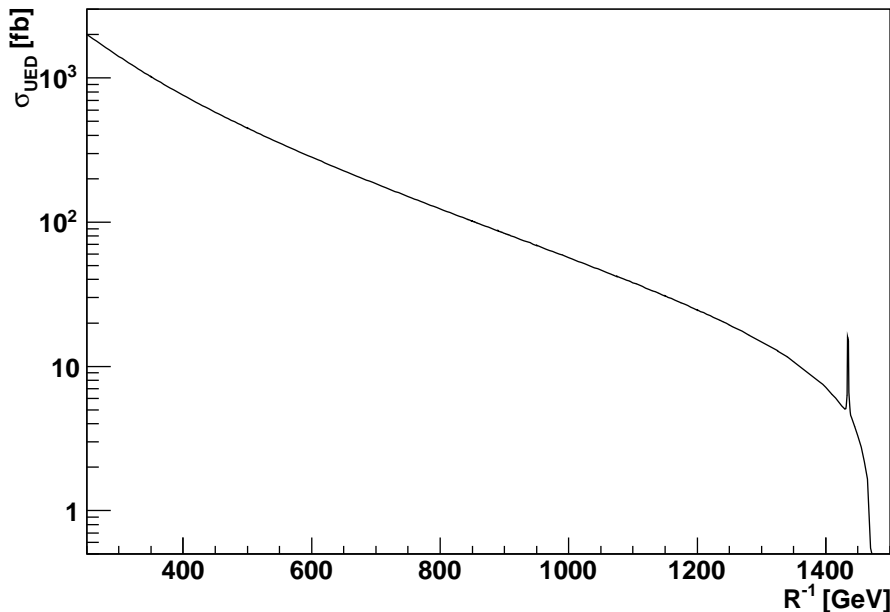
Figure 9.4: Cross section for μ_1-pair production as a function of R^{-1}, with $\Lambda R = 20$.

than $4°$, the contributions from the diagrams of figure 9.8 are made negligible. This cut will have no impact on the analysis of the UED model, since $4°$ is the minimum angle needed to just exit the beam pipe and enter the collider detector, regardless of the shielding in place (see section 2.4.5).

As well, the contributions from the diagrams in figure 9.7 with the neutral boson replaced by a Higgs boson (as shown in appendix A) can also be neglected. This simplifies the calculation for CompHEP, and removes m_h as a free parameter of the SM background generation. (Since the Higgs boson is also absent from the diagrams in figure 9.1 and from the mass corrections of the μ_1 and γ_1, we can completely eliminate m_h as a parameter for our analysis.)

The resulting total SM cross section, with the cuts detailed above, is 47.3 fb. The cross section for the state with only one neutrino pair is thus already competative with the UED cross section at large compactification scales. However, the invariant mass distribution of the SM-produced soft muons peaks sharply at zero and M_Z (figure 9.9[*]).

The diagrams of figures 9.7, 9.8 (except 9.8d), and 9.10 are the only diagrams of appendix A that have individual uncut cross sections of order pb or larger. We modified these diagrams to produce an additional ν pair in the final state and again investigated which diagrams contribute dominantly. The full calculation is presented in appendix B. Only four classes of such diagrams are expected

---

[*]One more cut will be motivated below, requiring the invariant mass be greater than 5 GeV. The figure reflects this cut, but the total cross section quoted here is without the cut.
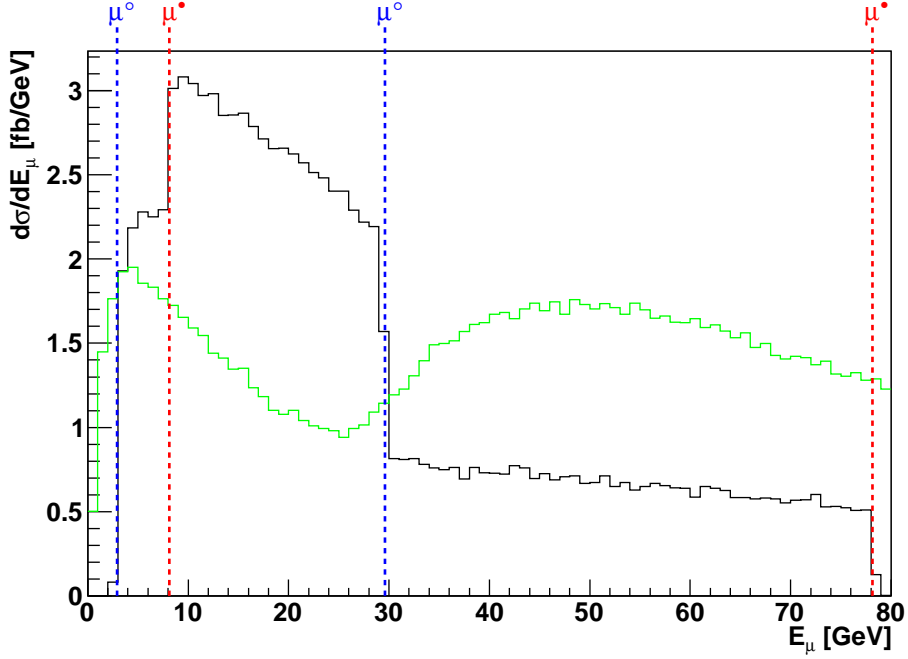
Figure 9.5: Differential cross section at $R^{-1} = 850$ GeV and $\Lambda R = 20$ for the production of a soft muon pair through μ_1-pair production (black) as a function of outgoing muon energy. The maximum and mininum energies of the SM muon from the decay of the $\mu_1^\bullet$ and μ_1° are highlighted. The green histogram shows the cross section for the production of soft muons in the SM scaled up by a factor of ten for comparison.

to contribute at or above the fb level to the cross section for soft muon-pair production (figures B.5 and B.3). Two of these are obtained by modifying figure 9.8a and are made negligible by the requirement that the muon angles be greater than $4°$.

The two remaining diagrams will contribute at the order of 100 fb. This would dominate over the UED processes over a large range of interest of the compactification scale. However, in these six-particle (6p) final states, the muon pair is dominantly produced by a photon and so the cross section sharply peaks at zero invariant dimuonic mass; this is in contrast to the UED cross section, which falls off at zero invariant mass. By imposing the requirement on the final state that the dimuonic mass be above 5 GeV, the 6p final states can be neglected.

The cross section for the production of a soft muon pair with all the requirements—$E_\mu, T_{\mu\mu} \leq 80$ GeV, $\cos\theta_\mu \geq \cos 4°$, and $M_{\mu\mu} \geq 5$ GeV—is $\sigma_{\text{SM}} = 11.70$ fb. The SM 4p cross section is reduced by 75% by the invariant-mass requirement; in contrast, σ_{UED} is reduced by at most a few percent (the distribution at low invariant mass changes with the compactification scale). Figure 9.11 shows the enhancement of the cross section in the UED model compared to the SM alone as a function of the compactification scale.
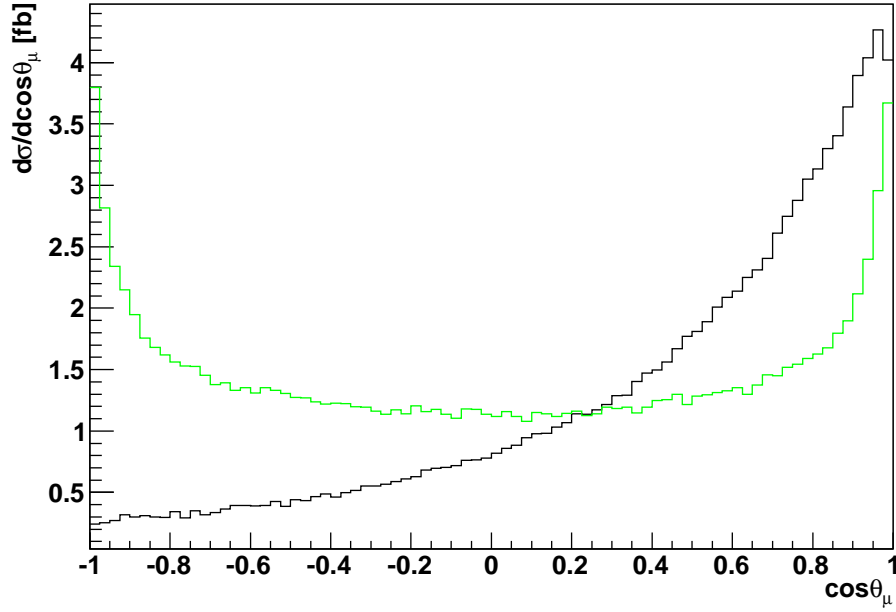
Figure 9.6: Differential cross section at $R^{-1} = 850$ GeV and $\Lambda R = 20$ for the production of a soft muon pair through μ_1-pair production (black) as a function of the angle of the outgoing muon with respect to the incoming muon. The green histogram shows the cross section for the production of soft muons in the SM scaled up by a factor of ten for comparison.

9.2.1 *mUED vs MSSM*

The shapes of the differential cross sections as a function of outgoing muon energy in the mUED model and the MSSM will be the same, since both are governed by two body decay kinematics. The SUSY counterparts to the $\mu_1^\bullet$ and μ_1° states are the $\tilde{\mu}_L$ and $\tilde{\mu}_R$. Since in comparing the two models, we assume that they have the same mass spectrum, the differential cross section shapes are exactly the same. However, the overall cross section for soft muon-pair production in the MSSM is expected to be significantly smaller than in mUED [35, 36, 154].

Battaglia et al. in [36] looked at the difference in angular distribution of the ougoing leptons in mUED and the MSSM. Figure 9.12 shows their results for $e^+e^- \rightarrow e^+e^- + \not{E}$. The angular distributions are the same as for the processes $\mu^+\mu^- \rightarrow \mu^+\mu^- + \not{E}$, and show a subtle, but detectable, difference between mUED and the MSSM.

9.3 MUED AT μC ANALYSIS

The enhancement of the production of soft muon pairs in the UED model is significantly large at compactification scales up to and even above 1 TeV. At
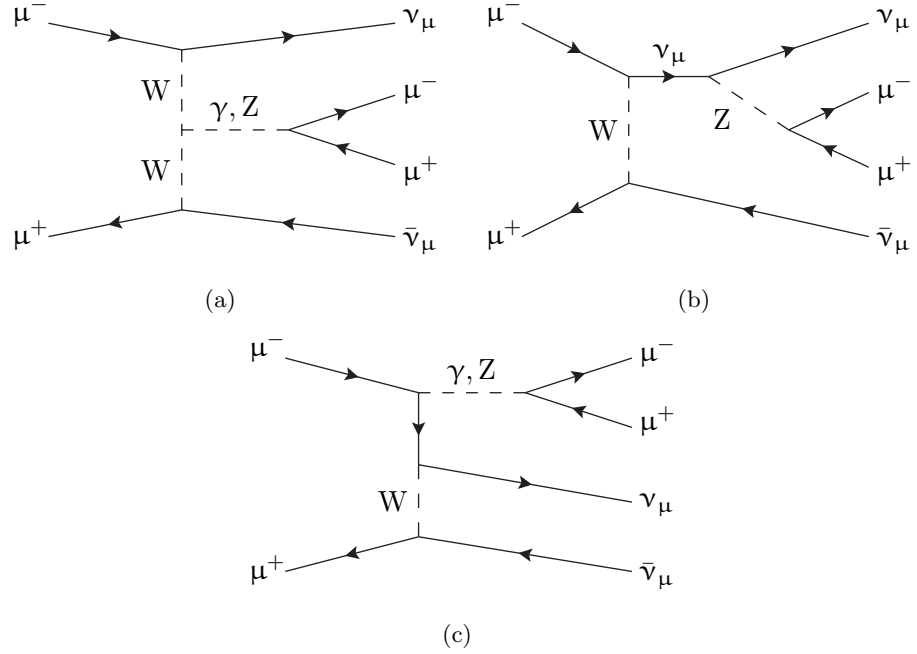
Figure 9.7: Feynman diagrams for the production of a soft muon pair through a photon or Z^0 accompanied by a neutrino pair in the SM.

these scales, discovery can be made through a counting of the total event rate with the above final-state requirements. We investigate the achievable statistical uncertainty on the measurement of the compactification scale as a function of the scale and the angle of the detector shielding.

To develop the analysis technique we start by looking at the total cross section $\sigma(R^{-1})$ for the production of a soft muon pair with $\cos\theta_{\mu^{\pm}} \geq \cos\theta_c$, where θ_c is the shielding angle, and the cross section includes the contributions from both the SM and UED (with compactification scale R^{-1}). Using Bayes' theorem, given a data sample D—the generation of which is discussed in section 9.3.1—the probability that the compactification scale is R^{-1} is

$$P(R^{-1}|D) = \frac{P_0(R^{-1})P(D|R^{-1})}{P_0(\text{SM})P(D|\text{SM}) + \int P_0(R^{-1'})P(D|R^{-1'})\mathrm{d}R^{-1'}}, \quad (9.4)$$

where $P_0(M)$ is the prior belief in model M. We take the prior belief to be democratically divided between the two models, the SM and UED,

$$P_0(\text{SM}) = \int P_0(R^{-1})\mathrm{d}R^{-1} = \frac{1}{2}, \quad (9.5)$$

and to be a constant function of R^{-1}. The denominator in equation (9.4) is independent of the particular value of R^{-1} in the numerator, and we can focus our attention on the the likelihood $L(R^{-1}|D) \propto P_0(R^{-1})P(D|R^{-1})$. In particular, we will look at how the likelihood changes in a small region around R^{-1}.
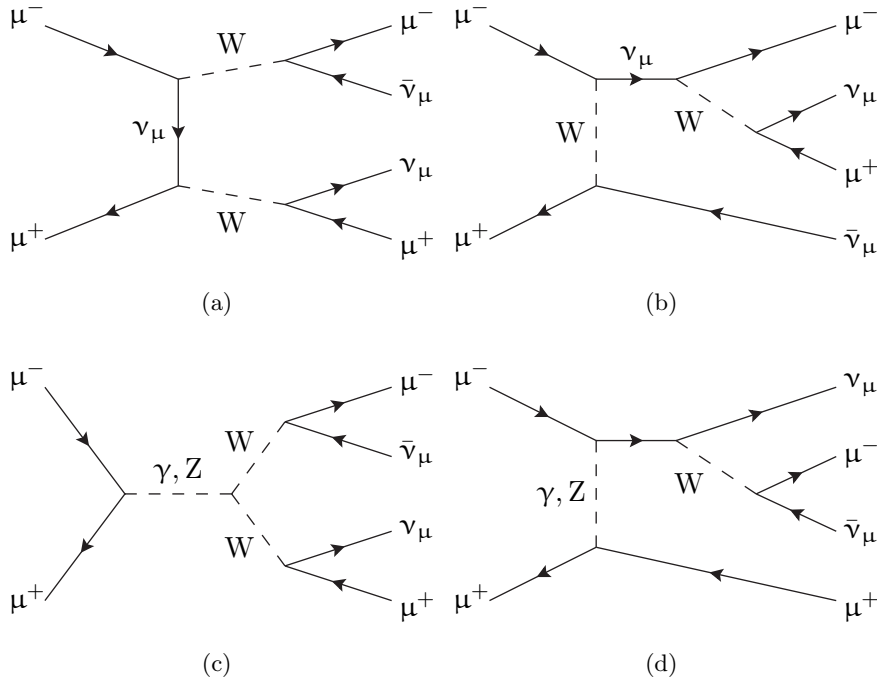
Figure 9.8: Feynman diagrams for the production of a soft muon pair through a W accompanied by a neutrino pair in the SM.

Working with the log of the likelihood, and dropping D since it is the same for the two likelihoods being compared, we have

$$
\begin{aligned}
\Delta \ln L(R^{-1}) &\equiv \ln L(R^{-1} + r^{-1}) - \ln L(R^{-1}) \\
&= \ln P(R^{-1} + r^{-1}) - \ln P(R^{-1}).
\end{aligned}
\tag{9.6}
$$

Taking the number of events n measured in D to be distributed according to Poisson statistics, we have for the change in likelihood

$$
\Delta \ln L(R^{-1}) = n \ln \left(1 + \frac{\Delta \nu}{\nu} \right) - \Delta \nu
\tag{9.7}
$$

where $\nu = \mathscr{L}\sigma(R^{-1})$ is the expected number of events given the cross section at R^{-1} and a specified integrated luminosity $\mathscr{L}$ for D; $\Delta \nu \equiv \mathscr{L}\sigma(R^{-1} + r^{-1}) - \nu$. In terms of the cross section, we have

$$
\Delta \ln L = n \ln \left(1 + \frac{\Delta \sigma}{\sigma} \right) - \mathscr{L}\Delta \sigma.
\tag{9.8}
$$

If we evaluate the change in log likelihood in a very local neighborhood of R^{-1}, we can require $|\Delta \sigma / \sigma| < 1$ and can Taylor expand the logarithm,

$$
\Delta \ln L = -n \sum_{j=1}^{\infty} \frac{(-1)^j}{j} \left(\frac{\Delta \sigma}{\sigma} \right)^j - \mathscr{L}\Delta \sigma.
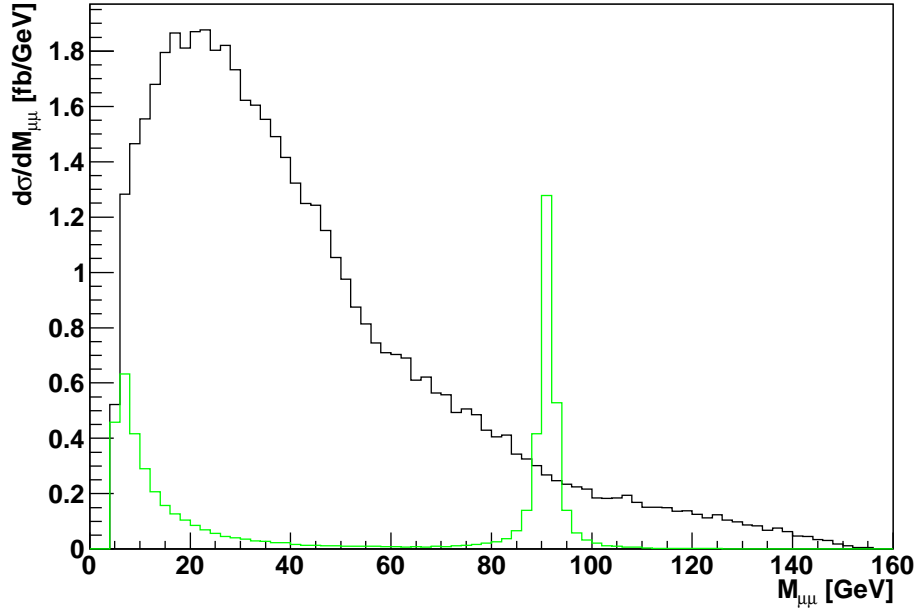\tag{9.9}
$$

Figure 9.9: The differential cross section at $R^{-1} = 850$ GeV and $\Lambda R = 20$ for the production of a soft muon pair through μ_1-pair production (black) as a function of the invariant mass of the outgoing muons. The green histogram shows the cross section for the production of soft muons in the SM.
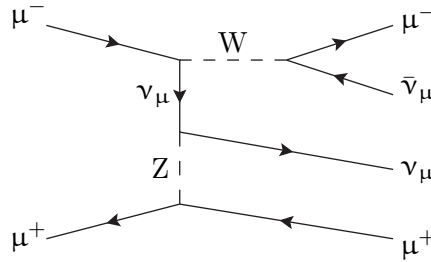

Figure 9.10: Dominant diagram for the production of a muon pair and a neutrino pair in the SM.

Taylor expanding $\Delta\sigma$ gives

$$\Delta \ln L = -n \sum_{j=1}^{\infty} \frac{(-1)^j}{j} \left(\sum_{k=1}^{\infty} \frac{\sigma^{(k)}}{\sigma} \frac{r^{-k}}{k!} \right)^j - \nu \sum_{k=1}^{\infty} \frac{\sigma^{(k)}}{\sigma} \frac{r^{-k}}{k!}, \qquad (9.10)$$

where $\sigma^{(j)}$ is the jth derivative of σ (with respect to the compactification scale). Truncating the expansions at first-order derivatives and at the second-order in
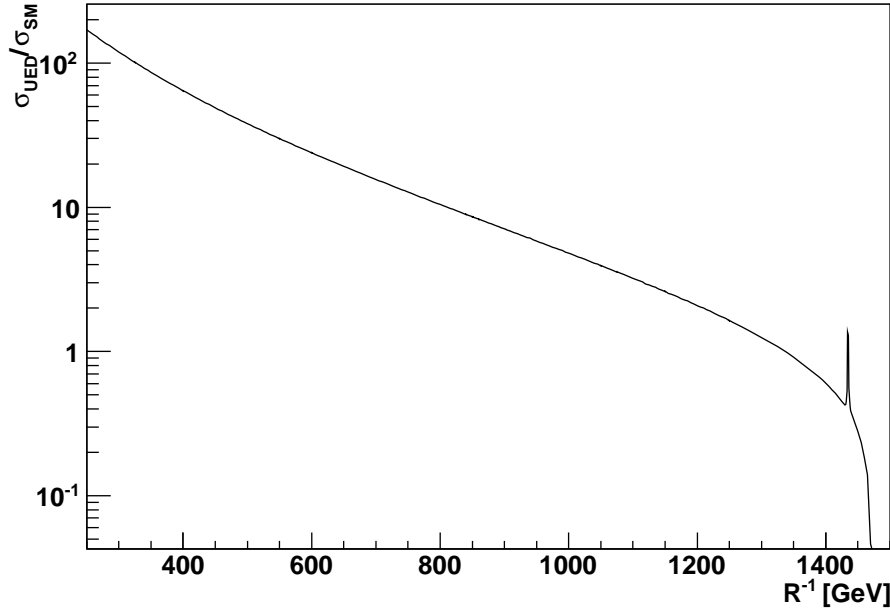
Figure 9.11: Enhancement of the cross section for soft muon-pair production in the UED model as a function of R^{-1}. All final-state requirements discussed in the text have been applied.

r^{-1}, we arrive at

$$
\begin{aligned}
\Delta \ln L &= -\frac{1}{2} n \left(\frac{\sigma'}{\sigma} \right)^2 r^{-2} + (n - \nu) \left(\frac{\sigma'}{\sigma} \right) r^{-1} \\
&= -\frac{1}{2} \beta \left(r^{-1} - \frac{\alpha}{\beta} \right) + \frac{\alpha^2}{2\beta},
\end{aligned}
\tag{9.11}
$$

with

$$
\alpha = (n - \nu) \frac{\sigma'}{\sigma}, \qquad \beta = n \left(\frac{\sigma'}{\sigma} \right)^2.
\tag{9.12}
$$

Removing the pedestal $\alpha^2/2\beta$, this is a gaussian-distributed likelihood

$$
\Delta \ln L = -\frac{1}{2} \beta (r^{-1} - \mu), \quad \mu = \left(1 - \frac{\nu}{n} \right) \frac{\sigma}{\sigma'},
\tag{9.13}
$$

with variance $\beta^{-1} = \sigma^2/n\sigma'^2$. For large expected event rates, $n \approx \nu$ and the N-standard-deviation credibility width around R^{-1} is

$$
\Delta_N R^{-1} = \frac{2N}{\sqrt{n}} \frac{\sigma(R^{-1})}{\sigma'(R^{-1})} = \frac{2N}{\sigma'(R^{-1})} \sqrt{\frac{\sigma(R^{-1})}{\mathscr{L}}},
\tag{9.14}
$$

which is shown in figure 9.13 for $N = 3$ (99% credibility), $\mathscr{L} = 100$ fb^{-1}, and $\theta_c = 4°$.[*] The uncertainty has the expected $1/\sqrt{n}$ dependence on the number of

---

[*]We choose θ_c just for illustration. To determine the effect of the shielding angle on the uncertainty on R^{-1}, we will use the binned analysis described below.
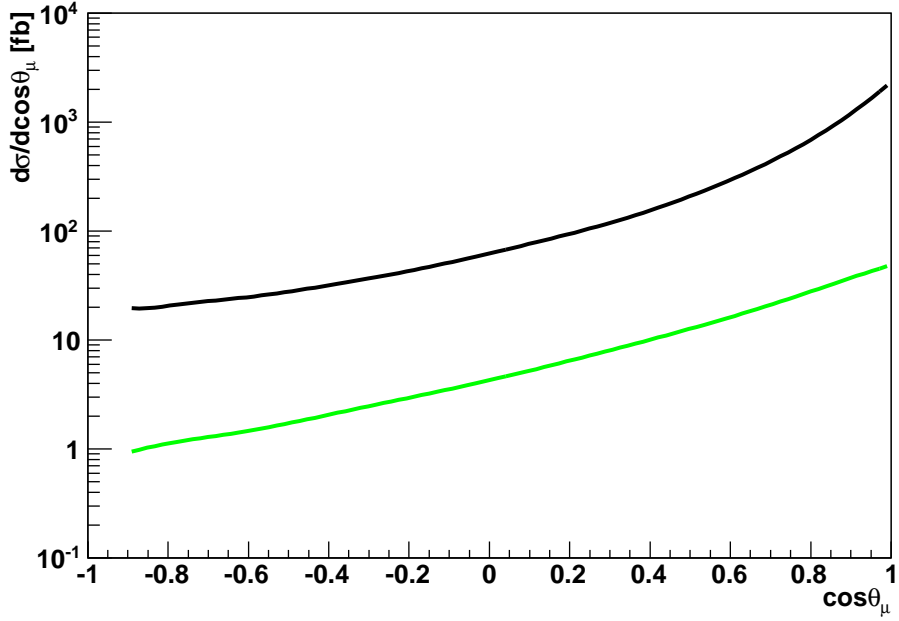
Figure 9.12: Differential cross section for soft electron-pair production in UED (black) and the MSSM (green) as a function of outgoing muon angle, from [36].

events. It also has a stronger dependence on the change of the cross section with R^{-1} than on the value of the cross section. The dependence on $\sqrt{\sigma}$ means that a decrease of σ_{UED} relative to σ_{SM} will have a stronger impact on the uncertainty on the higher values of R^{-1}, at which $\sigma_{\mathrm{UED}} \lesssim \sigma_{\mathrm{SM}}$. Thus a change in the estimation of the SM background more greatly effects the precision at large R^{-1}.

We can improve upon this result by performing the same calculation across the bins of a binned phase space of the outgoing muons. This is achieved by modifying the α and β terms of equation (9.11),

$$ \alpha = \sum_i (n_i - \nu_i) \frac{\sigma'_i}{\sigma_i}, \qquad \beta = \sum_i n_i \left(\frac{\sigma'_i}{\sigma_i} \right)^2, \qquad (9.15) $$

where the σ_i, σ'_i, n_i, and ν_i are the values for bin i.

As figures 9.5 and 9.6 show, the energy and angular distributions of the final-state muons in the SM and UED are very different; as well, equation (9.2) shows that the energy distribution will depend greatly on m_{μ_1} and m_{γ_1}, both of which depend greatly on the compactification scale. The 4D space $(E_{\mu^-}, \theta_{\mu^-}, E_{\mu^+}, \theta_{\mu^+})$ is therefore a good choice for the binned analysis. The summations in equation (9.15) can be performed with a cut on $\theta_{\mu^\pm}$ allowing for a calculation of the uncertainty on R^{-1} as a function of shielding angle.
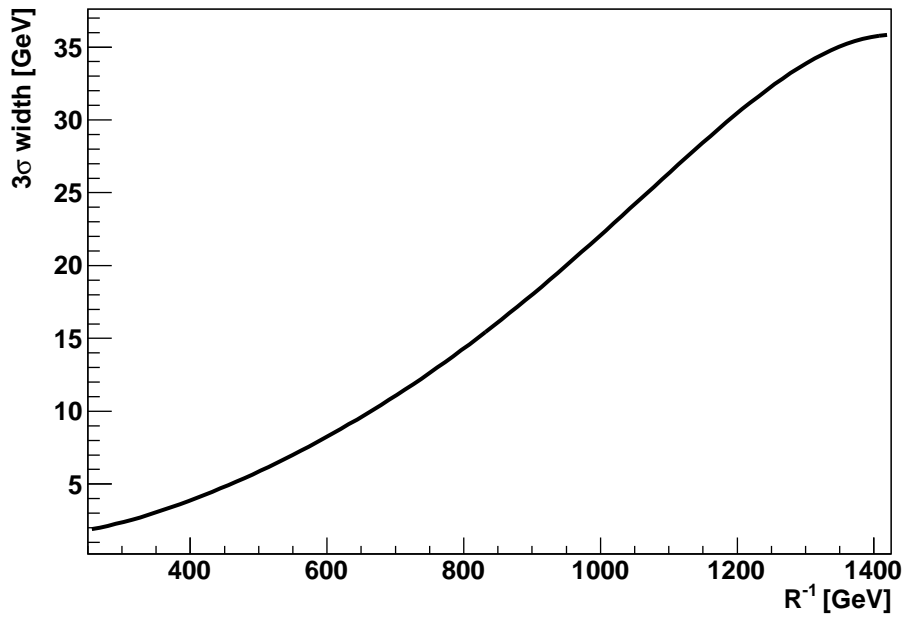
Figure 9.13: 3σ-credibility-interval width for the measurement of R^{-1} with an integrated luminosity of 100 fb^{-1} and $\theta_{\rm c} = 4°$.
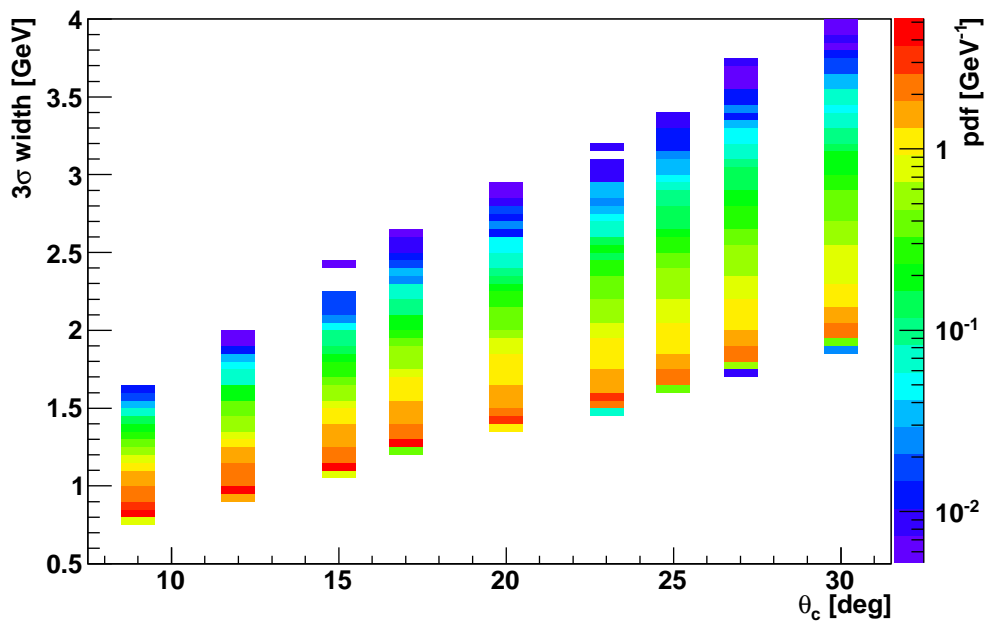

Figure 9.14: Distribution of the 3σ-interval width as a function of $\theta_{\rm c}$ at $R^{-1} = 300$ GeV with an integrated luminosity of 100 fb^{-1}.
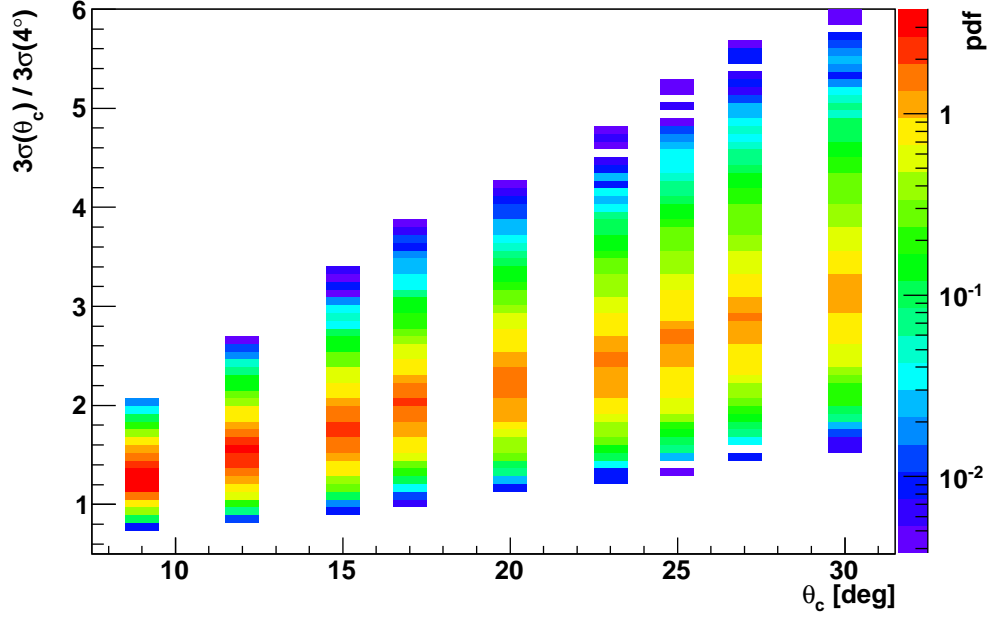
Figure 9.15: Distribution of the ratio of the 3σ-interval width at θ_c to that at $4°$ at $R^{-1} = 300$ GeV with an integrated luminosity of 100 fb^{-1}.

9.3.1 *Cross Section & Event Generation*

To produce the differential cross section binned in $(E_{\mu^\pm}, \theta_{\mu^\pm})$, we use the COMPHEP event generator to generate approximately twenty-million events for each value of R^{-1} investigated. These events are filled into a 4D histogram and normalized by the total cross section, which is also calculated with COMPHEP, yielding a 4D histogram of the differential cross section. To calculate σ_i' as needed in equation 9.15, we fit a straight line to the values σ_i of bin i in the cross section histograms for R^{-1} and at least two other compactification scales within a 10 GeV window around R^{-1}. The fit gives us both σ_i' and σ_i at R^{-1}.

To generate the binned event counts n_i of the data set D at R^{-1}, we distribute events in each bin according to Poisson statistics with the expectation value in bin i taken as $\mathscr{L}\sigma_i(R^{-1})$. We calculate α and β, store their results, generate a new data set D' and repeat.

9.3.2 *Angular Dependence of R^{-1} Measurement*

We used the procedure outlined above to generate ten-thousand data ensembles for $\mathscr{L} = 100$ fb^{-1} and calculated the symmetric 3σ-credibility interval for the measurement of the compactification scale at several representative values of R^{-1}. Figures 9.14 and 9.15 show the results of one such calculation, at $R^{-1} = 300$ GeV. The distribution of the width of the 3σ interval calculated for each iteration is shown as a function of the shielding angle θ_c in figure 9.14. The
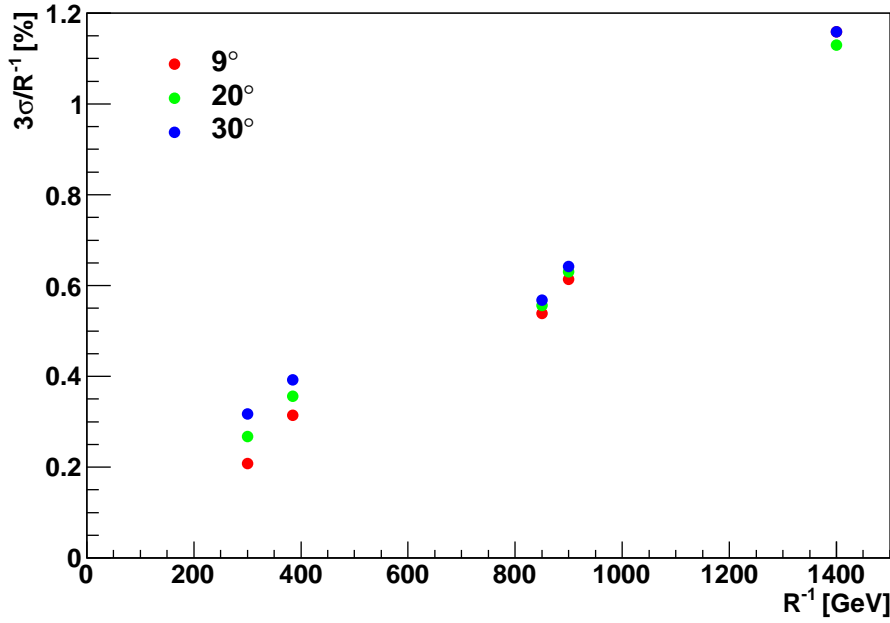
Figure 9.16: 3σ statistical precision on measuring R^{-1} with an integrated luminosity of 100 fb^{-1} at a muon collider as a function of R^{-1}, for three representative angles of detector shielding.

uncertainty on R^{-1} more than doubles as the shielding angle is increased from $9°$ to $30°$. Figure 9.15 shows the distribution of the ratio of the 3σ-credibility interval at θ_c to the interval at $4°$. This ratio is calculated for each iteration. We see that the uncertainty is 2.5 times larger at a shielding angle of $30°$ than it is at an angle of $9°$.

Figure 9.16 shows the summary of the results for values of R^{-1} of 300 GeV, 385 GeV, 850 GeV, 900 GeV, and 1400 GeV; the value shown at each (R^{-1}, θ_c) pair is the most likely interval width according to the distributions of the type shown in figure 9.14. The possible statistical unertainty on R^{-1} at a muon collider is at the percent level and lower, with the higher precisions possible for the smaller values of R^{-1}. At low compactification scales, the angle of the detector shielding can greatly affect the precision on the measurement of R^{-1}. Figure 9.17 shows the ratio of the 3σ-interval width at θ_c to that at $4°$ as a function of θ_c for the compactification scales listed above. The 3σ width widens rapidly with increase of the shielding angle at low compactification scales.

This illustrates the need to keep the shielding angle as low as possible. As discussed in chapter three, frictional cooling has the potential to produce high-luminosity muon beams with populations lower than those of other cooling schemes; this can reduce the background per bunch crossing and allow for shallower shielding angles.
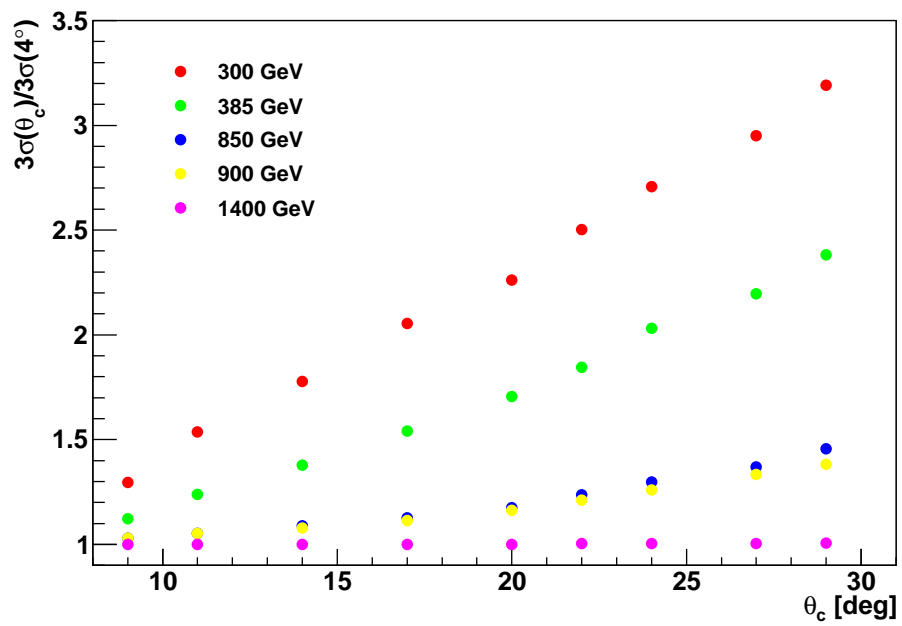
Figure 9.17: Ratio of the 3σ-interval width at θ_c to that at $4°$ as a function of θ_c for several representative values of R^{-1} with an integrated luminosity of $100\,\mathrm{fb}^{-1}$.

CHAPTER 10

Conclusion

We have presented three topics in this thesis: the impact of effective charge on frictional cooling, a scheme for beam preparation in a muon collider; the development and simulation of the Frictional Cooling Demonstration experiment at the Max Plank Institute for Physics; and the phenomenology of the universal extra dimensions model at a muon collider.

10.1 EFFECTIVE CHARGE & FRICTIONAL COOLING

Muon collider schemes employing frictional cooling are a viable option for collision of multi-TeV lepton beams. Several articles have been published with analytical and experimental results for frictional cooling of negatively charged particles (for examples see [88, 96]). Many of these articles have conjectured that the results for positively charged particles will be the same as for negatively charged particles, and schemes for the cooling of positively charged particles have been proposed (for example, the scheme presented in [97]). A key group of physics processes involved in the slowing down of positively charged particles—those inducing changes of the charge state of the particle—has been neglected in these studies. We found that accounting for these processes significantly alters the results for positively charged particles from those for negatively charged particles: The choice of cooling medium is greatly limited, such that helium gas becomes the only viable medium. The range of equilibrium energies for the cooled beam is also greatly limited, with the maximum energy possible being approximately 4 keV for a μ^+ (36 keV for a proton). And the electric field strength required to bring a beam of positively charged particles to an equilibrium energy is significantly greater than the strength required to bring a negatively charged beam to the same energy.

We developed a particle-tracking software package based on Geant4, called CoolSim, to undertake Monte-Carlo simulations of the frictional cooling of positively charged particles. The results obtained from CoolSim are in harmony with the analytical findings summarized above. CoolSim is currently capable of simulating charge exchange processes by assigning particles effective charges that approximate the rapid changes of the particles' charge states. This is a good approximation for all but the lightest densities of gas. We will continue to develop the simulation of charge exchange processes by adding to CoolSim the ability to track discrete changes of charge in very light-density media.

10.2 FCD EXPERIMENT

We have completed commissioning of the components of the FCD experiment. These include an accelerating grid that provides the electric field for frictional cooling, helium gas cell that provides the cooling medium, proton source, silicon drift detector, and detector read out system. We have developed an analysis scheme for processing the output of the detector and producing energy spectra.

We have simulated the experiment in the CoolSim software, using electric field maps calculated for the accelerating grid using a relaxation algorithm. These simulations have predicted the energy spectra of protons—transported from the source to the detector through helium gas by the electric field—for a range of strengths of the electric field and densities of the helium gas. As well, the simulations have predicted the relative rates of detection of protons for these configurations.

Energy spectra for various strengths of the electric field have been measured with the gas cell evacuated. With these spectra, we have confirmed the functioning of the proton source. Recently, spectra have been recorded for strengths of the electric field and densities of helium at which frictional cooling cannot be observed, but the effects of charge exchange can be studied. The next steps of the experiment are to analyze these new measurements and compare them to the simulations of charge exchange; and to continue the program of measurements up to higher densities of helium, where frictional cooling can be observed.

10.3 UED AT A MUON COLLIDER

Finally, we looked at the muon collider phenomenology of the universal extra dimensions model [33], which posits the existence of compact extra dimensions accessible to all standard model particles. We found that a characteristic signal of UED at a muon collider is the enhancement of the cross section for the production of soft muon pairs accompanied by large amounts of missing energy. This enhancement can be an order of magnitude or larger over a large range of compactification scales, R^{-1}. This makes discovery of UED possible for many values of R^{-1} through a measurement of this cross section.

Further developments of this analysis would extend the discussion of discoverability to larger compactification scales, where the enhancement of the cross section for soft muon pair production is small. In this range, discovery would involve comparing the dependence of the differential cross section for pair production on the energies and exit angles of the outgoing muons. We have shown this dependence in the UED model differs greatly to the dependence in the standard model. As well, supersymmetry models can be tuned to have particle mass spectra that mimic that of UED. The differentiability of SUSY and UED along the lines discussed in [36] for the proposed CLIC e^+e^- linear collider could be applied to the situation at a muon collider, with significant benefits pertaining to the finer beam energy resolution at a muon collider.

We investigated the statistical precision to which one can measure the compactification scale of a single universal extra dimension and found it to be im-

pacted by the detector shielding required at a muon collider. Such shielding will be in the form of tungsten cones radiating out from the interaction point and closing off the detection of particles exiting at small angles to the beam axis. The angle of such shielding is not yet fixed, and ranges between 9° and 30° in muon collider studies. We found that at low compactification scales, the precision possible on R^{-1} is up to approximately three times worse with 30° shielding as with 9° shielding.

The angle of such shielding depends on the amount of background radiation per bunch crossing. This in turn depends on the population of the muon bunches. We presented the frictional cooling scheme for a muon collider simulated in [55], which can deliver high beam luminosities with beam populations smaller than the schemes commonly considered in muon collider studies. This scheme would therefore reduce the backgrounds per bunch crossing, and so also the required shielding angle.

10.4 TOWARDS A MUON COLLIDER

Since the first ideas for a muon collider were published in the late 1970s, great strides have been made in overcoming the technical challenges to building one. That the muon is heavier than the electron and, unlike the proton, an elementary particle, makes a muon collider an ideal choice for a high-energy-frontier collider. New discoveries made at the LHC will further motivate the construction of a muon collider for precision measurement of the parameters of the newly discovered models and for further probing their high-energy phenomenology.

APPENDIX A

$\mu^+\mu^- \to \mu^+\mu^-\ \nu\,\bar{\nu}$

We present here the results from CompHEP for the calculation of the cross section for

$$\mu^+\mu^- \to \mu^+\mu^-\ \nu\,\bar{\nu} \tag{A.1}$$

in the SM. Since the final state is the same for all the diagrams[*], significant interference is expected between the diagrams. However, the cross sections quoted here are for the individual classes of diagrams, calculated without interferences outside of the class. The purpose of these calculations is not to determine the exact cross section, but rather to determine which diagrams will dominate in the total calculation. Chapter nine presents the total calculation, aided by the results given here.

Most of the diagrams shown in figures A.1–A.8 have charge-conjugation duals that are not shown. For these diagrams, the cross sections quoted are those of including the dual diagrams. As well, when multiple particles are written over an internal leg, the cross section includes the contributions from the individual diagrams for each possible internal particle.

All calculations are done in the Feynman gauge with the Higgs mass equal to 120 GeV/c^2. Cross sections are quoted when CompHEP was able to determine them to an uncertainty less than 1%. When the uncertainty is larger (though still below 10%) approximate cross sections or approximate upper bounds are quoted.

We present both the total cross section (σ), without cuts on the muon energies, and the soft cross section (σ_{s}), with the requirements that the individual muon energies are below 100 GeV and their total transverse energy is below 200 GeV. Notice that these are looser cuts than those used in chapter nine. When the total cross section is below 1 fb, the soft cross section is not calculated. In certain cases, CompHEP was unable to determine the total cross section to a satisfactory uncertainty, and only the soft cross section is quoted.

We divide the Feynman diagrams for tree-level muon-pair production with two neutrinos in the final state into eight topological classes. The naming scheme in the following sections is informal; FSR stands for final-state radiation, ISR for initial-state radiation.

---

[*]To be exact there are three possible final states, depending on the generation of the neutrino pair
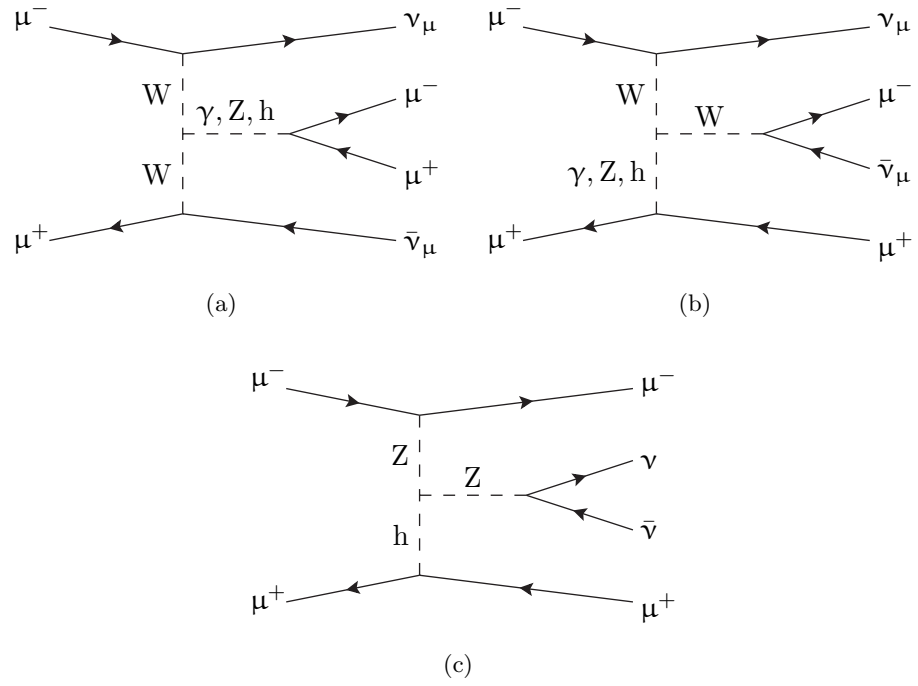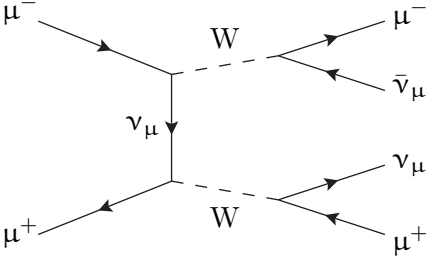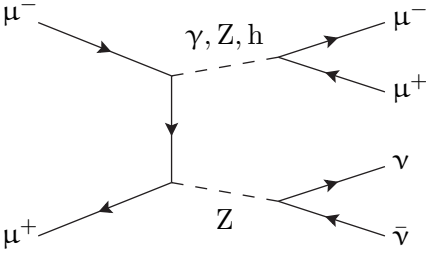
1.1 BOSON FUSION

$$\mu^- \quad\quad\quad\quad\quad\quad \nu_\mu$$

W | γ, Z, h → μ⁻, μ⁺

W

(a)

(b)

Z | h, Z

(c)

Figure A.1

Diagram	σ	σ_s
(a)	1.8 nb	2.8 pb
(b)		< fb
(c)	∼ zb	

Table A.1

1.2 *t*-CHANNEL BOSON-PAIR PRODUCTION

(a)

(b)

Figure A.2

Diagram	σ	σ_{s}
(a)	40 pb	6.6 fb
(b)	1 fb	$\sim$ ab

Table A.2
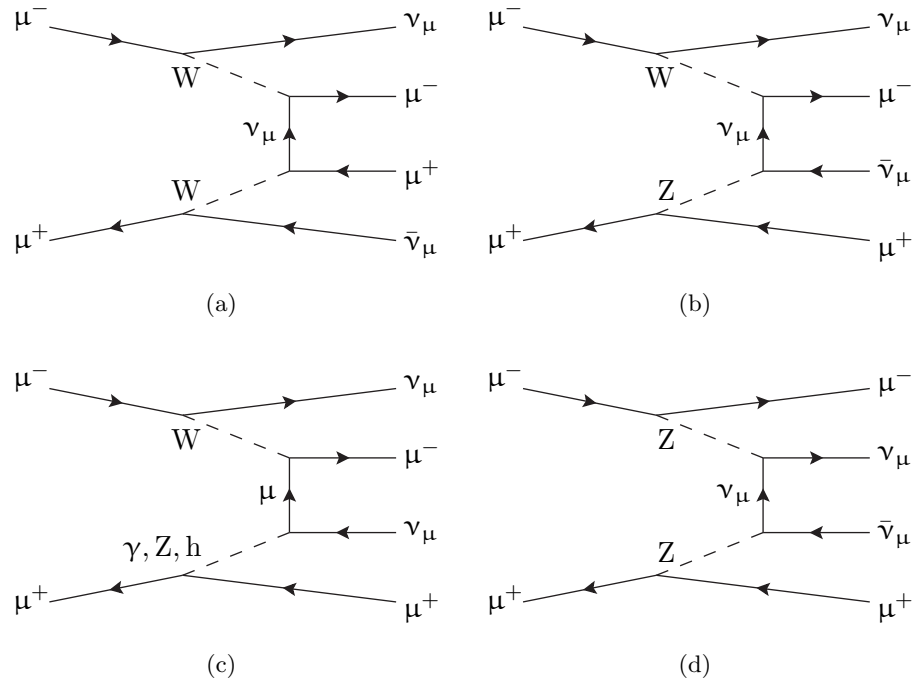
Figure A.3

Diagram	σ	σ_{s}
(a)	2 fb	0.1 fb
(b)	7 fb	$\sim$ ab
(c)		$<$ fb
(d)	0.1 fb	$\sim$ ab

Table A.3
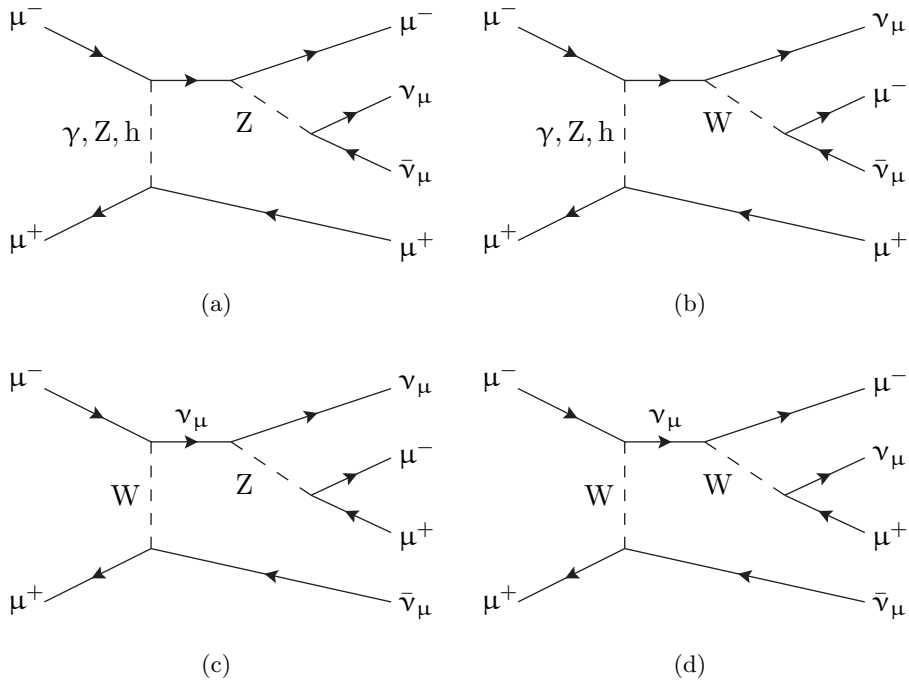
Figure A.4

Diagram	σ	σ_{s}
(a)		0.3 ab
(b)		5.9 fb
(c)	0.8 pb	8.6 fb
(d)	2 pb	$\sim$ fb

Table A.4
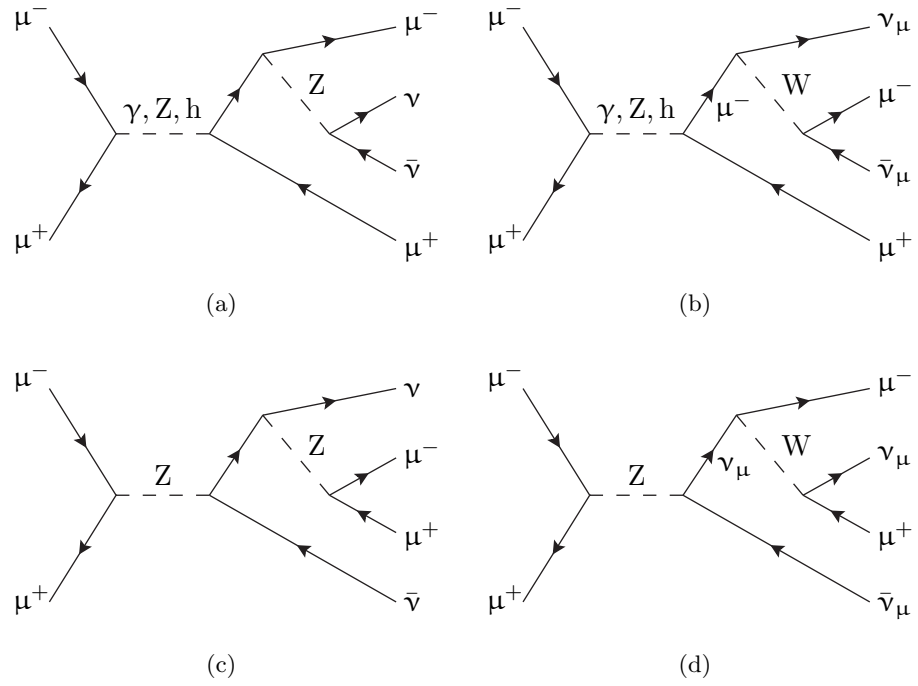
Figure A.5

Diagram	σ	σ_{s}
(a)	11 ab	
(b)	~ 0.5 fb	
(c)	15 ab	
(d)	0.2 fb	

Table A.5

(a)

(b)

(c)
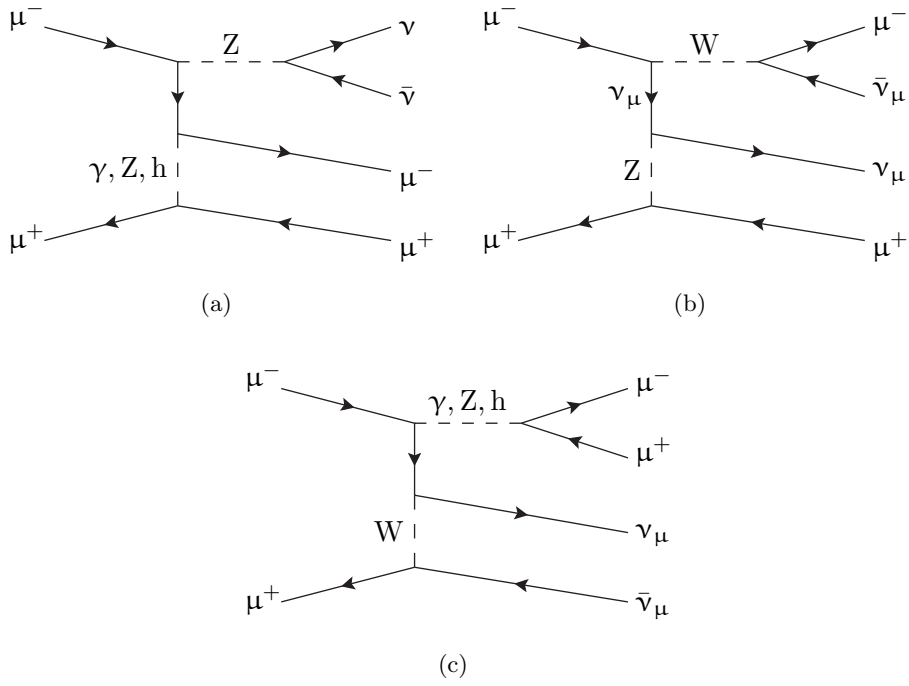
Figure A.6

Diagram	σ	σ_{s}
(a)		0.1 ab
(b)	~ 1 pb	~ 50 ab
(c)	$\sim$ nb	6 pb
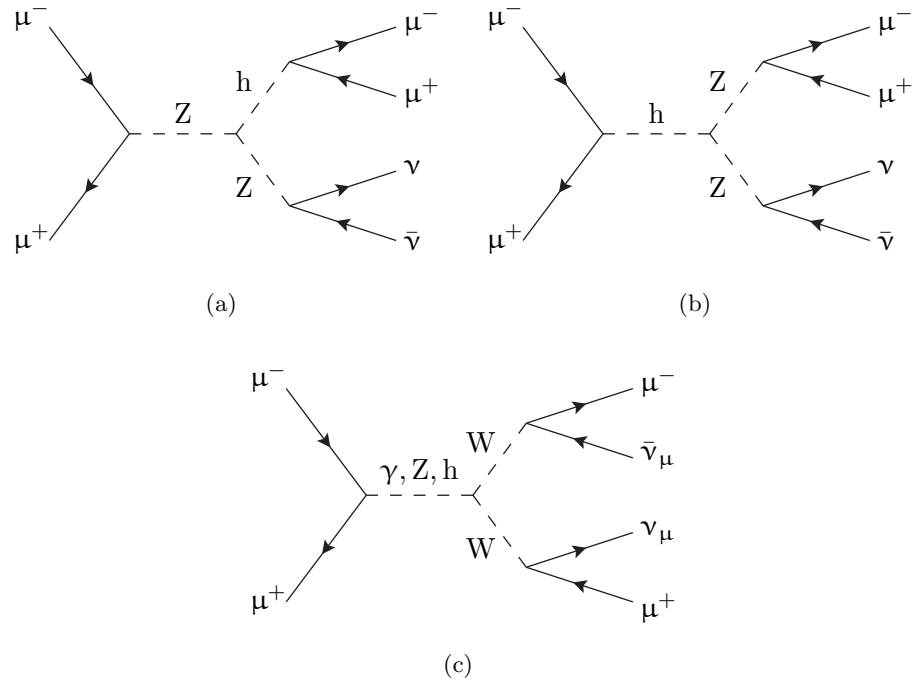
Table A.6

Figure A.7

Diagram	σ	σ_{s}
(a)	13 zb	
(b)	27 zb	
(c)	40 pb	6.6 fb

Table A.7

1.8 τ-PAIR PRODUCTION
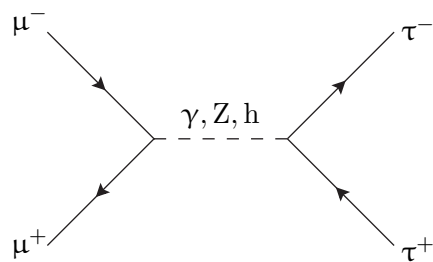
Figure A.8

σ	$\sigma \cdot \mathrm{BR}^2$
12.5 fb	0.4 fb

Table A.8

The second column in table A.8 lists the cross section for τ-pair production multiplied twice by the branching ratio for the decay $\tau \to \mu \nu_\mu \nu_\tau$, 17.36% [25].

APPENDIX B

$\mu^+\mu^- \to \mu^+\mu^-\ \nu_\mu\ \bar{\nu}_\mu\ \nu\ \bar{\nu}$

We present here the possible modifications to the dominant diagrams of appendix A to add a second neutrino pair to the final state. Most modifications are common to multiple diagrams and have a similar suppression effect on the individual diagram amplitudes. We discuss the common modifications first, presenting their approximate suppression factor, and then present modifications that are specific to a particular diagram. Six-particle (6p) final states can be challenging to calculate in CompHEP with percent-level uncertainties or lower; where noted, five-particle final states were calculated, with results modified by branching ratios.

When cross sections are quoted they are for the production of a soft muon pair (σ_s) with the requirements that the individual muon energies and their combined transverse energy are below 80 GeV.

2.1 EXTERNAL-LEG MODIFICATIONS

Figure B.1 shows the possible modifications to the incoming and outgoing external legs of the 4p diagrams. The effects of diagrams (a) and (b) were approximated by calculating the cross section for the production of an external (on-shell) Z^0 and then multiplying by the branching ratio for $Z^0 \to$ invisible, 20%. The cross sections for the 6p final states are suppressed by three orders of magnitude or greater from those for the 4p final states. Thus none of these modifications produce diagrams which contribute above the fb level to the cross section for soft muon-pair production.

2.2 INTERNAL-LEPTON MODIFICATIONS

Figure B.2 shows the possible modifications to the internal lepton legs of the 4p diagrams. Again the effects of diagrams (a) and (b) were calculated as 5p final states. Diagrams with the modifications of (a), (c), and (d) are suppressed such that none of them contribute above the fb level to soft muon-pair production. One of the dominant 4p diagrams can be modified by (b) to produce a diagram (figure B.3) with $\sigma_s = 1.5$ fb.
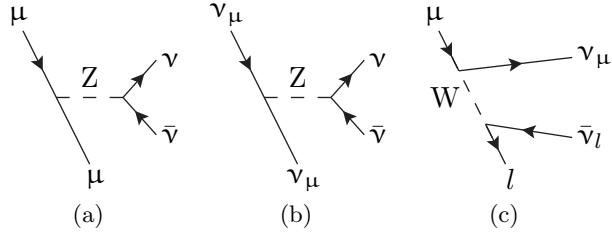
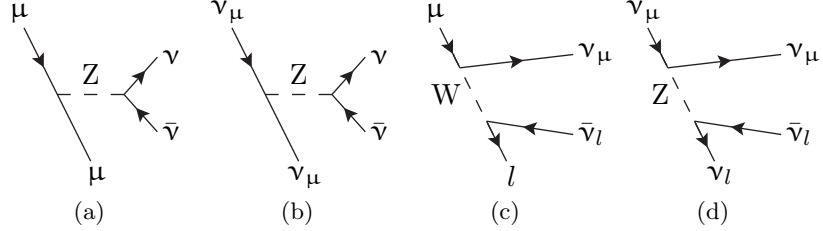Figure B.1: Modifications to external legs for the production of a neutrino pair.

Figure B.2: Modifications to the internal lepton legs for the production of a neutrino pair.
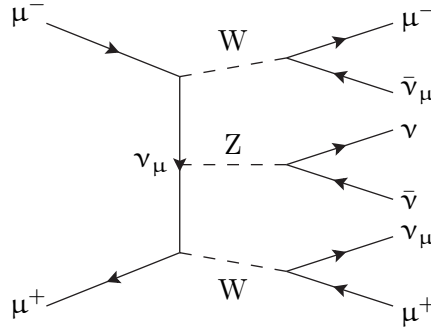

Figure B.3

2.3 INTERNAL-BOSON MODIFICATIONS

Figure B.4 shows the possible modifications to the internal vector boson legs of the 4p diagrams. All but three diagrams are suppressed when modified in this way to below the fb level. Figure B.5 shows the modifications of the three remaining diagrams; table B.1 lists their individual cross sections for soft muon-pair production.

2.4 ODDS & ENDS

Only three modifications to the 4p diagrams remain, which do not fit into one of the above three categories. Figure B.6 shows these diagrams. Needless to say, due to the abundance of added vertices, they are suppressed to well below fb.
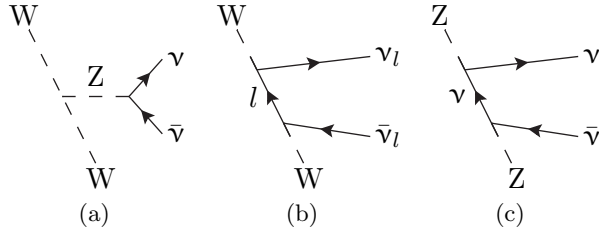
Figure B.4: Modifications to internal vector-boson legs for the production of a neutrino pair.
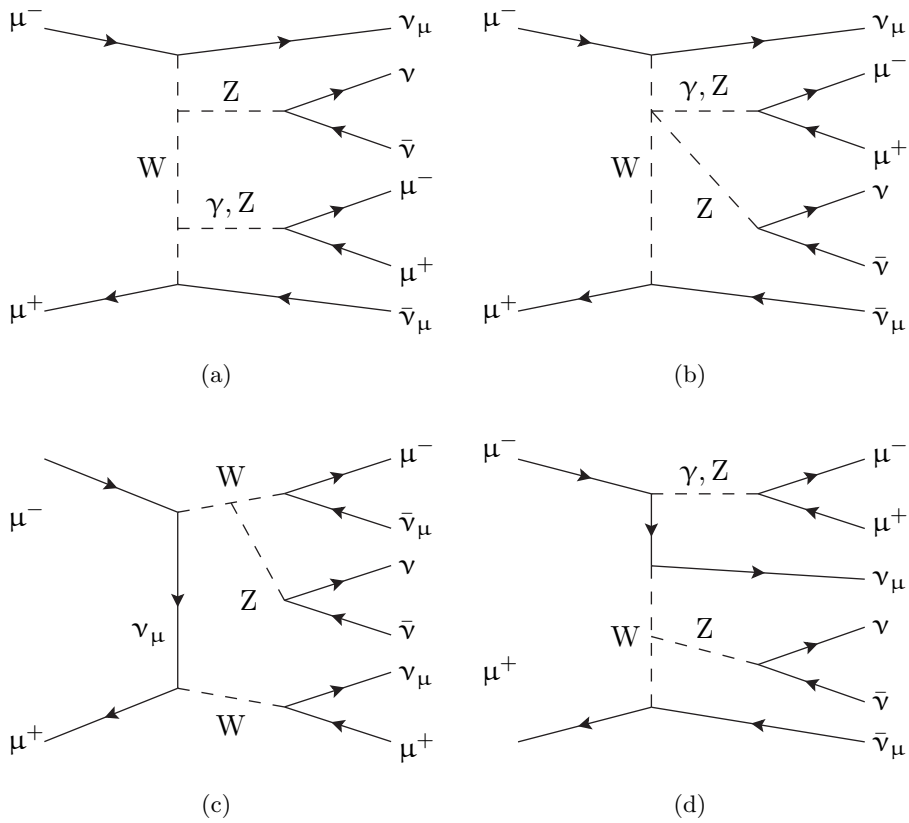

Figure B.5

Diagram	σ_s
(a) + (b)	3 fb
(c)	~ 5 fb
(d)	114 fb

Table B.1: Diagrams refer to figure B.5.
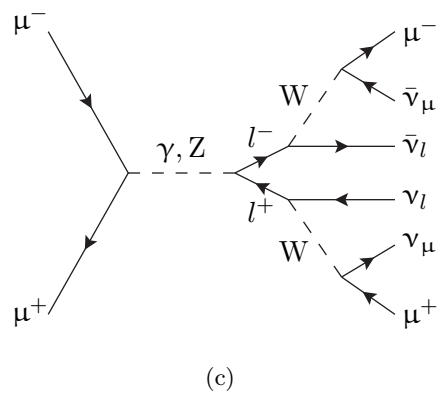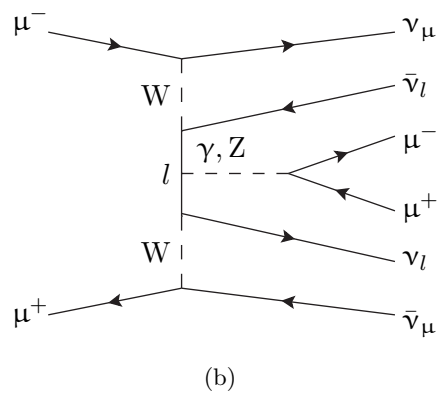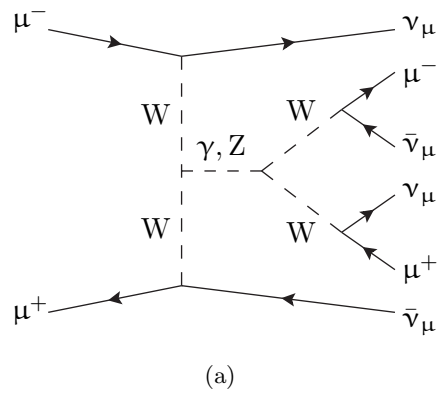
(a)

(b)

(c)

Figure B.6

126

Bibliography

[1]   S. L. Glashow, Nucl. Phys. **22**, 579 (1961).

[2]   S. Weinberg, Phys. Rev. Lett. **19**, 1264 (1967).

[3]   A. Salam, Nobel Symp. 8 , 367 (1968).

[4]   D. Neuffer, Fermilab Report No. FN-0319, 1979.

[5]   M. Sands, SLAC Report No. 0121, 1970.

[6]   ILC Report No. 2007-001, 2007.

[7]   R. W. Assmann *et al.*, CERN Report No. 2000-008, 2000.

[8]   A. D. Martin, W. J. Stirling, R. S. Thorne, and G. Watt, Eur. Phys. J. **C63**, 189 (2009).

[9]   LHC/ILC Study Group, G. Weiglein *et al.*, Phys. Rept. **426**, 47 (2006).

[10]   V. Shiltsev, Mod. Phys. Lett. **A25**, 567 (2010), 1003.3051.

[11]   V. D. Barger, AIP Conf. Proc. **441**, 3 (1998).

[12]   J. Gunion, AIP Conf. Proc. **435**, 37 (1998).

[13]   R. N. Mohapatra, AIP Conf. Proc. **435**, 358 (1998).

[14]   M. M. Alsharo *et al.*, Phys. Rev. ST Accel. Beams **6**, 081001 (2003).

[15]   C. M. Ankenbrandt *et al.*, Phys. Rev. ST Accel. Beams **2**, 081001 (1999).

[16]   C. Blöchinger *et al.*, (2002), hep-ph/0202199v1.

[17]   V. Barger, M. Berger, J. Gunion, and T. Han, Snowmass Proc. (2001).

[18]   S. Y. Choi, J. Kalinowski, Y. Liao, and P. M. Zerwas, Eur. Phys. J. C. **40**, 555 (2005).

[19]   B. Grzadkowski, J. F. Gunion, and J. Pliszka, Nucl. Phys. B **583**, 49 (2000).

[20]   D. Atwood and A. Soni, Phys. Rev. D **52**, 6271 (1995).

[21]   V. Barger, M. S. Berger, and T. Han, Phys. Rev. D. **59**, 071701 (1998).

[22] F. E. Paige, AIP Conf. Proc. **435**, 537 (1998), hep-ph/9801396v1.

[23] J. D. Lykken, (1998), hep-ph/9803427v1.

[24] M. S. Berger, AIP Conf. Proc. **441**, 79 (1998), hep-ph/9802213v1.

[25] Particle Data Group, K. Nakamura *et al.*, J. Phys. G **G37**, 075021 (2010).

[26] V. Barger, M. Berger, J. Gunion, and T. Han, Nucl. Phys. B-Proc Sup **51**, 13 (1996).

[27] D. Choudhury and S. Raychaudhuri, (1998), hep-ph/9807373v1.

[28] V. Barger, M. S. Berger, J. F. Gunion, and T. Han, Phys. Rev. D **55**, 142 (1997).

[29] S. Godfrey, J. L. Hewett, and L. E. Price, (1996), hep-ph/9704291v1.

[30] S. Godfrey, (1997), hep-ph/9802212v1.

[31] N. Arkani-Hamed, S. Dimopoulos, and G. Dvali, Phys. Lett. B **429**, 263 (1998).

[32] L. Randall and R. Sundrum, Phys. Rev. Lett. **83**, 3370 (1999).

[33] T. Appelquist, H.-C. Cheng, and B. A. Dobrescu, Phys. Rev. D **64**, 035002 (2001).

[34] J. D. Lykken, (1996), hep-th/9612114.

[35] M. Battaglia, A. K. Datta, A. D. Roeck, K. Kong, and K. T. Matchev, (2005), hep-ph/0507284v1.

[36] M. Battaglia, A. K. Datta, A. D. Roeck, K. Kong, and K. T. Matchev, JHEP **7**, 33 (2005).

[37] Nova Collaboration, D. Ayres *et al.*, (2002), hep-ex/0210005.

[38] K2K Collaboration, Y. Oyama, (1998), hep-ex/9803014.

[39] K. Hagiwara, N. Okamura, and K. Senda, Phys. Rev. D. **76**, 093002 (2007).

[40] ISS Physics Working Group, A. Bandyopadhyay *et al.*, Rep. Prog. Phys. **72**, 106201 (2009).

[41] A. Donini, D. Meloni, and P. Migliozzi, Nucl. Phys. B **646**, 321 (2002).

[42] S. Geer, Phys. Rev. D **57**, 6989 (1998).

[43] B. J. King, AIP Conf. Proc. **435**, 334 (1998).

[44] D. A. Harris and K. S. McFarland, AIP Conf. Proc. **435**, 505 (1998).

128

[45] H. Schellman, AIP Conf. Proc. **435**, 166 (1998).

[46] K. Cheung, AIP Conf. Proc. **441**, 338 (1998).

[47] T. Kinoshita and W. J. Marciano, Theory of the muon anomalous magnetic moment, in *Quantum Electrodynamics*, edited by T. Kinoshita, , Adv. Ser. Direct. High Energy Phys. Vol. 7, chap. 10, pp. 419–478, World Scientific, 1990.

[48] A. Czarnecki and W. J. Marciano, Electromagnetic dipole moments and new physics, in *Lepton Dipole Moments*, edited by B. L. Roberts and W. J. Marciano, , Adv. Ser. Direct. High Energy Phys. Vol. 20, chap. 2, pp. 11–67, World Scientific, 2010.

[49] J. Aysto *et al.*, (2001), hep-ph/0109217.

[50] E. De Rafael, Nucl. Phys. B-Proc. Sup. **186**, 211 (2009).

[51] Y. Kuno, Search for the charged lepton-flavor-violating transition moments $l \to l'$, in *Lepton Dipole Moments*, edited by B. L. Roberts and W. J. Marciano, , Adv. Ser. Direct. High Energy Phys. Vol. 20, chap. 19, pp. 701–745, World Scientific, 2010.

[52] W. J. Marciano, AIP Conf. Proc. **435**, 58 (1998).

[53] W. Molzon, AIP Conf. Proc. **435**, 152 (1998).

[54] C. Ankenbrandt *et al.*, Fermilab Report No. TM-2399-APC, 2009.

[55] H. Abramowicz, A. Caldwell, R. Galea, and S. Schlenstedt, Nucl. Instr. and Meth. A **546**, 356 (2005).

[56] O. E. Krivosheev and N. V. Mokhov, Fermilab Report No. CONF-00-186, 2000.

[57] N. V. Mokhov, K. K. Guidman, J. B. Strait, and S. I. Striganov, Fermilab Report No. CONF-09-646, 2009.

[58] J. S. Berg, AIP Conf. Proc. **1222**, 358 (2010).

[59] J. Wei, S.-N. Fu, and S.-X. Fang, High-power accelerators in China: Status and outlook, in *Proceedings of HB2006*, 2006.

[60] P. Piwnicki ed., PSI Paul Scherrer Institute, Villigen. Scientific report 2009.

[61] Y. Yamazaki ed. *et al.*, KEK Report No. 2002-13, 2003.

[62] Y. Miyake *et al.*, Nucl. Instr. and Meth. A **600**, 22 (2009).

[63] Y. Miyake *et al.*, Strongest pulsed muon source at J-PARC MUSE, in *NuFact 2010*, 2011.

[64] S. D. Holmes, Project X: A Multi-MW Proton Source at Fermilab, in *IPAC10*, 2010.

[65] G. Flanagan *et al.*, Using Project X as a Proton Driver for Muon Colliders and Neutrino Factories, in *IPAC10*, 2010.

[66] S. D. Holmes ed., Project X Initial Configuration Document, 2009.

[67] S. D. Holmes ed., Project X Initial Configuration Document - 2, 2010.

[68] K. T. McDonald *et al.*, The MERIT High-Power Target Experiment at the CERN PS, in *IPAC10*, 2010.

[69] D. Neuffer, Part. Accel. **14**, 75 (1983).

[70] V. V. Parkhomchuk and A. N. Skrinsky, AIP Conf. Proc. **352**, 7 (1996).

[71] A. Kolomenskii, Atomic Energy **19**, 1511 (1965).

[72] Y. M. Ado and V. I. Balbekov, Atomic Energy **31**, 731 (1971).

[73] G. I. Budker, Atomic Energy **22**, 438 (1967).

[74] A. N. Skrinsky and V. V. Parkhomchuk, Sov. J. Part. Nucl. **12**, 223 (1981).

[75] R. Palmer *et al.*, Phys. Rev. ST Accel. Beams **8**, 061003 (2005).

[76] J. Monroe *et al.*, Phys. Rev. Special Topics – Accel. and Beams **4**, 041301 (2001).

[77] A. Blondel *et al.*, Letter of Intent: An International Muon Ionization Cooling Experiment (MICE).

[78] R. Edgecock, J. Phys. **G29**, 1601 (2003).

[79] S. Ozaki *et al.*, BNL Report No. 52623, 2001.

[80] MICE Collaboration, F. J. P. Soler, AIP Conf. Proc. **1222**, 288 (2010).

[81] L. Coney, Status of the MICE Muon Ionization Cooling Experiment, in *PAC09*, 2009.

[82] O. Benary, S. Kahn, and I. Stumer, AIP Conf. Proc. **530**, 1 (2000).

[83] I. Stumer *et al.*, Study of detector backgrounds in a mu+ mu- collider, in *Snowmass*, 1996.

[84] I. F. Ginzburg, Nucl. Phys. B-Proc Sup **51A**, 186 (1996).

[85] Stopping powers and ranges for protons and alpha particles, 1993, Bethesda, USA: ICRU (1993) 286 p. (ICRU report: 49).

[86] M. Agnello *et al.*, Phys. Rev. Lett. **74**, 371 (1995).

[87] P. Sigmund and A. Schinner, Eur. Phys. J. C. **15**, 165 (2001).

[88] M. Mühlbauer, H. Daniel, and F. J. Hartmann, Hyperfine Interact. **82**, 459 (1993).

[89] U. Fano, Ann. Rev. Nucl. Part. Sci. **13**, 1 (1963).

[90] J. F. Ziegler, J. P. Biersack, and M. D. Ziegler, *The Stopping and Range of Ions in Matter* (SRIM Co., 2008).

[91] B. H. Bransden and C. Forster, J. Phys. B-At. Mol. Opt. **23**, 115 (1990).

[92] P. Sigmund, *Stopping of Heavy Ions: A Theoretical Approach* (Springer-Verlag, 2004).

[93] S. K. Allison, Rev. Mod. Phys. **30**, 1137 (1958).

[94] Y. Nakai, T. Shirai, T. Tabata, and R. Ito, Atom. Data Nucl. Data **37**, 69 (1987).

[95] A. E. S. Green and R. J. McNeal, J. Geophys. Res. **76**, 133 (1971).

[96] M. Mühlbauer *et al.*, Nucl. Phys. B **51A**, 135 (1996).

[97] T. J. Roberts and D. M. Kaplan, Particle Refrigerator, in *PAC09*, 2009.

[98] D. M. Kaplan, Muon Cooling and Future Muon Facilities: The Coming Decade, in *DPF09*, 2009.

[99] J. S. Cohen, Phys. Rev. A **65** (2002).

[100] J. S. Cohen, J. Phys. B-At. Mol. Opt. **31**, L833 (1998).

[101] J. Sommerville, Proc. Phys. Soc. B **65**, 620 (1952).

[102] W. Blum and L. Rolandi, *Particle Detection with Drift Detectors* (Springer-Verlag, 1994).

[103] Y. Bao, A. Caldwell, D. Greenwald, and G. Xia, Nucl. Instr. and Meth. A **622**, 28 (2010).

[104] GEANT4 Collaboration, S. Agostinelli *et al.*, Nucl. Instrum. Meth. A **506**, 250 (2003).

[105] L. Urbán, CERN Report No. OPEN-2006-077, 2006.

[106] V. N. Ivanchenko, O. Kadri, M. Maire, and L. Urban, J. Phys. Conf. Ser. **219**, 032045 (2010).

[107] R. Brun and F. Rademakers, Nucl. Instrum. Meth. A **389**, 81 (1997).

[108] H. Tawara, T. Kato, and Y. Nakai, Atom. Data Nucl. Data **32**, 235 (1985).

[109] M. Simson *et al.*, Detection of low-energy protons using a silicon drift detector, TU Munich, 2007.

[110] PNSensor, http://www.pnsensor.de.

[111] National Instruments, http://www.ni.com.

[112] LabView, http://www.ni.com/labview.

[113] M. M. Pejovic, G. S. Ristic, and J. P. Karamarkovic, J. Phys. D **35**, R91 (2002).

[114] S. N. Sen and A. K. Ghosh, Proceedings of the Physical Society **79**, 180 (1962).

[115] M. W. F. Popp, *Untersuchung und analytische modellierung der systemantwort von pn-CCD detektoren*, PhD thesis, Ludwig-Maximilians-Universität München, 2000.

[116] M. Popp *et al.*, Nucl. Instr. and Meth. A **439**, 567 (2000).

[117] G. Nördstrum, Phys. Zeit. **XV**, 504 (1914).

[118] T. Kaluza, Sitzungsber. Preuss. Akad. Wiss. Berlin **1921**, 966 (1921).

[119] O. Klein, Z. Phys. **37**, 895 (1926).

[120] J. van Dongen, Stud. Hist. Philos. M. P. **33**, 185 (2002).

[121] P. Halpern, Phys. Persp. **9**, 390 (2007).

[122] K. R. Dienes, E. Dudas, and T. Gherghetta, Nucl. Phys. B **537**, 47 (1999).

[123] T. Appelquist, B. A. Dobrescu, E. Pontón, and H.-U. Yee, Phys. Rev. Lett. **87**, 181802 (2001).

[124] N. Arkani-Hamed and M. Schmaltz, Phys. Rev. D **61**, 033005 (2000).

[125] B. A. Dobrescu and E. Poppitz, Phys. Rev. Lett. **87**, 031801 (2001).

[126] N. Arkani-Hamed, H.-C. Cheng, B. A. Dobrescu, and L. J. Hall, Phys. Rev. D **62**, 096006 (2000).

[127] G. D. Kribs, TASI Lectures on Phenomenology of extra dimensions, 2006.

[128] H.-C. Cheng, TASI Lectures Introduction to Extra Dimensions, 2010.

[129] J. Papavassiliou and A. Santamaria, Phys. Rev. D **63**, 125014 (2001).

[130] H. Georgi, A. K. Grant, and G. Hailu, Phys. Rev. D **63**, 064027 (2001).

[131] H. Georgi, A. K. Grant, and G. Hailu, Phys. Lett. B **506**, 207 (2001).

[132] H.-C. Cheng, K. T. Matchev, and M. Schmaltz, Phys. Rev. D **66**, 036005 (2002).

[133] C. Macesanu, C. D. McMullen, and S. Nandi, Phys. Rev. D **66**, 015009 (2002).

[134] J. A. R. Cembranos, J. L. Feng, and L. E. Strigari, Phys. Rev. D **75**, 036004 (2007).

[135] H.-C. Cheng, K. T. Matchev, and M. Schmaltz, Phys. Rev. D **66**, 056006 (2002).

[136] T. Appelquist and B. A. Dobrescu, Phys. Lett. B **516**, 85 (2001).

[137] T. G. Rizzo, Phys. Rev. D **64**, 095010 (2001).

[138] M. E. Peskin and T. Takeuchi, Phys. Rev. Lett. **65**, 964 (1990).

[139] G. Altarelli and R. Barbieri, Phys. Lett. B **253**, 161 (1991).

[140] T. Appelquist and H.-U. Yee, Phys. Rev. D **67**, 055002 (2003).

[141] T. Flacke, D. Hooper, and J. March-Russell, Phys. Rev. D **73**, 095002 (2006).

[142] I. Gogoladze and C. Macesanu, Phys. Rev. D **74**, 093012 (2006).

[143] K. Agashe, N. G. Deshpande, and G. H. Wu, Phys. Lett. B **514**, 309 (2001).

[144] A. J. Buras, M. Spranger, and A. Weiler, Nucl. Phys. B **660**, 225 (2003).

[145] A. J. Buras, A. Poschenrieder, M. Spranger, and A. Weiler, Nucl. Phys. B **678**, 455 (2004).

[146] J. F. Oliver, J. Papavassiliou, and A. Santamaria, Phys. Rev. D **67**, 056002 (2003).

[147] G. Servant and T. M. P. Tait, Nucl. Phys. B **650**, 391 (2003).

[148] M. Kakizaki, S. Matsumoto, and M. Senami, Phys. Rev. D **74**, 023504 (2006).

[149] F. Burnell and G. D. Kribs, Phys. Rev. D **73**, 015001 (2006).

[150] S. Matsumoto, J. Sato, M. Senami, and M. Yamanaka, Phys. Rev. D **80**, 056006 (2009).

[151] A. Datta, K. Kong, and K. T. Matchev, Phys. Rev. D **72**, 096006 (2005).

[152] G. Bhattacharyya, A. Datta, S. K. Majee, and A. Raychaudhuri, Nucl. Phys. B **821**, 48 (2009).

[153] B. Bhattacherjee and K. Ghosh, Phys. Rev. D **83**, 034003 (2011).

[154] J. M. Smillie and B. R. Webber, JHEP **10**, 069 (2005).

[155] A. Barr, Phys. Lett. B **596**, 205 (2004).

[156] G. Corcella *et al.*, JHEP **01**, 010 (2001).

[157] CompHEP Collaboration, E. Boos *et al.*, Nucl. Instrum. Meth. A **534**, 250 (2004).

[158] A. Datta, K. Kong, and K. T. Matchev, New J. Phys. **12**, 075017 (2010).

Acknowledgements

Many people have made my time at the institute and in Munich a very great one, I would like to thank

—o Prof. Allen Caldwell for hiring me as a summer student over a decade ago, inviting me into the group in Munich, helping me to further my education, and providing invaluable guidance all along the way.

—o Daniel Kollár, for teaching me how to write a scientific paper, and the value of labeled axes even on practice plots.

—o My fellow Muon Collider groupmates, Bao Yu, Christian Blume, Brodie MacKenzie, and Andrada Ianus for all the help in the lab and contributions to the experiment.

—o Si Tran, for fixing the endless series of broken electronics and giving me his pho recipe. Karlheinz Ackermann and Alexander Wimmer for constructing all the intricate pieces of the FCD experiment.

—o My officemates, Annika and Sabine for putting up with the snowdrifts of papers around the office and the music I inflicted upon them. And the other members of the Gerda group, Hossein, Sabine, Fabiana, Chris, Jing, and Daniel for providing a fun office environment. Especially Kevin Kröninger and Xiang Liu for helping to welcome me into the institute so many years ago.

—o The head-in-the-clouds theorists at the institute, for enlightening discussions, ethnic cuisines, and physics questions answered, in particular Javier Redondo, Lorenzo Calibbi, and of course Clemens Kießig, thank you so much for helping with German translations and field theory questions.

—o Julia Grebeniouk for ROOT commiseration. And Fred Beaujean for answering all my pestering statistics questions.

—o My Parents, Rachel and Ken, who even four years after I've attended any classes still ask me "How's school going? How're classes?"

—o Elisabeth Veh, Fiona Brutscher, and Arek Odoj for helping to naturalize me as Bavarian.

—o Franziska Schwarz, who hasn't seen much of me in three months, but kindly left food out for me many nights, and woke me up each morning and sent me on my way to finishing this thesis. Thank you.